Magnetic fields in giant planet formation and protoplanetary discs

Sarah Louise Keith

MACQUARIE University
SYDNEY · AUSTRALIA

Department of Physics and Astronomy

Faculty of Science and Engineering

A thesis submitted to Macquarie University
for the degree of Doctor of Philosophy
December 2015

Typeset in $\LaTeX\,2_\varepsilon$.

Contents

Abstract

Protoplanetary discs channel accretion onto their host star. How this is achieved is critical to the growth of giant planets which capture their massive gaseous atmosphere from the surrounding flow. Theoretical studies find that an embedded magnetic field could power accretion by hydromagnetic turbulence or torques from a large-scale field. This thesis presents a study of the influence of magnetic fields in three key aspects of this process: circumplanetary disc accretion, gas flow across gaps in protoplanetary discs, and magnetic-braking in accretion discs.

The first study examines the conditions needed for self-consistent accretion driven by magnetic fields or gravitational instability. Models of these discs typically rely on hydromagnetic turbulence as the source of effective viscosity. However, magnetically-coupled, accreting regions may be so limited that the disc may not support sufficient inflow. An improved Shakura-Sunyaev α disc is used to calculate the ionisation fraction and strength of non-ideal effects. Steady magnetically-driven accretion is limited to the thermally ionised, inner disc so that accretion in the remainder of the disc is time-dependent.

The second study addresses magnetic flux transport in an accretion gap evacuated by a giant planet. Assuming the field is passively drawn along with the gas, the hydrodynamical simulation of Tanigawa, Ohtsuki & Machida (2012) is used for an a posteriori analysis of the gap field structure. This is used to post-calculate magnetohydrodynamical quantities. This assumption is self-consistent as magnetic forces are found to be weak, and good magnetic coupling ensures the field is frozen into the gas. Hall drift dominates across much of the gap, with the potential to facilitate turbulence and modify the toroidal field according to the global field orientation.

The third study considers the structure and stability of magnetically-braked accretion discs. Strong evidence for MRI dead-zones has renewed interest in accretion powered by large-scale fields. An equilibrium model is presented for the radial structure of an axisymmetric, magnetically-braked accretion disc connected to a force-free external field. The accretion rate is multivalued at protoplanetary disc column densities, featuring an 'S-curve' associated with models of accretion outbursting. A local, linear analysis of the stability of radial modes finds that the rapidly accreting, middle and upper solution branches are unstable, further highlighting the potential for eruptive accretion events.

Statement of Candidate

I certify that the work in this thesis has not been submitted for award of any other degree or diploma at any university or equivalent institution. This dissertation is the result of my own work and includes nothing which is the outcome of work done in collaboration except where specifically indicated in the text. Those parts of this thesis which have been published are as follows:

- Chapter 2 is based very closely on the following journal paper. I derived the equation set, carried out the calculations, and wrote the paper.

  'Accretion in giant planet circumplanetary discs', by Sarah L. Keith & Mark Wardle, appearing in the Monthly Notices of the Royal Astronomical Society, **440**, p. 89-105, 2014.

- Chapter 3 is based very closely on the following journal paper. In this chapter, I used a snapshot from the Tanigawa, Ohtsuki & Machida (2012) simulation as the underlying disc model for this calculation. The data was used with permission from Takayuki Tanigawa. I performed the subsequent MHD calculations, analysed the findings and wrote the paper.

  'Magnetic fields in gaps surrounding giant protoplanets', by Sarah L. Keith & Mark Wardle, appearing in the Monthly Notices of the Royal Astronomical Society, **451**, p. 5623–5635, 2015.

Sarah Keith
December 2015

Acknowledgements

First and foremost, I would like to thank my supervisor, Mark Wardle, for his guidance, encouragement, and scientific insight in what has been a very enjoyable project. I am indebted to him for the support he gave me in my move to England, for teaching me to strive toward physical insight, and for his friendship.

I would like to thank the Department of Physics and Astronomy at Macquarie University for their assurance of support following my move to England, and the Jodrell Bank Centre for Astrophysics and the University of Manchester for giving me a visiting position for two years. Thank you to Carol McNaught, Lisa Chanell, David Spence, Jane Yang and others at Macquarie University who had to deal with my crazy requests and paperwork.

Thank you to Pandey, Yurii Fujii, Takayuki Tanigawa, Raquel Salmeron, Matthew Bate, Oliver Gressel, Donna Rogers-Lee and Turlough Downes for helpful conversations, practical assistance with the project, and in some cases, hospitality. I am especially grateful to Philippa Browning for making time for me, and for helpful discussions and comments on my articles.

Thank you also to Tui Britton, Leonie Wainwright, Jess Traynor, Mark and Alex Glew, Alan Chettle, office mates at Macquarie and Manchester, and friends at Holy Trinity Platt for cups of tea and encouragement over the course of the project.

Finally, I would like to express my gratitude to my family. In particular, to my parents and grandparents for their continual love and enthusiasm, and for the million ways they made this PhD possible; to my husband, Michael for his unwavering love and companionship in all the crazy things we did this last four years - looking forward to being Doctor and Doctor Keith; to my Heavenly Father, for everything He has done for me, and in me over this PhD.

1
Introduction

Until the late 20th century, the Solar system was our only laboratory for the study of planet formation. From this single example, it was deduced that the planets grow from a circumstellar disc left over from the formation of the central star. Rocky planets form through the hierarchical growth of solid bodies from the dust in the disc. Further from the star ices bulk up planetary cores sufficiently to gravitationally capture the massive, gaseous atmosphere, characteristic of giant planets (Safronov, 1967, 1969).

The discovery of the first extra-solar planets in the 1990's (Wolszczan & Frail, 1992; Mayor & Queloz, 1995), and of the diversity of exoplanetary systems (Borucki et al., 2010), has revolutionised the field. Over 1500 planets have now been discovered orbiting stars other than our Sun. Giant planets are relatively common, with surveys indicating that they are present in approximately one in five planetary systems around Solar-type stars (Winn & Fabrycky, 2015). Fig. 1.1 shows the distribution of exoplanet and Solar system planet mass with orbital radius (cataloged in the `www.exoplanet.eu` exoplanet database; Schneider et al., 2011). Unlike our Solar system, giant exoplanets are found a wide range of orbits (orbital distances $d \approx 0.01$–$100\,\mathrm{au}$), and in a variety of extreme exoplanetary system configurations.

This has highlighted the important role of gas giants in shaping planetary systems. The notion that giant planets are confined to the cold, outer regions of a planetary system was dismantled by the discovery of a significant population of Jovian-mass planets in tight orbits around their host star (orbital distance $d < 0.1\,\mathrm{au}$;

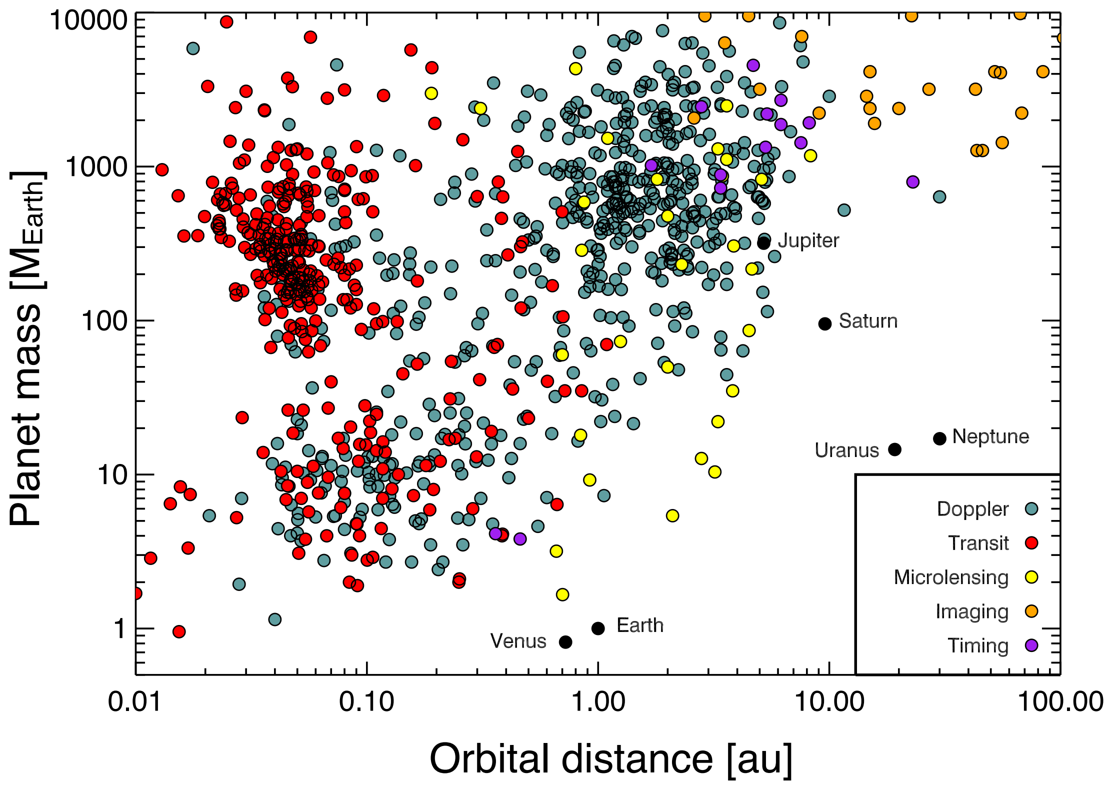

Figure 1.1: Approximate masses and orbital distances of known Solar system planets (black) and exoplanets. Exoplanet data points are colour-coded according to detection method: radial velocity (green), transit (red), microlensing (yellow), direct imaging (orange), and timing (purple). This figure appears in Winn & Fabrycky (2015) and uses data from the `www.exoplanet.eu` database (Schneider et al., 2011), accessed in October 2014 .

Wolszczan & Frail, 1992). These so-called 'hot Jupiters' challenged theories which assumed that planets formed at their present-day orbit. So close to the star, the disc is too hot for ice grains, which are necessary to sufficiently bulk up a giant planet core to capture a massive atmosphere. Furthermore, giant planets are disruptive members of their planetary system. Giant planets are less likely to be in a multiple-planet system, and have a broader eccentricity distribution, than their smaller counterparts (Latham et al., 2011; Dawson & Murray-Clay, 2013).

Instead, theoretical models of planet formation demonstrate that planetary orbits are not static and can evolve significantly prior to the establishment of the final system architecture (Lin & Papaloizou, 1986). Giant planets migrating through a system disrupt the orbits of nearby objects, ejecting some from the system, and clearing the feeding zone of others (Gomes et al., 2005; Tsiganis et al., 2005; Walsh et al., 2011). Naturally, models accounting for the formation of diverse planetary systems are complex and multi-faceted, and observations of planet formation in action are needed to confirm or redirect theory.

Crucially, high sensitivity, high resolution submillimeter observations with the Atacama Large Millimeter/submillimeter Array (ALMA) are opening planet formation to observational scrutiny. Forming planets are obscured by dust and gas, yet they create observable, large-scale structures in the disc. Giant planets carve out annular gaps in the gas around their orbit (Lin & Papaloizou, 1986), and dust cavities could also result from grain growth or the incorporation of dust into a planet core (Zhang, Blake & Bergin, 2015). Spiral arms and gas streams bridging disc gaps are signatures of by an unseen protoplanet (Casassus et al., 2013; Dong et al., 2015; Ober et al., 2015; Zhu et al., 2015). An accreting giant planet and circumplanetary disc may be hot enough to detect through a mid-infrared excess or submillimeter molecular emission (Cleeves, Bergin & Harries, 2015; Zhu, 2015), and CO line emission offers the potential to trace the kinematics in the circumplanetary region (Perez et al., 2015).

1.1 Giant planet formation

Most giant planets are thought to form according to the core accretion model (Safronov, 1969; Mizuno, 1980). This process involves the production of a planetary core out of rock and ice present in the nebula, in much the same fashion as rocky planet growth. These cores grow increasingly rapidly, and capture a substantial atmosphere (Bodenheimer & Pollack, 1986; Pollack et al., 1996).

The first stage of giant planet core assembly involves collisional growth of dust and ice grains within a protoplanetary disc. Gravitational settling concentrates the grains at the midplane, increasing the collision rate. Low impact collisions (i.e., those with velocities $\lesssim 1\,\mathrm{m\,s^{-1}}$) of μm-sized grains result in net particle growth via sticking through intermolecular, van der Waals forces (Blum & Wurm, 2008).

Planetesimal growth is not so easily accounted for. Firstly, collisions between cm-sized particles typically result in the objects bouncing off one another, rather than growth (Zsom et al., 2010). Growth of metre-sized planetesimals is hampered by low binding energies and high relative collision velocities (Youdin, 2010). The second challenge is the inward-spiraling and eventual accretion of centimetre to metre sized objects by the protostar (Whipple, 1972; Weidenschilling, 1977). Gas and entrained small grains experience radial support against the gravitational force from an outward pressure gradient. This reduces their effective potential and consequently their orbital speed. Larger grains, on the other hand, do not feel the pressure gradient and so they orbit at the slightly faster Keplerian speed. Therefore, large grains experience a gas headwind. While this provides an opportunity for larger grains to grow by sweeping up smaller particles (Weidenschilling & Cuzzi, 1993), energy loss associated with the headwind causes grains to rapidly drain into the star. Growth through this regime must be rapid to avoid substantial loss of grains to the star.

The most promising mechanism for overcoming this issue is local gravitational collapse. If the density of solid particles could somehow be enhanced sufficiently that their gravity locally dominates over that of the star, they would be susceptible to direct gravitational collapse, avoiding hierachical growth in this regime (Goldreich & Ward, 1973). This could be achieved by trapping particles in pressure maxima such as spiral arms, vortices, or the inner disc edge of transition discs (Rice et al., 2004; Pinilla et al., 2015). Turbulent fluctuations produce localised particle enhancements which may be sufficient to trigger the streaming instability driven by relative velocities between gas and solids (Youdin & Goodman, 2005). The subsequent growth of boulders via gravitational collapse is faster than the inspiral time, presenting a solution to the drag problem (Johansen et al., 2007).

Objects which reach a kilometre in size transition to a new growth regime. They are massive enough to perturb the local gravitational field, with gravitational focussing enhancing their effective accretion cross-section. The planetesimal's gravity dominates over that of the protostar out to the Hill radius, $R_H = d\,[M/(3M_*)]^{1/3}$, where d is the orbital radius of the planetesimal, M is its mass, and M_* is the mass of the protostar. This increases the growth rate as it collects an increasingly wider scope of particles, and retains debris from (initially) destructive collisions.

Accretion accelerates with mass so that the earliest objects to form halt the growth of nearby planetesimals by draining their common feeding zone (Kokubo & Ida, 1998). In this way a small number of the largest objects detach from the upper end of the planetesimal mass distribution. By the end of this oligarchic phase, planetesimals are massive enough to disrupt one another's orbit, leading to interactions and ejections. The increase in mutual velocities slows planet growth as successively fewer planetesimals collide with low enough impact to stick (Ida & Makino, 1993).

The largest objects grow into giant planets through the capture of a massive gaseous atmosphere. Initially a loosely bound envelope extends out to the Hill radius, and accretion is limited by the rate at which radiative cooling can remove gravitational energy released from planetesimal accretion and atmospheric contraction (Pollack et al., 1996). Once the mass of the envelope reaches the core mass (typically at $M_{\rm core} \sim 10 M_{\rm Earth}$), gas accretion accelerates and thermal pressure is insufficient to support the envelope. The envelope collapses to roughly the planet's final radius on a time-scale determined by the balance of accretion heating and cooling by energy transport (Mizuno, 1980). Gas flow from the disc continually refills the cavity in a rapid, runaway fashion (Bodenheimer & Pollack, 1986). This rapid growth ends once the accretion rate exceeds the rate at which viscosity can resupply the Hill sphere.

The alternate model of gravitational instability in discs (Kuiper, 1951; Cameron, 1978; Boss, 1997, 2007) may be more appropriate for giant planets forming on wide orbits [i.e., orbital radius $d >$100 au; Boley (2009)]. In the outer regions of massive discs ($M_{\rm disc} \gtrsim 0.1 M_*$) self-gravity of the disc can exceed that of the central object. These regions undergo local gravitational collapse. Perturbations emanating from over-dense regions manifest as spiral arms, which can themselves form self-gravitating clumps (Laughlin & Bodenheimer, 1994). Simulations indicate that up to 50% of fragments survive being sheared apart by the disc to form viable precursors to giant protoplanets (Galvagni & Mayer, 2014). A planetary core is formed out of solids caught up with the gas, yielding an available core mass of 5–10$M_{\rm Earth}$ (Boss, 1997; Forgan & Rice, 2013).

Disc instability requires that self-gravity is strong enough to overcome stabilising pressure waves and tidal forces (Toomre, 1964). This condition is summarised by Toomre's parameter, $Q = c_s \Omega/(\pi G \Sigma)$, where Ω is the orbital angular frequency, c_s is the sound speed, and Σ is the column density. Regions where Toomre's parameter is below the critical value $Q_{\rm crit} \sim 1$ are susceptible to gravitational collapse.

Maintaining a sufficiently cool temperature throughout collapse is challenging, as compression heats the gas and spiral density waves can develop into into shock waves (Nelson, Benz & Ruzmaikina, 2000). Therefore, efficient cooling is needed to radiate away heat generated in the process. Simulations find that the disc must cool within $\sim$ 30 orbits to allow for collapse into a self-gravitating object (Rafikov, 2007; Meru & Bate, 2012; Rice et al., 2014). Otherwise too much heat is retained and the outcome is merely turbulence (Gammie, 2001).

Regardless of how giant planets are formed, unbalanced torques from the disc can alter the planet's orbit (Goldreich & Tremaine, 1979, 1980). In a Keplerian disc angular momentum increases with orbital distance, so that a planet's gain or loss of angular momentum translates into an orbital shift (Lin & Papaloizou, 1986).

Type I orbital migration (Ward, 1986, 1997) occurs in response to the combined influence of Lindblad, corotation and magnetic torques (Goldreich & Tremaine, 1979;

Tanaka, Takeuchi & Ward, 2002; Terquem, 2003). The planet launches spiral density waves which exchange orbital angular momentum as they exert a torque on one another. Material both inside and beyond the planet's orbit exert a torque on the planet, but typically the density asymmetry about the planet's orbit yields a stronger exterior torque. The resulting inward migration time-scale is much shorter than the disc life-time (typically 0.1 Myr; Tanaka, Takeuchi & Ward, 2002), meaning that some planets migrate into the star while survivors are left in tight orbits. If the disc is MRI unstable, turbulent fluctuations introduce a stochastic element to the rate, and potentially even the direction, of migration of low-mass planets (Nelson & Papaloizou, 2004).

Protoplanet accretion slows once the planet grows massive enough to modify the local disc structure. The disc cannot supply the Hill sphere with enough material to sustain runaway gas accretion indefinitely (Bate et al., 2003). Instead the planet drains the disc around it's orbit, evacuating a gap (Lin & Papaloizou, 1986; Bryden et al., 1999). Once a gap has been opened, the planet's accretion rate is limited by the supply of new material into the Hill sphere by viscosity (Lin & Papaloizou, 1986), or orbital migration into fresh material (Alibert et al., 2005).

Gaps are potentially observable once the Hill sphere reaches the disc scale height (Bryden et al., 1999; Crida, Morbidelli & Masset, 2006). Annular gaps have been detected in several young circumstellar discs (e.g., Debes et al., 2013; Garufi et al., 2014; Brogan et al., 2015), and the inferred presence of young substellar companions within gaps strengthens the case for planetary clearing (Quanz et al., 2013; Pineda et al., 2014; Reggiani et al., 2014).

Following the contraction of the envelope, material with too much angular momentum to reach the planet directly enters a circumplanetary disc (Lunine & Stevenson, 1982; Ayliffe & Bate, 2009a). Regular moons (i.e., those with prograde, coplanar, circular orbits) in giant planet satellite systems are strong circumstantial evidence for circumplanetary discs (e.g., see Lunine & Stevenson 1982). Regular moons likely formed within the disc, and so their composition records locally icy conditions in the final stage of the disc's lifetime (Mosqueira, Estrada & Turrini, 2010).

Figure 1.2 shows a composite image of a simulated protoplanetary disc (right; Baruteau et al., 2011), gap and circumplanetary disc (left; adapted from Tanigawa, Ohtsuki & Machida 2012). The disc extends out to a radius of ≈ 0.3–$0.4\,R_H$ as limited by tidal forces (Quillen & Trilling, 1998; Martin & Lubow, 2011b). Very little is known about the structure and evolution of the disc, nor how much of the planet's accretion is delivered through the circumplanetary disc. Recent studies indicate that

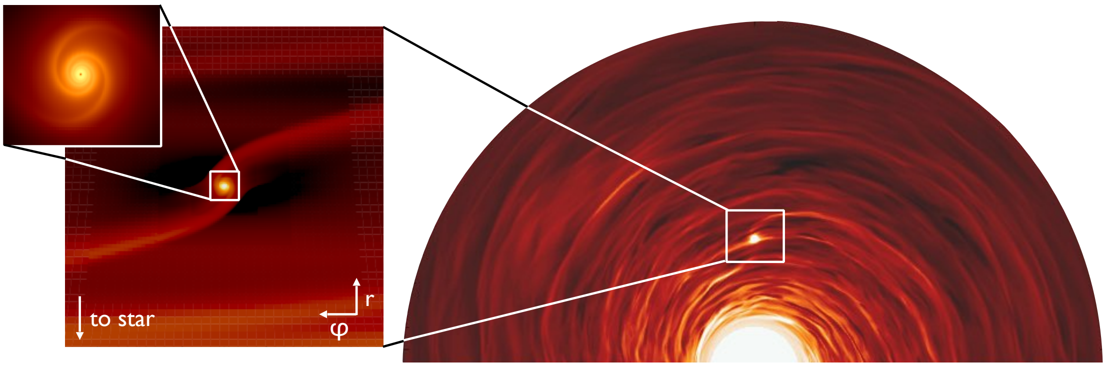

Figure 1.2: Circumplanetary disc and gap in the protoplanetary disc surrounding a giant planet. This gap and circumplanetary disc are adapted from the Tanigawa, Ohtsuki & Machida (2012) hydrodynamical simulation, and the protoplanetary disc is adapted from the Baruteau et al. (2011) magnetohydrodynamical simulation.

circumplanetary discs spend much of their life in a quiescent phase with little inflow (or outflow; Gressel et al., 2013). This is likely punctuated by episodic, potentially hot, accretion events (Martin & Lubow, 2011a; Lubow & Martin, 2012; Turner, Lee & Sano, 2014; Keith & Wardle, 2014).

Gap opening, and the eventual clearing of the disc, alters orbital migration. The strongest contribution to Type I migration torques occurs at resonances located approximately a scale-height either side of the planet's orbital radius (Artymowicz, 1993). By emptying gas at the resonances, gap opening quenches these torques, and ends Type I migration. A new, slower mode of migration takes over; type II migration pulls giant planets toward the star at the viscous inflow speed. This arises from a torque imbalance driven by the accretion of the inner disc onto the central object (Lin & Papaloizou, 1986; Ward, 1997; D'Angelo, Henning & Kley, 2002; Bate et al., 2003).

Even after the disc has dissipated, further orbital evolution is possible through interactions with other planets or remnant planetesimals (Malhotra, 1993; Rasio & Ford, 1996). Planets can drift inward or outward by exchanging angular momentum with other objects in the system. Giant planets are massive and so an interaction with a less massive object can leave the object on an eccentric orbit, or eject it from the system. This may explain why systems with multiple transiting planets are less likely to include a transiting giant planet (Latham et al., 2011).

In our own Solar system, migration of Jupiter and Saturn may have been responsible for limiting Mars' mass by clearing the disc around its orbit (Walsh et al., 2011), exciting eccentricity in the gas giant and ice giant orbits (Tsiganis et al., 2005), and the spike in asteroid collisions in the inner Solar system during the late heavy bombardment (Gomes et al., 2005).

1.2 Protoplanetary discs

Protoplanetary discs set the stage for planet formation; conditions in the disc govern fundamental processes such as gas transport, solid processing and turbulence. Here we give an overview of their properties and evolution.

Protoplanetary discs form along with their host star through the gravitational collapse of a molecular cloud core [radius $\sim 0.1\,\mathrm{pc}$; see McKee & Ostriker (2007) for a review]. Random motions within the cloud produce a small, but non-zero net rotation. Angular momentum conservation amplifies the initial rotation considerably during the collapse, until it is strong enough to balance gravity. As there is no rotational support along the rotation axis, the core flattens into a circumstellar disc. Young circumstellar discs extend out to $d \sim 1000\,\mathrm{au}$, and internal pressure sets the disc height to $H \approx 0.1d$ (Chiang & Goldreich, 1997; Williams & Cieza, 2011). Vertical settling of the cloud is not instantaneous so that the protostar is initially obscured by the envelope (the so-called Class 0 phase with $M_{\mathrm{envelope}} > M_{\mathrm{star}} > M_{\mathrm{disc}}$).

Planet formation probably begins in earnest in the T Tauri phase, following the clearing of the envelope. T Tauri disc masses, inferred from submillimetre dust mass measurements, are only 1% of the protostellar mass (Williams & Cieza, 2011). This is consistent with the standard model of the pre-Solar nebula, the minimum mass Solar nebula, which is produced by augmenting the solid material in the planets with enough hydrogen and helium gas to bring it up to Solar composition (Weidenschilling, 1977; Hayashi, 1981; Desch, 2007). The mass is redistributed between the planets into a disc accounting for the differing planet core masses and migration history. This yields a column density of $140\,\mathrm{g\,cm^{-2}}$ at the present-day orbital radius of Jupiter. Incident starlight produces a blackbody temperature profile $T \approx 280(d/\mathrm{au})^{-1/2}$, although accretion heating may exceed this within the inner $\sim 6\,\mathrm{au}$ if the energy is dissipated locally (Dullemond et al., 2007).

Active stellar accretion in the T Tauri phase is evident through Hα and ultraviolet emission. Accretion is typically at the level of $\dot{M} = 10^{-8}\,M_{\odot}/\mathrm{year}$ (Williams & Cieza, 2011), although many young stellar objects [e.g., FU Orionis (Herbig, 1977; Hartmann & Kenyon, 1996), EX Lupis (Herbig, 1989, 2007), and Herbig-Haro objects (Bally, Reipurth & Davis, 2007)] show considerable brightness variability attributed to accretion outbursts of up to $\dot{M} = 10^{-3}\,M_{\odot}$/year. Accretion can also be accompanied by outflows (Hartigan, Edwards & Ghandour, 1995), likely in the form of magnetic disc winds or magnetospheric X-winds (Blandford & Payne, 1982; Wardle & Königl, 1993; Shu et al., 1994).

The disc inherits a magnetic field from the progenitor molecular cloud. A large-scale poloidal field is drawn into the disc, wound up by the rotation, and may be subject to turbulence. Unfortunately, very little is known about magnetic field in protoplanetary discs, let alone in the planet forming region. High extinction prevents polarisation measurements of background stars, and measured polarisation of sub-millimeter dust thermal emission is very low (polarisation $< 1\%$). Nevertheless high sensitivity, spatially resolved (up to 80 au) dust polarisation maps around Class 0 (Rao et al., 2014) and T Tauri (Stephens et al., 2014) discs have been used to detect (complex) structure. Non-thermal broadening of molecular line emission reveal the presence of super-sonic turbulence in the far outer disc ($d \sim 100$ au; Hughes et al., 2011; Guilloteau et al., 2012), and ALMA observations should shed light on how turbulence varies with height (Simon et al., 2015).

The field is certainly compressionally enhanced over the cloud field ($B \sim 1$–100 mG; Shu, Adams & Lizano, 1987), while the equipartition field $B_{\rm eq} = 8\pi p \sim 18$ G at $d = 1$ au provides a maximum field strength the disc will support before magnetic forces exceed the thermal pressure, p (Wardle, 2007). Meteorites record a primordial magnetic field of ≈ 0.5 G, however it is debatable whether this corresponds to the ambient field in the disc or to the dynamo field generated in the interior of the object's progenitor (Weiss et al., 2010; Fu et al., 2014).

Protoplanetary discs are eventually cleared through accretion and photoevaporation after 2–3 million years following the embedded phase (Williams & Cieza, 2011).

1.3 Accretion processes in protoplanetary discs

Accretion governs conditions in protoplanetary discs, and is a key element of planet formation models. The challenge of accretion disc theory is to identify the mechanism by which angular momentum is lost. Angular momentum can be carried away by a small fraction of the material, allowing for accretion the of bulk of the disc. The observed low disc-to-protostar mass ratio indicates that this process is relatively efficient. Viscous diffusion from intrinsic molecular viscosity is too slow ($t = l^2/\nu \approx 3 \times 10^7$ years; e.g. Pringle, 1981; Balbus, 2003) to account for observed accretion and so another process is needed.

Turbulence is a source of (effective) viscosity. Pure-hydrodynamical turbulence is ruled out in Keplerian discs, as their radially increasing angular momentum profile renders them stable to hydrodynamical instabilities (Rayleigh, 1917). Shakura & Sunyaev (1973) circumvented this issue by appealing to another unspecified process, assumed to be magnetic, to generate turbulence. From this standpoint they developed a simplified description of the turbulent inflow, assuming turbulence is subsonic and confined within the disc scale-height. The resulting prescription for the viscosity, $\nu = \alpha c_s H$, combines the considerable uncertainty in properties of astrophysical turbulence into an efficiency parameter, $\alpha < 1$.

Much of the headway in analytical accretion disc theory can be attributed to the α prescription. Observational estimates derived from the inferred mass accretion rates of T-Tauri stars, and the time-dependent behaviour of FU Orionis outbursts, dwarf nova, and X-ray transients, indicate $\alpha \sim 10^{-2}$–10^{-1} [see King, Pringle & Livio (2007) and references therein]. Yet, while the α-prescription is a useful tool, the challenge is in the physics causing the effective α. Ultimately this requires detailed calculations and simulations for specific mechanisms.

Hydromagnetic turbulence driven by the magnetorotational instability (MRI) is the most promising candidate for the accretion mechanism in protoplanetary discs (Velikhov, 1959; Chandrasekhar, 1960; Balbus & Hawley, 1991). The MRI converts free energy available in differential rotation of the disc into runaway growth of a small-scale radial seed magnetic field from a weak (i.e., subthermal) poloidal magnetic field (Balbus & Hawley, 1991). It is an efficient transport mechanism with numerical magnetohydrodynamical shearing box simulations finding an effective $\alpha \sim 10^{-3}$–10^{-1} (King, Pringle & Livio, 2007; Lesur & Longaretti, 2009).

Growth in the linear phase is simply illustrated by radially displacing parcels connected by a vertical field. If the field is pulled along with the displaced fluid, it develops a small radial component. Parcels which are displaced towards the star enter a faster orbit than those which moved outward and so the field is further bent in the azimuthal direction. This creates magnetic tension resisting the developing field gradients, which pulls the inward fluid element back, and outward element forward. This redistributes angular momentum between fluid elements connected by the field, leading to an outward transport of angular momentum and inward transport of mass (Balbus & Hawley, 1992; Hawley, Gammie & Balbus, 1995). This is a runaway process which develops into turbulence in the non-linear regime.

Hydrodynamical transport mechanisms may also be at work. Fragments in a gravitationally-unstable disc launch spiral density waves. Waves interacting with one another can transport angular momentum (Johnson & Gammie, 2006), and gravitationally unstable discs can undergo accretion outbursts (Vorobyov & Basu, 2015). If the disc cools too slowly to fragment, marginally unstable discs can be turbulent with an effective alpha of $\alpha \approx 0.01$ (Meru & Bate, 2012). Vortices created by radial pressure gradients (Goldreich & Schubert, 1967; Fricke, 1968), or entropy gradients (Klahr & Bodenheimer, 2003), can operate in magnetically-inactive regions (Lyra & Klahr, 2011).

Magnetic torques from large-scale, ordered fields are a promising alternative to turbulent accretion. Large-scale fields can extract momentum from the disc in two key ways. In a magnetocentrifugal wind, gas is flung out along strong (i.e., equipartition or super-equipartion), poloidal field lines inclined to the rotational axis by at least 30° (Blandford & Payne, 1982; Wardle & Königl, 1993). As the wind is accelerated to faster than the Alfvén speed, inertia of gas is so strong that it winds the field line into a helix. In this scenario it is the wind which carries angular momentum away from the disc. Outflows, indicated by doppler shifting of CO lines, are common in discs around young stars (Li et al., 2014).

Alternatively, the disc may be magnetically-braked if the field is anchored into an external medium. In a magnetic braking model the field exerts a torque on an external medium such as the surrounding molecular cloud (Matsumoto & Tomisaka, 2004). The angular momentum transferred to the cloud has a negligible effect in its rotation as it is much more massive than the disc. Consequently, the cloud pulls back on the field, and subsequently braking the disc.

Of course, disc accretion need not be steady. Limit-cycles in the accretion rate can occur as the accretion efficiency and inflow mechanism evolve over time. For example, the thermal-viscous instability allows for rapid expansion of the inner, thermally-ionised accreting region if the disc transitions between two H-scattering opacity branches (Hartmann & Kenyon, 1985, 1996; Bell et al., 1997). Alternatively, if the local supply rate exceeds the inflow rate (e.g., in weakly-accreting MRI 'dead zones') gas pile-up may occur to the extent that the region becomes self-gravitating, triggering gravitational instability. Associated heating could periodically revive MRI turbulence leading to an accretion outburst (Armitage, Livio & Pringle, 2001; Martin & Lubow, 2011a; Lubow & Martin, 2012).

Studies of protoplanetary disc accretion have typically focussed on the efficiency and extent of magnetically-driven accretion across the disc. Magnetic diffusion, caused by collisions at the microphysical level, poses the greatest challenge to accretion driven by magnetic fields as it decouples the evolution of the field and gas.

1.4 Non-ideal magnetohydrodynamics

The requirement of magnetic coupling is a major caveat of magnetically-driven accretion. Magnetic coupling describes an anchoring of field lines into gas so that they evolve together. In this state a magnetic field is advected with the fluid faster than it diffuses away. This facilitates the disc-field interaction necessary for the growth of magnetic field structures employed for magnetic accretion processes, such as the runaway field buckling for the MRI.

However, collisions between neutral and charged particles compromise magnetic flux-freezing in protoplanetary discs (Wardle, 2007). In a conducting, magnetised fluid, charged particles accelerate along the electric field, $\mathbf{E}$ and gyrate around the magnetic field, $\mathbf{B}$. This introduces a relative $\mathbf{E} \times \mathbf{B}$ velocity between charged and neutral species. Collisions between ions and neutrals resist the differential velocity by exerting a drag force. If the neutral density is high enough that collisional drag dominates the Lorentz force then charges are carried along with the neutrals. Some degree of field-line drift is beneficial as it allows gas to be accreted without advecting the field into the disc interior (Wardle & Königl, 1993). However, if drift is too strong the effect is to wash out the response of charged particles to the magnetic field.

The transition between ideal and drag-dominated regimes occurs at different densities for electrons and ions. This leads to three different 'non-ideal' effects:

1. *Ohmic resistivity* - in high density, weakly magnetised regions (e.g, the inner disc midplane), drag decouples both electrons and ions from the magnetic field and the field diffuses away.
2. *Ambipolar diffusion* - a low density, strongly magnetised fluid (e.g, in the outer disc, or in surface layers) yields insufficient drag to decouple either the electrons or ions from the magnetic field. The field is tied to the ionised component of the fluid and together they drift through the neutrals.
3. *Hall drift* - at intermediate densities/field strengths, drag decouples ions from the field, but the field remains frozen into the electrons fluid.

Ohmic resistivity and ambipolar diffusion tend to inhibit magnetically-driven accretion. Typically they cooperate to resist small-scale field structure by smoothing out gradients with a length-scale smaller than η/v_a, where η is the transport coefficient associated with the non-ideal effects, and v_a is the Alfvén speed. They pose an obvious threat to small-scale structure induced by turbulence. If non-ideal effects wash out field gradients at the wavelength of the fastest growing MRI mode the growth-rate can be lowered substantially (Jin, 1996; Sano & Miyama, 1999). Global and shearing-box simulations confirm the quenching of the MRI in the presence of strong Ohmic resistivity and ambipolar diffusion [see Turner et al. (2014) for a review].

Hall drift behaves in a fundamentally different way to Ohmic resistivity and ambipolar diffusion. In Hall MHD field drift is along the current, and can suppress or enhance field gradients. The outcome depends on the orientation of the global poloidal field relative to the rotation axis. For example, Hall drift co-operates with shear in MRI field buckling if the magnetic field is in the same direction as the disc rotation axis (Wardle, 1999; Balbus & Terquem, 2001; Kunz & Lesur, 2013; Lesur, Kunz & Fromang, 2014). In fact, Hall drift in a favourable orientation can destabilise the disc, even when dominated by Ohmic resistivity and ambipolar diffusion (Wardle & Salmeron, 2012). The converse is also true: Hall drift associated with a field antiparallel to the rotation axis counteracts shear and stabilises the disc against the MRI. This field-orientation dependence is also evident in theoretical models of Hall-dominated magnetocentrifugal outflows, as it influences the range parameter-space with viable solutions (Königl, Salmeron & Wardle, 2010; Salmeron, Königl & Wardle, 2011), and may result in a bimodal population of circumstellar discs as it influences magnetic braking (Krasnopolsky, Li & Shang, 2011; Li, Krasnopolsky & Shang, 2011; Tsukamoto et al., 2015).

Non-ideal effects are strong in poorly ionised regions. Protoplanetary discs are weakly ionised throughout and so the impact is considerable (Wardle, 2007).
Magnetically-driven accretion is confined to ionised, so-called 'active' regions, giving rise to the 'layered-accretion' model (Gammie, 1996). These are (i) the thermally ionised, inner $d \lesssim 1\,\mathrm{au}$, where temperature exceeds $T = 1000\,\mathrm{K}$, and (ii) surface layers (column density 0.1–$100\,\mathrm{g\,cm^{-2}}$) which are ionised by absorption of cosmic rays, stellar X-rays and ultraviolet radiation (Igea & Glassgold, 1999; Turner & Sano, 2008; Perez-Becker & Chiang, 2011). Additional, pervasive sources of ionisation, such as radioactive decay of short-lived radioactive isotopes are too weak to alter magnetic coupling (Umebayashi & Nakano, 2009).

The result is an MRI-inactive 'dead zone' in the critical planet-forming region at the midplane between $d = 1$–$10\,\mathrm{au}$. Although there is no observational evidence confirming (or denying) the existence of 'dead zones', it has overwhelming support from theoretical studies. Instead, other mechanisms, such as disc winds or hydrodynamical transport, may very well operate there instead (Lyra & Klahr, 2011; Bai & Stone, 2013).

1.5 Thesis aim and outline

The critical role of magnetic fields in protoplanetary disc dynamics highlights the need to investigate the role of magnetic fields in giant planet formation. Magnetic fields are not only at work in the evolution of the wider protoplanetary disc; a magnetic field drawn into a gap and circumplanetary disc can influence the flow with implications for planet and satellite growth. Despite this, very little has been done to assess the role of magnetic fields in the critical gas capture zone supplying accretion to the planet.

This thesis addresses the influence of magnetic fields and non-ideal effects in three aspects of giant planet formation: circumplanetary disc accretion, dynamics of the gas captured from protoplanetary discs by a giant planet, and magnetic-braking in accretion discs.

The first study focusses on accretion in circumplanetary discs, and the uncertainty in the role of the MRI. In Chapter 2 we assess the potential for steady-state accretion arising from hydromagnetic turbulence, large-scale magnetic fields, and turbulence driven by gravitational instability. We model the disc by a Shakura-Sunyaev α-disc, and adjust the accretion efficiency (i.e., α) to self-consistently match the effectiveness of the inflow mechanisms. We consider whether the resulting steady state solution is a realistic, viable option, or whether the disc would need to be modelled by an evolving system (e.g., MRI-Gravitational limit cycles; Martin & Lubow, 2011a; Lubow & Martin, 2012). This chapter is closely based on the published paper 'Accretion in giant planet circumplanetary discs' (Keith & Wardle, 2014).

The second study considers the interaction of magnetic fields drawn into the gap with the inflowing gas. Lowered density in the gap enhances the chance that flow is MRI turbulent, and that magnetic forces from large-scale fields are dynamically important. In Chapter 3 we present a detailed investigation of gap magnetic field structure as determined by non-ideal effects. We determine the susceptibility to turbulence induced by the MRI, and angular momentum loss from large-scale fields. Simulations are needed to capture the complex flow in the gap but full non-ideal simulations are computationally expensive. Therefore we take an a posteriori approach, estimating MHD quantities from the high resolution, pure-hydrodynamical, gap-crossing simulation by Tanigawa, Ohtsuki & Machida (2012). This allows us to calculate the ionisation fraction and the strength of non-ideal effects. This chapter is closely based on the published paper 'Magnetic fields in gaps surrounding giant protoplanets' (Keith & Wardle, 2015).

The final study investigates protoplanetary disc accretion driven by large-scale magnetic fields. A magnetic braking model is used, in which a magnetic field carries away angular momentum and magnetic torques decelerate the disc. In Chapter 4, we construct a one-dimensional, axisymmetric model of the radial structure of such a disc. A magnetic field is embedded in the disc, and is connected to a force-free atmosphere above and below the disc. An equilibrium model is developed in which non-ideal effects provide the necessary field-line drift relative to accreting gas. We perform a linear perturbation analysis for local radial modes, to determine the stability of the equilibrium model, and assess the susceptibility to accretion outbursts.

Finally, Chapter 5 discusses the overall thesis results and presents conclusions and prospects for future work.

2

Magnetically-driven accretion in giant planet circumplanetary discs

2.1 Introduction

Gas giant planets form within a protoplanetary disc surrounding a young star (Lin & Papaloizou, 1985). Those orbiting within $\sim 100\,\mathrm{au}$ of the star are thought to form through the aggregation of a $\sim 15 M_{\mathrm{Earth}}$ solid core and subsequent gas capture from the surrounding disc (Pollack et al., 1996; Boley, 2009). During the initial slow accretion phase the protoplanet envelope is thermally supported and distended. However, once the envelope mass reaches the core mass gas accretion accelerates rapidly and, unable to maintain thermal equilibrium, the envelope collapses (Pollack et al., 1996; Lissauer et al., 2009). This 'run-away' gas accretion ends once the planet is massive enough that it accretes faster than gas can be replenished into its vicinity. Infalling gas has too much angular momentum to fall directly onto the contracted planet, and so an accretion disc, the circumplanetary disc, forms around the planet (Lunine & Stevenson, 1982; Ayliffe & Bate, 2009a).

In contrast to the icy conditions implied by satellite systems around Solar System giant planets, circumplanetary discs are likely initially hot and convective (Coradini et al., 1989). Most of the protoplanet's mass is delivered during run-away accretion and so the circumplanetary disc must support a high inflow rate during this phase.

The formation of Jupiter consistent with the giant planet formation time-scale inferred from the life-time of protoplanetary discs (life-time $\sim 3 \times 10^6$ years; Williams & Cieza, 2011) suggests an inflow rate of $\dot{M} \sim 10^{-6} M_J$/year, where M_J is the mass of Jupiter.

Models of the accretion phase of a circumplanetary disc include self-luminous discs (Quillen & Trilling, 1998; Fendt, 2003; Nelson & Benz, 2003), Shakura-Sunyaev α discs (Canup & Ward 2002, 2006; Alibert, Mousis & Benz, 2005; Turner, Lee & Sano, 2014), time-dependent discs with MRI-Gravitational instability limit cycles (Martin & Lubow, 2011a; Lubow & Martin, 2012), and hydrodynamical simulations (Lubow, Seibert & Artymowicz, 1999; D'Angelo, Henning & Kley, 2002, 2003; Machida et al., 2008; Ayliffe & Bate, 2009a,b; Machida, 2009; Rivier et al., 2012; Tanigawa, Ohtsuki & Machida, 2012; Shabram & Boley, 2013). The evolution of the disc associated with the contraction of the proto-planetary envelope and changes in the mode of accretion from the protoplanetary disc have also been addressed (Ward & Canup, 2010).

The angular momentum transport mechanism is key in determining the disc structure and evolution, yet little work has been done to model the disc self-consistently with the accretion mechanism. The α-model invokes a source of viscosity (typically hydromagnetic turbulence is suggested) however there is no guarantee that the resulting disc complies with the conditions required for viscosity, hydromagnetic or otherwise. An exception is the time-dependent gravo-magneto outbursting cycles modelled by Lubow & Martin (2012), however numerical simulations suggest discs rapidly evolve away from a gravitationally unstable state (Shabram & Boley, 2013).

There are a variety of candidates for the accretion mechanism, including magnetic forces, gravitational instability, thermally-driven hydrodynamical instabilities, torques from spiral waves generated by satellitesimals [see Papaloizou & Lin, 1995 and Turner et al. (in preparation) for a review], and stellar forcing (Rivier et al., 2012). Magnetic fields and gravitational instability are generally considered the most promising mechanisms within the protoplanetary disc.

Magnetically-driven accretion may result from hydromagnetic turbulence produced by the magnetorotational instability (MRI; Balbus & Hawley, 1991; Hawley, Gammie & Balbus, 1995), centrifugally-driven disc winds associated with large-scale poloidal fields (Blandford & Payne, 1982; Wardle & Königl, 1993), or magnetic braking (Matsumoto & Tomisaka, 2004). MRI turbulence has been modelled extensively (e.g., Gammie, 1996; Sano et al., 2004; Turner, Sano & Dziourkevitch, 2007; Flaig et al., 2012; Wardle & Salmeron, 2012; Parkin & Bicknell, 2013) and simulations of MRI transport in protoplanetary discs indicate $\alpha \sim 10^{-3}$, where α is the Shakura-Sunyaev viscosity parameter (Shakura & Sunyaev, 1973; King, Pringle & Livio, 2007). Gravitational instability occurs in massive discs and may cause fragmentation or gravitoturbulence (Toomre, 1964; Gammie, 2001).

Certain conditions are required for these mechanisms to be effective. For example, magnetic processes can only act in sufficiently ionised 'active' regions, where the evolution of the magnetic field is coupled to the motion of the disc. If the ionisation fraction is too low, magnetic diffusivity decouples their motion (e.g. Wardle, 2007). In protoplanetary discs, magnetic coupling is strong enough to permit MRI accretion in two regions: (i) layers above the midplane where cosmic rays, and stellar X-rays and UV photons penetrate, and (ii) close to the star where the disc is hot and thermally ionised (Gammie, 1996). Gravitational instability requires strong self-gravity such that Toomre's stability parameter $Q \lesssim 1$, and quasi-steady gravoturbulent accretion further requires a cooling time-scale in excess of ~ 30 orbital time-scales (Meru & Bate, 2012; Paardekooper, 2012).

Existing steady-state models of circumplanetary discs are not massive enough for gravitational instability, and so testing for self-consistent accretion has focussed on identifying regions which are susceptible to the MRI. Fujii, Okuzumi & Inutsuka (2011) determined the thickness of the magnetically-uncoupled Ohmic midplane 'dead zone' of an α disc for cosmic ray ionisation. They find that a dead zone extends up at least 2.5 scale heights (for plasma $\beta = 10^4$) with the presence of grains extending this region to even greater heights.

These results agree with the findings of Turner, Lee & Sano (2014) which also included ionisation from X-rays, radioactive decay, turbulent mixing, thermal ionisation as well as cosmic rays, and accounted for Ambipolar and Ohmic diffusion. They found that α discs are magnetically-coupled in surface layers above ~ 3 scale heights unless the disc is dusty and is shielded from X-rays. They also considered magnetic coupling in the Jovian analogue to the Minimum Mass Solar Nebula - the Minimum Mass Jovian Nebula (MMJN; Mosqueira & Estrada, 2003), finding that dust must be removed for magnetically coupled surface layers. They found that thermal ionisation in actively supplied discs may permit coupling within the inner $4\,R_J$ of the midplane, although Fendt (2003) suggest a larger thermally ionised region ($r \lesssim 65\,R_J$).

Either way, we conclude that current α models of circumplanetary discs are not necessarily susceptible to the magnetically driven accretion assumed at all radii, and that magnetically active surface layers may be too high above the midplane to carry the required accreting column.

In this chapter, we probe the viability of self-consistent steady-state accretion through the circumplanetary disc midplane, with accretion driven by magnetic fields and gravitoturbulence. We model the disc as a Shakura-Sunyaev α disc and solve for the disc structure self-consistently with the opacity using the Zhu, Hartmann & Gammie (2009) opacity-law (§2.2). In §2.3 we calculate the ionisation level produced by thermal ionisation, cosmic rays, and radioactive decay, and also consider the effectiveness of turbulent mixing (Ilgner & Nelson, 2006; Turner, Sano & Dziourkevitch, 2007; Ilgner & Nelson, 2008), and Joule heating in resistive MRI regions (Inutsuka & Sano, 2005; Muranushi, Okuzumi & Inutsuka, 2012). We determine the magnetic field strength needed for accretion by an MRI or large-scale vertical field (§2.4), and calculate Ohmic, Hall and Ambipolar diffusivities to determine the strength of magnetic coupling (§2.5).

Motivated by the failure of the standard constant-α disc (§2.6.1) to produce magnetic coupling consistent with the assumed viscosity profile, we present an alternate α disc (§2.6.2); we allow the level of magnetic transport (i.e., α) to vary radially, consistent with the level of viscosity produced by either magnetic forces or gravitational instability. We use the Sano & Stone (2002) prescription for α to quantify non-ideal magnetic transport. We present the results in §2.7, with a summary and discussion of findings in §2.8.

2.2 Disc structure

We model a circumplanetary disc as an axisymmetric, radiative, thin disc surrounding a protoplanet of mass M, in orbit around a star of mass M_*, at an orbital distance d. The disc extends out to a radius $r = R_H/3$ around the planet, where

$$\begin{aligned} R_H &= d\left(\frac{M}{3M_*}\right)^{\frac{1}{3}} \\ &\approx 743\,R_J\left(\frac{d}{5.2\,\mathrm{au}}\right)\left(\frac{M}{M_J}\right)^{\frac{1}{3}}\left(\frac{M_*}{M_\odot}\right)^{-\frac{1}{3}} \end{aligned} \tag{2.1}$$

is the Hill radius, R_J is the radius of Jupiter, M_J is the mass of Jupiter, and $M_\odot$ is the mass of the Sun (Quillen & Trilling, 1998; Martin & Lubow, 2011b).

The scale height, H, is determined by a balance between thermal pressure, the planet's gravity, and self-gravity of the disc. Toomre's Q quantifies the strength of self-gravity (Toomre, 1964),

$$\begin{aligned} Q &= \frac{c_s \Omega}{\pi G \Sigma} \\ &\approx 5.3 \times 10^3 \left(\frac{T}{10^3\,\mathrm{K}}\right)^{\frac{1}{2}} \left(\frac{\Sigma}{10^2 \mathrm{g\,cm^{-2}}}\right)^{-1} \left(\frac{M}{M_J}\right)^{\frac{1}{2}} \left(\frac{r}{10^2\,R_J}\right)^{-\frac{3}{2}}, \end{aligned} \tag{2.2}$$

with $Q \gg 1$ if self-gravity is negligible and $Q \ll 1$ where self-gravity is important. Here, Σ is the column density, Ω is the Keplerian angular velocity,

$$\Omega = \sqrt{\frac{GM}{r^3}} \approx 5.9 \times 10^{-7}\,\mathrm{s^{-1}} \left(\frac{r}{10^2\,R_J}\right)^{-\frac{3}{2}} \left(\frac{M}{M_J}\right)^{\frac{1}{2}}, \tag{2.3}$$

$c_s = \sqrt{kT/m_n} \approx 1.9\,\mathrm{km\,s^{-1}}\sqrt{T/1000\,\mathrm{K}}$ is the isothermal sound speed with $m_n = 2.34 m_p$ the mean neutral particle mass for a H/He gas at temperature T, m_p the proton mass, and k is Boltzmann's constant. Solving for the scale height for arbitrary Q is complex [e.g, see Paczynski, 1978], and so we adopt the simplified equation of vertical equilibrium (c.f., Krasnopolsky & Königl, 2002)

$$\Omega^2 H^2 + \pi G H \Sigma - c_s^2 = 0, \tag{2.4}$$

with solution

$$H = \frac{2Q}{1 + \sqrt{1 + 4Q^2}} \frac{c_s}{\Omega}. \tag{2.5}$$

This reduces to the standard approximations

$$\begin{aligned} \frac{H}{r} &= \frac{c_s}{r\Omega} \\ &\approx 0.45 \left(\frac{T}{10^3\,\mathrm{K}}\right)^{\frac{1}{2}} \left(\frac{r}{10^2\,R_J}\right)^{\frac{1}{2}} \left(\frac{M}{M_J}\right)^{-\frac{1}{2}} \end{aligned} \tag{2.6}$$

for low mass discs (i.e., $M_{\mathrm{disc}} \ll M_J$) where self-gravity is negligible, and (Pringle, 1981; see footnote[1])

$$\begin{aligned} \frac{H}{r} &= \frac{c_s^2}{\pi G \Sigma r} \\ &= Q \frac{c_s}{r\Omega} \\ &\approx 2.4 \times 10^{-2} \left(\frac{T}{10^2\,\mathrm{K}}\right) \left(\frac{\Sigma}{10^6\,\mathrm{g\,cm^{-2}}}\right)^{-1} \left(\frac{r}{10^2\,R_J}\right)^{-1} \end{aligned} \tag{2.7}$$

[1] We have adopted a larger column density than the standard value, $\Sigma = 10^2\,\mathrm{g\,cm^{-2}}$, in equation (2.7) to reflect the higher surface density needed for the disc to enter a self-gravitating state.

for massive, cool, self-gravitating discs. From this we estimate the vertically-averaged neutral mass density

$$\begin{aligned}\rho &= \frac{\Sigma}{2H}, \\ &\approx 6.2\times10^{-9}\,\mathrm{g\ cm^{-3}}\left(\frac{\Sigma}{10^2\,\mathrm{g\,cm^{-2}}}\right)\left(\frac{T}{10^3\,\mathrm{K}}\right)^{-\frac{1}{2}}\left(\frac{r}{10^2\,R_J}\right)\left(\frac{M}{M_J}\right)^{-\frac{1}{2}},\end{aligned} \tag{2.8}$$

and the associated number density, $n = \rho/m_n \approx 2.6\times10^{15}\,\mathrm{cm^{-3}}\ (\rho/10^{-8}\,\mathrm{g\,cm^{-3}})$.

The thermal structure of the disc is governed by dissipation driven by the inflow. We use the standard plane-parallel stellar atmosphere model (Hubeny, 1990),

$$\sigma T^4 = \frac{3}{8}\tau\sigma T_s^4, \tag{2.9}$$

to calculate the midplane temperature T from the surface temperature T_s and optical depth τ from the midplane to the surface. Gravitational binding energy released during infall results in a surface temperature (Pringle, 1981)

$$\begin{aligned}T_s &= \left(\frac{3\dot{M}\Omega^2}{8\pi\sigma}\right)^{\frac{1}{4}} \\ &\approx 82\,\mathrm{K}\left(\frac{\dot{M}}{10^{-6}\,M_J/\mathrm{year}}\right)^{\frac{1}{4}}\left(\frac{M}{M_J}\right)^{\frac{1}{4}}\left(\frac{r}{10^2\,R_J}\right)^{-\frac{3}{4}},\end{aligned} \tag{2.10}$$

where $\dot{M}$ is the inflow rate, and σ the Stefan-Boltzmann constant. We consider a uniform, steady, inward mass flux throughout the disc.

Shock heating of infalling material colliding with the disc contributes additional heating, however it is negligible compared to that of the viscous dissipation [i.e., flux ratio: $F_{\mathrm{infall}}/F_{\mathrm{viscous}} < 10^{-4}$; Cassen & Moosman (1981)]. Similarly, irradiation from the hot young planet [$T_J = 500\,\mathrm{K}$ determined from pure contraction of the young planet; e.g. Hubbard, Burrows & Lunine (2002)] and the accretion hot spot [$T_{\mathrm{hotspot}} = 3300\,\mathrm{K}$ calculated using equation (3.3) in Pringle (1977)] is also negligible with $F_{\mathrm{planet}}/F_{\mathrm{viscous}} < 10^{-4}$ and $F_{\mathrm{hotspot}}/F_{\mathrm{viscous}} < 10^{-2}$ determined using equation (21) from Turner, Lee & Sano (2014).

Equations (2.9) and (2.10) are applicable in optically-thick regions of the disc (i.e., where optical depth $\tau \gg 1$). This is appropriate for the midplane, as the high column density favours a large optical depth:

$$\tau = \kappa\Sigma/2 \gg 1. \tag{2.11}$$

Table 2.1: Coefficient and index, in each opacity regime, for the opacity law $\kappa = \kappa_i\, \rho^a\, T^b$, as given in Table 3 of Bell & Lin (1994) and Table 1 of Zhu, Hartmann & Gammie (2009). The resulting opacity has units of $\mathrm{cm}^2\,\mathrm{g}^{-1}$. See equation (2.12) and Fig. 2.1 for the boundaries of the opacity regimes.

Bell & Lin (1994)				Zhu et al., (2009)			
Opacity Regime	κ_i	a	b	Opacity Regime	κ_i	a	b
Ice grains	2×10^{-4}	0	2	Grains	5.3×10^{-2}	0	0.74
Ice grain evaporation	2×10^{16}	0	-7	Grain evaporation	1.0×10^{145}	1.3	-42
Metal grains	0.1	0	1/2	Water vapour	1.0×10^{-15}	0	4.1
Metal grain evaporation	2×10^{81}	1	-24		1.1×10^{64}	0.68	-18
Molecules	10^{-8}	2/3	3	Molecules	5.1×10^{-11}	0.50	3.4
H scattering	10^{-36}	1/3	10	H scattering	8.9×10^{-39}	0.38	11
Bound–free and free–free	1.5×10^{20}	1	$-5/2$	Bound–free and free–free	1.1×10^{19}	0.93	-2.4
Electron scattering	0.348	0	0	Electron scattering	0.33	0	0
				Molecules and H scattering[a]	1.4	0	3.6

[a] This regime is given in the footnote of Table 1 in Zhu, Hartmann & Gammie (2009). The dominant sources of opacity in this regime are molecular lines and H scattering (Z. Zhu 2013, private communication).

To calculate the opacity, κ, we use the analytic Rosseland mean opacity law presented in Zhu, Hartmann & Gammie (2009). This is a piecewise power-law fit to the Zhu et al. (2007, 2008) opacity law. We give this in Table 2.1, re-expressed as a function of temperature and density, using the ideal gas law[2]. This model features nine opacity regimes, incorporating the effects of dust grains, molecules, atoms, ions and electrons. The transition temperature $T_{j\to k}$ between regimes j and k, as a function of density, is obtained by equating the opacity in neighbouring regimes (i.e., $\kappa_j = \kappa_k$), and is

$$T_{j\to k} = \left(\frac{\kappa_{i,j}}{\kappa_{i,k}}\right)^{\frac{1}{b_k - b_j}} \rho^{\frac{a_j - a_k}{b_k - b_j}}, \tag{2.12}$$

with two additional constraints:

1. use Grain opacity for $T < 794\,K$, and
2. use Molecules and H scattering opacity for $2.34 \times 10^4 \kappa^{0.279}\,K < T < 10^4\,K$.

[2] We have used the mean particle mass of molecular H/He gas in the conversion from pressure to density even though it is not strictly valid where hydrogen is ionised. Hydrogen is only ionised within the inner $5\,R_J$, at temperatures above 3000 K, and we find that correcting the mean particle mass (to $\mu = 1.24$) leads to at most a 15% change in the temperature in this region.

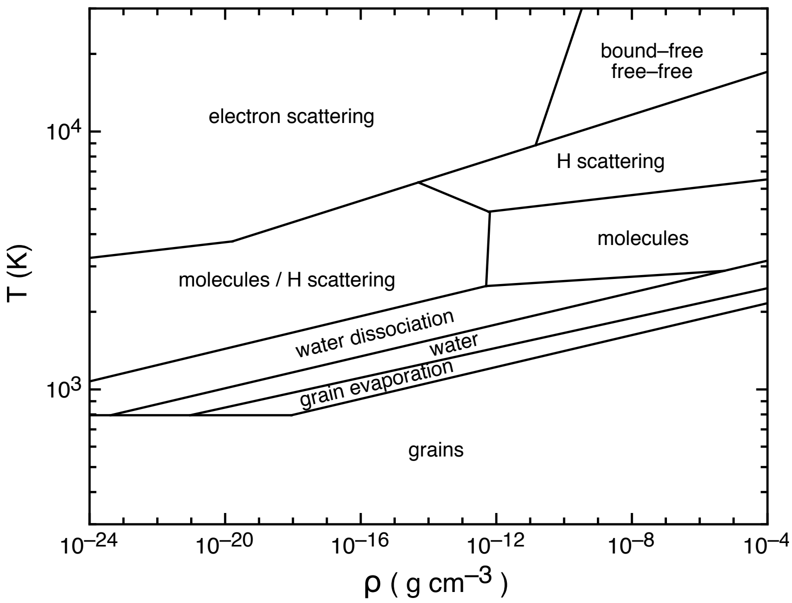

Figure 2.1: Temperature and density boundaries of the Zhu, Hartmann & Gammie (2009) opacity regimes, given in Table 2.1, calculated with equation (2.12).

We show the temperature and density boundaries for each opacity regime in Fig. 2.1.

For comparison, we also give the Bell & Lin (1994) opacity law in Table 2.1. This opacity law underestimates the opacity for temperatures $T \sim$1500–3000 K because it neglects contributions from TiO and water lines longward of 5μm (Alexander & Ferguson, 1994; Semenov et al., 2003; Zhu, Hartmann & Gammie, 2009). The discrepancy is greatest at $\sim$ 1700 K where the Bell & Lin opacity is a factor $\sim$ 500 too low, as compared with the Zhu, Hartmann & Gammie model.

We solve for the local structure (i.e., Σ and T) simultaneously with the opacity, at each radius. Following Bell et al. (1997), we solve for the radial temperature profile by combining equations (2.2), (2.3), (2.5), (2.9) – (2.11) and the opacity law in Table 2.1, to give

$$T^{4-b} = \frac{9\dot{M}\kappa_i}{2^{a+7}\pi\sigma}\Omega^2 H^{-a}\Sigma^{a+1}, \tag{2.13}$$

with a, b, and κ_i specified for each opacity regime. This relationship allows us to describe the disc temperature and column density self consistently, when one or the other is specified.

At a given radius, we solve this equation within each opacity regime, and determine whether the resulting temperature and density fall within the limits of that regime. Solutions which do not fall within these limits are discarded. The solution is not necessarily unique, as the disc may satisfy the conditions of multiple opacity regimes (e.g., Bell & Lin, 1994; Zhu et al., 2007).

Conservation of angular momentum provides the closing relation by specifying the accreting column needed to drive the inflow caused by turbulence, $\dot{M} = 2\pi\nu\Sigma$ (Shakura & Sunyaev, 1973; see footnote[3]). A common approach to modelling the turbulent viscosity ν is to adopt the α-viscosity prescription, in which uncertainties in the form of the viscosity are gathered into a single parameter $\alpha \lesssim 1$ (Shakura & Sunyaev, 1973),

$$\nu = \alpha c_s H. \tag{2.14}$$

Observational estimates of α, derived from the inferred mass accretion rates of T-Tauri stars, and the time dependent behaviour of FU Orionis outbursts, dwarf nova, and X-ray transients, indicate $\alpha \sim 0.001 - 0.1$, while numerical magnetohydrodynamical shearing box simulations yield $\alpha \sim 0.01$–10^{-3} [see King, Pringle & Livio (2007) and references therein]. This results in an accreting column

$$\begin{aligned} \Sigma &= \frac{\dot{M}}{2\pi\alpha c_s H} \qquad (2.15) \\ &\approx 1.6 \times 10^2 \mathrm{g\ cm}^{-2} \left(\frac{\dot{M}}{10^{-6} M_J/\mathrm{yr}}\right) \left(\frac{\alpha}{10^{-3}}\right)^{-1} \left(\frac{M}{M_J}\right)^{\frac{1}{2}} \left(\frac{T}{10^3\,\mathrm{K}}\right)^{-1} \left(\frac{r}{10^2\,R_J}\right)^{-\frac{3}{2}} \end{aligned}$$

for negligible self-gravity.

2.3 Degree of ionisation

In this section we calculate the level of ionisation at the midplane of the circumplanetary disc. The disc is too dense for the penetration of cosmic rays and X-rays down to the midplane, and so the primary sources of ionisation are thermal ionisation and decaying radionuclides. We also consider two further ionising mechanisms produced by the action of MRI turbulence - the transport of ionisation from MRI active surface layers to the midplane by eddies, and ionisation by electric fields generated by MRI turbulence.

[3]Heat is released in a boundary layer (thickness $\ll R_J$) above the planet surface where the disc angular velocity profile transitions sharply between Keplerian and the planetary rotation rate (Pringle, 1977). This contributes an additional factor $\left(1 - \sqrt{R_J/r}\right)$ to the right hand side to this viscosity-inflow relation. However, we find that this factor is only significant within $r < 2\,R_J$, i.e., within the boundary layer.

Table 2.2: Atomic number (Z), atomic weight, solar photospheric logarithmic abundance and abundance, and first ionisation potential for hydrogen, helium, sodium, magnesium, and potassium (Lide, 2004; Asplund et al., 2009). Depletion of heavy elements by incorporation into grains is parametrised by δ.

Z	Element	Atomic weight (amu)	Logarithmic Abundance	Abundance	Ionisation potential (eV)	Depletion (dex)
1	H	1.01	12.00	9.21×10^{-1}	13.60	0
2	He	4.00	10.93	7.84×10^{-2}	24.59	0
11	Na	22.98	6.24	1.60×10^{-6}	5.14	δ
12	Mg	24.31	7.60	3.67×10^{-5}	7.65	δ
19	K	39.10	5.03	9.87×10^{-8}	4.34	δ

2.3.1 Thermal ionisation

Ionisation leads to the production of electrons, ions (with atomic number j), and charged dust grains with associated number density n_e, $n_{i,j}$, n_g, mass m_e, $m_{i,j}$, m_g, and charge $-q$, $+q$, $Z_g q$ respectively. Here, grain mass and charge represent the mean value.

From this we define the total ion number density $n_i \equiv \sum_j n_{i,j}$, and average ion mass $m_i \equiv \left(n_i^{-1} \sum_j n_{i,j} m_{i,j}{}^{-\frac{1}{2}}\right)^{-2}$, where the summation runs over each ion species.

To calculate the level of thermal ionisation we use the Saha equation

$$\frac{n_e n_{i,j}}{n_j} = g_e \left(\frac{2\pi m_e kT}{h^3}\right)^{\frac{3}{2}} \exp\left(-\frac{\chi_j}{kT}\right), \tag{2.16}$$

where n_j is the number density of neutrals with atomic number j, χ_j is the ionisation potential of the j^{th} ion species, $g_e = 2$ is the statistical weight of an electron, and h is Planck's constant. Table 2.2 gives the atomic weight and first ionisation energy of five key contributing elements: hydrogen, helium, sodium, magnesium, and potassium (Lide, 2004).

The exponential factor in the Saha equation gives rise to switch on/off behaviour in thermal ionisation, such that the bulk of atoms are ionised in a narrow temperature band around their ionisation temperature. Potassium has the lowest ionisation energy, and is first to be ionised, with an ionisation temperature of $T \sim 10^3$ K.

We use solar photospheric abundances to model the elemental composition of the disc, as given in Table 2.2 (Asplund et al., 2009). However, heavy elements are incorporated into grains, reducing their gas phase abundance. We allow for depletion into grains through a depletion factor δ (c.f., Sano et al., 2000). The degree of depletion varies greatly between elements, however we make the simplification that the abundance of elements other than hydrogen and helium are reduced by a constant factor, 10^{δ}. Grain depletion in the Orion nebula has been determined by comparing the abundances in the HII region (gas only) with that of Orion O stars (gas and dust; Esteban et al., 1998). Magnesium, a key grain constituent, is depleted at the level $\delta_{\mathrm{Mg}} = -0.92$, which we adopt for all depleted elements.

The abundance of the j^{th} element is related to its logarithmic form, accounting for depletion into grains: $X_j = \log_{10}(n_j/n_H) + 12 - \delta$, where the logarithmic abundance of hydrogen is defined to be $X_H = 12$. The abundance is then $x_j = 10^{X_j}/(\sum_i 10^{X_i})$, for which we take the logarithmic abundances of the remaining elements from Asplund et al. (2009).

Dust grains also act to reduce the ionisation fraction by soaking up electrons, acquiring charge through the competitive sticking of electrons and ions to their surface. The net charge is found through the balance of preferential sticking of electrons due to their higher thermal velocity, with the subsequent Coulomb repulsion that develops. The average charge acquired by a dust grain is (Draine & Sutin, 1987)

$$Z_g = \psi\tau - \frac{1}{1 + \sqrt{\tau_0/\tau}} \tag{2.17}$$

where

$$\tau = \frac{a_g k T}{q^2}, \tag{2.18}$$

$$\tau_0 \equiv \frac{8 m_e}{\pi \mu m_p}, \tag{2.19}$$

$$\mu \equiv \left(\frac{n_e s_e}{n_i}\right)^2 \left(\frac{m_i}{m_p}\right), \tag{2.20}$$

where s_e is the electron sticking coefficient, a_g the grain radius, and ψ is the solution to the transcendental equation (Spitzer, 1941):

$$1 - \psi = \left(\mu \frac{m_p}{m_e}\right)^{\frac{1}{2}} e^{\psi}. \tag{2.21}$$

We solve this using the second-order approximation (Armstrong & Kulesza, 1981)

$$\psi = 1 - \ln(1+y) + \frac{\ln(1+y)}{1 + \ln(1+y)} \ln[(1 + y^{-1}) \ln(1+y)] \tag{2.22}$$

with $y \equiv e\sqrt{\mu m_p/m_e}$.

Charge fluctuations are small, with most grains having charge within one unit about this mean (Elmegreen, 1979). Measurements and analytical estimates of the electron sticking coefficient suggest s_e is in the range 10^{-3}–1 (Umebayashi & Nakano, 1980; Heinisch, Bronold & Fehske, 2010). As an approximation, we maximise the impact of grain charge removal by adopting $s_e \sim 1$.

We adopt a constant gas-to-dust mass ratio ratio $\rho_d/\rho \equiv f_{dg} = 10^{-2}$, grain size $a_g = 0.1\mu$m, and grain bulk density $\rho_b = 3\,\mathrm{g\ cm^{-3}}$ (Pollack et al., 1994). This leads to a grain number density

$$\begin{aligned} n_g &= \frac{m_n f_{dg} n}{\frac{4}{3}\pi a_g^3 \rho_b} \\ &\approx 3.1\times10^3\,\mathrm{cm^{-3}} \left(\frac{n}{10^{15}\,\mathrm{cm^{-3}}}\right)\left(\frac{f_{dg}}{10^{-2}}\right)\left(\frac{a_g}{0.1\,\mu\mathrm{m}}\right)^{-3}\left(\frac{\rho_b}{3\,\mathrm{g\ cm^{-3}}}\right)^{-1}. \end{aligned} \tag{2.23}$$

Grain evaporation, which removes grain species, will cause spatial variation of these properties. For instance, very few grains would be present where the temperature exceeds the vaporisation temperature of iron ($T \sim 1500\,\mathrm{K}$ at $\rho \sim 10^{-7}\,\mathrm{g\,cm^{-3}}$; Pollack et al., 1994). However, we find that removing grains in this region (i.e., $f_{dg} = 0$ for $r < 7\,R_J$), or indeed uniformly across the disc (i.e., $f_{dg} = 0$ for all r), has no effect on the boundary of the magnetically-coupled region owing to the overwhelming effectiveness of thermal ionisation here.

The final condition needed to determine the ionisation level is charge neutrality,

$$n_i - n_e + Z_g n_g = 0. \tag{2.24}$$

To solve equations (2.16)–(2.24), we use Powell's Hybrid Method for root finding (Powell, 1970), with the routine `fsolve` from the Python library `scipy.optimize` (Jones et al., 2001). This method is a modified form of Newton's Method, which checks that the residual is improved before accepting a Newton step. This optimisation allows for convergence despite the steep gradients caused by the exponential factor in the Saha equation.

2.3.2 Ionisation by decaying radionuclides, cosmic rays and X-rays

Cosmic rays and the decay of radionuclides are the primary sources of ionisation in the outer disc where it is too cool for thermal ionisation. The short-lived radioisotope ^{26}Al is the main contributor to ionisation by decaying radionuclides, yielding an ionisation rate $\zeta_R = 7.6 \times 10^{-19}\,\mathrm{s}^{-1}$ (Umebayashi & Nakano, 2009).

Cosmic ray ionisation occurs at a rate $\zeta_{\mathrm{CR}} = 10^{-17}\,\mathrm{s}^{-1}\exp(-\Sigma/\Sigma_{\mathrm{CR}})$, where $\Sigma_{\mathrm{CR}} = 96\,\mathrm{g\,cm^{-2}}$ is the attenuation depth of cosmic rays. However, cosmic-ray ionisation is negligible in our disc as we find the disc column density is too large for penetration of the ionising radiation.

X-rays from the young star will also ionise the surface layers [with $\zeta_{\mathrm{XR}} = 9.6 \times 10^{-17}\,\mathrm{s}^{-1}\exp(-\Sigma/\Sigma_{\mathrm{XR}})$ at the orbital radius of Jupiter for a star with Solar luminosity (Igea & Glassgold, 1999; Turner & Sano, 2008)], however the X-ray attenuation depth is so small ($\Sigma_{\mathrm{XR}} = 8\,\mathrm{g\,cm^{-2}}$) that X-rays do not reach the midplane and do not contribute to midplane ionisation or accretion [in contrast with *surface* ionisation calculations by Turner, Lee & Sano (2014)].

Calculating the ionisation resulting from radioactive decay involves solving a coupled set of reaction rate equations for electrons, metal ions (number density n_i with metal abundance x_m), and grains subject to charge neutrality. Molecular ions are the first ions produced as part of the reaction scheme, but charge transfer to metals is so rapid that metal ions are more abundant (Fujii, Okuzumi & Inutsuka, 2011). We model the metals as a single species, adopting the mass, m_i, and abundance, x_i, of the most abundant metal - magnesium (Lide, 2004; Asplund et al., 2009). Free electrons and ions are formed through ionisation, and are removed through recombination (rate coefficient k_{ei}) and capture by grains (rate coefficients k_{eg}, k_{ig} for electrons and ions, respectively).

These processes are described by the following rate equations:

$$\frac{dn_i}{dt} = \zeta n - k_{ei} n_i n_e - k_{ig} n_g n_i, \tag{2.25}$$

$$\frac{dn_e}{dt} = \zeta n - k_{ei} n_i n_e - k_{eg} n_g n_e, \tag{2.26}$$

$$\frac{dZ_g}{dt} = k_{ig} n_i - k_{eg} n_e, \tag{2.27}$$

$$0 = n_i - n_e + Z_g n_g, \tag{2.28}$$

for which we have neglected grain charge fluctuations (see for example, Umebayashi & Nakano 1980; Fujii, Okuzumi & Inutsuka 2011). Anticipating that the resulting ionisation fraction will be low, we make the following simplifications: (i) the average grain charge will be low and so we approximate $Z_g \approx 0$ in calculating the rate coefficients k_{ig}, k_{eg}, and (ii) recombination is inefficient such that charge capture by grains dominates and we set $k_{ei} = 0$. The charge capture rate co-efficients for neutral grains are

$$\begin{aligned} k_{ig} &= \pi a_g^2 \sqrt{\frac{8k_bT}{\pi m_i}} \\ &\approx 3.0\times 10^{-5}\,\mathrm{cm^3\,s^{-1}} \left(\frac{T}{10^3\,\mathrm{K}}\right)^{\frac{1}{2}} \left(\frac{a_g}{0.1\mu\,\mathrm{m}}\right)^{2} \left(\frac{m_i}{24.3\,m_p}\right)^{-\frac{1}{2}}, \end{aligned} \tag{2.29}$$

$$\begin{aligned} k_{eg} &= \pi a_g^2 \sqrt{\frac{8k_bT}{\pi m_e}} \\ &\approx 6.2\times 10^{-3}\,\mathrm{cm^3\,s^{-1}} \left(\frac{T}{10^3\,\mathrm{K}}\right)^{\frac{1}{2}} \left(\frac{a_g}{0.1\mu\,\mathrm{m}}\right)^{2}. \end{aligned} \tag{2.30}$$

Under these conditions the equilibrium electron and ion number density fractions are

$$\begin{aligned} \frac{n_e}{n} &= \frac{\zeta}{k_{eg}n_g}, \\ &\approx 5.2\times 10^{-20} \left(\frac{T}{10^3\,\mathrm{K}}\right)^{-\frac{1}{2}} \left(\frac{n}{10^{15}\,\mathrm{cm^{-3}}}\right)^{-1} \left(\frac{\zeta}{10^{-18}\,\mathrm{s^{-1}}}\right) \\ &\times \left(\frac{\rho_b}{3\,\mathrm{g\,cm^{-3}}}\right) \left(\frac{f_{dg}}{10^{-2}}\right)^{-1} \left(\frac{a_g}{0.1\mu\,\mathrm{m}}\right), \end{aligned} \tag{2.31}$$

and

$$\begin{aligned} \frac{n_i}{n} &= \frac{k_{eg}}{k_{ig}}\frac{n_e}{n_n}, \\ &\approx 1.1\times 10^{-17} \left(\frac{T}{10^3\,\mathrm{K}}\right)^{-\frac{1}{2}} \left(\frac{n}{10^{15}\,\mathrm{cm^{-3}}}\right)^{-1} \left(\frac{\zeta}{10^{-18}\,\mathrm{s^{-1}}}\right) \\ &\times \left(\frac{\rho_b}{3\,\mathrm{g\,cm^{-3}}}\right) \left(\frac{f_{dg}}{10^{-2}}\right)^{-1} \left(\frac{a_g}{0.1\mu\,\mathrm{m}}\right) \left(\frac{m_i}{24.3\,m_p}\right)^{\frac{1}{2}}. \end{aligned} \tag{2.32}$$

We insert these values into equation (2.28) to calculate an improved estimate of the grain charge:

$$\begin{aligned} Z_g &= -\frac{n_i}{n_g} \\ &\approx -3.5\times 10^{-6} \left(\frac{T}{10^3\,\mathrm{K}}\right)^{-\frac{1}{2}} \left(\frac{n}{10^{15}\,\mathrm{cm^{-3}}}\right)^{-1} \left(\frac{\zeta}{10^{-18}\,\mathrm{s^{-1}}}\right) \\ &\times \left(\frac{\rho_b}{3\,\mathrm{g\,cm^{-3}}}\right)^{2} \left(\frac{f_{dg}}{10^{-2}}\right)^{-2} \left(\frac{a_g}{0.1\mu\,\mathrm{m}}\right)^{4} \left(\frac{m_i}{24.3\,m_p}\right)^{\frac{1}{2}}. \end{aligned} \tag{2.33}$$

Charge capture by grains has removed a large fraction of the free electrons and so the average grain charge is small (validating our initial estimate, $Z_g \approx 0$), and simply traces the ion density. To calculate the charge resulting from the combined efforts of thermal ionisation, decay of radionuclides, and external ionisation sources we add the contributions linearly. A complete treatment would address the non-linear effects associated with using the combined charge particle population, rather than treating the populations as independent. However, as the drop-off of the radial thermal ionisation profile is so steep, the contribution of decaying radionuclides and cosmic rays within $r \lesssim 55\,R_J$ is insignificant when compared to thermal ionisation. Similarly, thermal ionisation is highly inefficient beyond this distance, and so charge production is by radioactive decay and cosmic rays.

2.3.3 Ionisation from MRI turbulence

The action of MRI turbulence in the disc offers two further ionising mechanisms, which we describe below. We do not calculate the level of ionisation produced by these mechanisms, but rather determine their effectiveness within the circumplanetary disc.

Eddies in ionised, MRI active, surface layers may penetrate into the underlying dead zone, transporting ionised material with them (Ilgner & Nelson, 2006; Turner, Sano & Dziourkevitch, 2007; Ilgner & Nelson, 2008). Turbulent mixing may deliver enough ionisation into the dead zone for magnetic coupling and reactivation of the dead zone (Turner, Sano & Dziourkevitch, 2007). The vertical mixing time-scale for diffusion through a scale height is (Ilgner & Nelson, 2006)

$$\tau_D = \frac{H^2}{\nu} = (\alpha\Omega)^{-1}, \tag{2.34}$$

which is 1000 dynamical time-scales for a Shakura-Sunyaev viscosity parameter $\alpha = 10^{-3}$. However, free charges are removed through recombination and grain charge capture which lowers the ionisation fraction. From equation (2.26), we find that charges are removed on a time-scale

$$\tau_R = \left(k_{ei}\overline{n_i} + k_{eg}\overline{n_g}\right)^{-1}, \tag{2.35}$$

where the ion and grain number densities are vertically averaged along the path. We calculate the grain charge capture rate k_{eg} for neutral grains, and the ion number density using the height-averaged cosmic ray and constant radioactive decay ionisation rates assuming that ion capture by grains is small. We use a vertically uniform temperature, but we find no qualitative difference in the results using midplane or surface temperatures. For turbulent mixing to be effective in delivering ionisation to the midplane, it must be at least as rapid as charge removal (i.e., $\tau_D \gtrsim \tau_R$). Thus, we determine the effectiveness of midplane ionisation from active surface layers by comparing the charge removal and vertical mixing time-scales in §2.7.

Ionisation is also produced through currents generated by the action of the MRI turbulent field (Inutsuka & Sano, 2005). An electric field, E, associated with the MRI may be able to accelerate electrons to high enough energies that they ionise hydrogen in some regions. Such MRI 'sustained' regions occur within the minimum mass solar nebula, reducing the vertical extent of the dead zone away from the midplane (Muranushi, Okuzumi & Inutsuka, 2012). Here we determine if self-sustained MRI occurs in circumplanetary discs.

Joule heating is the primary mechanism for converting work done by shear [work per unit volume $W_{\rm S} = (3/2)\alpha\Omega p$] into electron kinetic energy. The work dissipated per unit volume by Joule heating of an equipartition current [i.e., the current $J_{\rm eq} = cB_{\rm eq}/(4\pi H)$ associated with an equipartition field over a length scale H], is $W_J = f_{\rm fill} f_{\rm sat} J_{\rm eq} E$. Here c is the speed of light, $f_{\rm fill}$ is the filling factor representing the fraction of the total volume contributing to Joule heating, and $f_{\rm sat}$ is the ratio of the saturation current in MRI unstable regions to the equipartition current. Muranushi, Okuzumi & Inutsuka (2012) performed three dimensional shearing box simulations to determine the time, space, and ensemble averaged filling factor and MRI saturation current, finding $f_{\rm fill} = 0.264$ and $f_{\rm sat} = 13.1$. The total energy available for ionisation through Joule heating is limited to the work done by shear (i.e., $W_J \leqslant W_S$), and so the electric field strength cannot exceed (Muranushi, Okuzumi & Inutsuka, 2012)[4]

$$E = \frac{3\alpha c_s B_{\rm eq}}{4c f_{\rm fill} f_{\rm sat}} \left(\frac{2Q}{1+\sqrt{1+4Q^2}} \right). \tag{2.36}$$

Given this restriction, we calculate the maximum electron kinetic energy, ϵ, available from Joule heating (Inutsuka & Sano, 2005),

$$\epsilon = 0.43 qEl\sqrt{m_n/m_e} \tag{2.37}$$

[4]For consistency we insert our equation (2.38) into equation (32) of Muranushi, Okuzumi & Inutsuka 2012, and account for self-gravity which leads to stricter criterion, independent of plasma β: $f_{\rm whb} = 5.4 \times 10^{-2}$ for $Q = 0$ [c.f., their equation (36)].

where $l = 1/(n\langle\sigma_{en}\rangle) \approx 1\,\mathrm{cm}\,(10^{15}\,\mathrm{cm}^{-3}/n)$ is the electron mean free path, and $\langle\sigma_{en}\rangle = 10^{-15}\,\mathrm{cm}^2$ is the momentum transfer rate co-efficient between electrons and neutrals. For ionisation to be effective, the electron energy, ϵ must exceed the ionisation threshold of neutral particles within the disc.

2.4 Magnetic field strength

Further to a possible proto-planetary dynamo field (e.g., Jupiter's present day surface field is 4.2 G; Stevenson, 2003), the disc may accrete its own field from the protoplanetary disc (Quillen & Trilling, 1998; Turner, Lee & Sano, 2014). As both MRI and vertical fields have been modelled extensively in protoplanetary discs, we consider both field geometries in driving accretion in circumplanetary discs. We calculate the magnetic field strength, B, required to drive accretion at the inferred accretion rate, $\dot{M} = 10^{-6} M_J/\mathrm{year}$.

Three-dimensional stratified and unstratified shearing box, and global MRI simulations with a net vertical flux indicate that during accretion the MRI magnetic field saturates with (Hawley, Gammie & Balbus, 1995; Sano et al., 2004; Simon, Hawley & Beckwith, 2011; Parkin & Bicknell, 2013)

$$\alpha \approx 0.5\beta^{-1} = 0.5\frac{B^2}{8\pi p}, \tag{2.38}$$

where $\beta \equiv 8\pi p/B^2$ is the plasma beta, and $p = c_s^2\rho$ is the pressure. This leads to a turbulent magnetic field strength

$$B_{\mathrm{MRI}} = \sqrt{16\pi\alpha c_s^2\rho}, \tag{2.39}$$

which can be directly determined by the inflow rate as (Wardle, 2007)

$$\begin{aligned} B_{\mathrm{MRI}} &= \left(\frac{\dot{M}\Omega^2}{c_s}\right)^{\frac{1}{2}}\left(\frac{1+\sqrt{1+4Q^2}}{Q}\right) \qquad (2.40)\\ &\approx 0.66\,\mathrm{G}\left(\frac{\dot{M}}{10^{-6}M_J/\mathrm{year}}\right)^{\frac{1}{2}}\left(\frac{M}{M_J}\right)^{1/2}\left(\frac{T}{10^3\,\mathrm{K}}\right)^{-\frac{1}{4}}\\ &\quad\times\left(\frac{r}{10^2\,R_J}\right)^{-\frac{3}{2}}\left(\frac{Q^{-1}+\sqrt{Q^{-2}+4}}{2}\right). \end{aligned}$$

The equipartition field, $B_{\mathrm{eq}} = \sqrt{8\pi p}$, defines the maximum field that the disc can support before magnetic pressure dominates over thermal pressure. From equation (2.38) we see that the MRI field is sub-equipartition, satisfying

$$\frac{B_{\rm MRI}}{B_{\rm eq}} = \frac{v_a}{\sqrt{2}c_s} = \sqrt{2\alpha} \tag{2.41}$$

where the Alfvén speed is

$$\begin{aligned} v_a &= \frac{B}{\sqrt{4\pi\rho}}, \\ &\approx 8.9\times10^{-2}\,{\rm km\,s^{-1}}\left(\frac{B}{1\,{\rm G}}\right)\left(\frac{\rho}{10^{-9}{\rm g\,cm^{-3}}}\right)^{-\frac{1}{2}}. \end{aligned} \tag{2.42}$$

This ratio is constant for a given α.

Large-scale fields acting through disc winds and jets may also drive angular momentum transport and have been studied in the context of protoplanetary discs (e.g., Wardle & Königl 1993; Shu et al. 1994; Bai & Stone 2013). Magnetically-driven outflows have also been proposed for circumplanetary discs (Quillen & Trilling, 1998; Fendt, 2003; Machida, Inutsuka & Matsumoto, 2006; Adams, 2011). If a vertical field drives the inflow the field strength must be at least (Wardle, 2007)

$$\begin{aligned} B_{\rm V} &= \sqrt{\frac{\dot{M}\Omega}{2r}}, \\ &\approx 0.16\,{\rm G}\left(\frac{\dot{M}}{10^{-6}M_J/{\rm year}}\right)^{\frac{1}{2}}\left(\frac{M}{M_J}\right)^{\frac{1}{4}}\left(\frac{r}{10^2\,R_J}\right)^{-5/4}. \end{aligned} \tag{2.43}$$

2.5 Magnetic coupling

We are now in a position to calculate the level of magnetic diffusivity within the disc to identify which regions of the disc are subject to magnetically-driven transport. A minimum level of interaction between the disc and the magnetic field is needed for magnetically-controlled accretion.

Collisions disrupt the gyromotion of charged species around the magnetic field. Collisions between the electrons, ions, and neutrals occur at a rate ν_{ij} (for colliding species i with j), with (Spitzer, 1962; Draine, 1980; Draine, Roberge & Dalgarno, 1983; Pandey & Wardle, 2008)

$$\nu_{\rm ei} = 1.6\times10^{-2}\,{\rm s^{-1}}\left(\frac{T}{10^3\,{\rm K}}\right)^{-\frac{3}{2}}\left(\frac{n_e}{10\,{\rm cm^{-3}}}\right)\left(\frac{n_n}{10^{15}\,{\rm cm^{-3}}}\right), \tag{2.44}$$

$$\nu_{\rm en} = 6.7\times10^{6}\,{\rm s}^{-1}\left(\frac{T}{10^{3}\,{\rm K}}\right)^{-\frac{1}{2}}\left(\frac{\rho_n}{10^{-9}\,{\rm g\,cm^{-3}}}\right), \tag{2.45}$$

$$\nu_{\rm in} = 3.4\times10^{5}\,{\rm s}^{-1}\left(\frac{\rho_n}{10^{-9}\,{\rm g\,cm^{-3}}}\right), \tag{2.46}$$

where $\rho_n = \rho-(\rho_i+\rho_e)$, and $n_n = \rho_n/m_n$ are the mass and number density of neutral particles, respectively. Electron–ions collisions are the dominant source of drag in the highly ionised inner region, but neutral drag dominates across the remainder of the disc.

These collision frequencies are consistent with state of the art measured collision cross-sections (Pinto & Galli, 2008). We use the Langevin estimate for the ion-neutral collision cross-section, which is within a factor of two of the Pinto & Galli (2008) H_2–HCO^+ and H_2–H_3^+ fits. Our electron-neutral collision cross-sections are also within a factor of two of the best e^-–H_2 fits, and up to an order of magnitude better than the Langevin estimate.

The Hall parameter for a species j, β_j, quantifies the relative strength of magnetic forces and neutral drag. It is the ratio of the gyrofrequency to the neutral collision frequency (Wardle, 2007),

$$\beta_j = \frac{|Z_j|eB}{m_j c}\frac{1}{\nu_{jn}}. \tag{2.47}$$

The Hall parameter is large, $\beta_j \gg 1$, when magnetic forces dominate the equation of motion, and small, $\beta_j \ll 1$, when neutral drag decouples the motion from the field.

The Hall parameters for ions, electrons, and grains are (Wardle, 1998, 2007)

$$\beta_i \approx 4.6\times10^{-3}\left(\frac{B}{1\,G}\right)\left(\frac{n}{10^{15}\,{\rm cm^{-3}}}\right)^{-1}, \tag{2.48}$$

$$\beta_e \approx 1.1\left(\frac{B}{1\,G}\right)\left(\frac{n}{10^{15}\,{\rm cm^{-3}}}\right)^{-1}\left(\frac{T}{10^{3}\,K}\right)^{-\frac{1}{2}}, \tag{2.49}$$

$$\beta_g \approx 5.5\times10^{-8}Z_g\left(\frac{B}{1\,{\rm G}}\right)\left(\frac{n}{10^{15}\,{\rm cm^{-3}}}\right)^{-1}\left(\frac{T}{1000\,{\rm K}}\right)^{-\frac{1}{2}} \times\left(\frac{a_g}{0.1\,\mu{\rm m}}\right)^{\frac{1}{2}}\left(\frac{\rho_b}{3\,{\rm g\,cm^{-3}}}\right)^{\frac{1}{2}}. \tag{2.50}$$

Ions and grains, being the more massive particles, have a lower gyrofrequency, and hence a lower Hall parameter[5]. Thus, neutral collision are more effective at decoupling ions and grains than electrons. This leads to three regimes, according to the neutral density: (a) Ohmic regime, high density: electron–ion or neutral collisions are so frequent as to decouple both electrons and ions (i.e., $\beta_i \ll \beta_e \ll 1$). (b) Hall regime, intermediate density: neutral collisions decouple ions, but the electrons remain tied to the field (i.e., $\beta_i \ll 1 \ll \beta_e$). (c) Ambipolar regime, low density: both the ions and electrons are coupled to the magnetic field, and drift through the neutrals. (i.e., $1 \ll \beta_i \ll \beta_e$).

In each regime collisions produce magnetic diffusivity which affects the evolution of the magnetic field through the induction equation:

$$\frac{\partial \mathbf{B}}{\partial t} = \nabla(\mathbf{v} \times \mathbf{B}) - \nabla \times [\eta_O(\nabla \times \mathbf{B}) + \eta_H(\nabla \times \mathbf{B}) \times \hat{\mathbf{B}}] - \nabla \times [\eta_A(\nabla \times \mathbf{B})_\perp], \quad (2.51)$$

where $\mathbf{v}$ is the fluid velocity, and the subscript $\perp$ refers to the orientation with respect to the local magnetic field.

Ohmic (η_O), Hall (η_H), and Ambipolar transport coefficients (η_A) are [Pandey & Wardle, 2008, Wardle & Pandey (in preparation)]

$$\begin{aligned} \eta_O &= \frac{m_e c^2}{4\pi e^2 n_e}(\nu_{\rm en} + \nu_{\rm ei}) \\ &\approx 1.9 \times 10^{17} \mathrm{cm^2\,s^{-1}} \left[\left(\frac{T}{10^3\,\mathrm{K}}\right)^{\frac{1}{2}} \left(\frac{n_e}{10\,\mathrm{cm^{-3}}}\right)^{-1} \left(\frac{\rho}{10^{-9}\,\mathrm{g\,cm^{-3}}}\right) \right. \\ &\quad \left. \times + 2.4 \times 10^{-9} \left(\frac{T}{10^3\,\mathrm{K}}\right)^{-\frac{3}{2}} \right], \end{aligned} \quad (2.52)$$

$$\begin{aligned} \eta_H &= \frac{cB}{4\pi e n_e}\left(\frac{1+\beta_g^2 - \beta_i^2 P}{1+(\beta_g+\beta_i P)^2}\right) \\ &\approx 5.0 \times 10^{17}\,\mathrm{cm^2\,s^{-1}} \left(\frac{B}{1\,\mathrm{G}}\right) \left(\frac{n_e}{10\,\mathrm{cm^{-3}}}\right)^{-1} \left(\frac{1+\beta_g^2 - \beta_i^2 P}{1+(\beta_g+\beta_i P)^2}\right), \end{aligned} \quad (2.53)$$

[5]The grain Hall Parameter in equation (51) of Keith & Wardle (2014) is a factor of $\sqrt{m_g/m_n}$ too large, and is corrected in equation (2.50). This discrepancy does not affect the results of Keith & Wardle (2014) as the terms involving β_g in the diffusivities are negligible in the diffusivities, equation (2.52)–(2.54).

$$
\begin{aligned}
\eta_A &= \left(\frac{B^2}{4\pi\rho_i\nu_{\rm ni}}\right)\left(\frac{\rho_n}{\rho}\right)^2\left(\frac{1+\beta_g^2+(1+\beta_i\beta_g)\,P}{1+(\beta_g+\beta_i P)^2}\right) \\
&\approx 6.0\times10^{16}\,{\rm cm^2\,s^{-1}}\left(\frac{B}{1\,{\rm G}}\right)^2\left(\frac{\rho_n}{\rho}\right)^2\left(\frac{n_i}{10\,{\rm cm^{-3}}}\right)^{-1} \\
&\quad\times\left(\frac{\rho}{10^{-9}\,{\rm g\,cm^{-3}}}\right)^{-1}\left(\frac{1+\beta_g^2+(1+\beta_i\beta_g)\,P}{1+(\beta_g+\beta_i P)^2}\right),
\end{aligned}
\tag{2.54}
$$

where $P = n_g|Z_g|/n_e$ is the Havnes parameter[6].

The magnetic field couples to the motion of the disc in regions of low magnetic diffusivity [i.e., where $|\nabla\times(\mathbf{v}\times\mathbf{B})| \gg |\nabla\times[\eta(\nabla\times\mathbf{B})]|$, for each diffusivity, η]. For MRI fields we require that the turbulent magnetic field grows faster than dissipation can destroy it such that (Sano & Stone, 2002; Mohanty, Ercolano & Turner, 2013)

$$
\begin{aligned}
\eta &< v_{a,z}^2/\Omega \\
&\approx 1.3\times10^{14}\,{\rm cm^2\,s^{-1}}\left(\frac{B}{1\,{\rm G}}\right)^2\left(\frac{\rho}{10^{-9}\,{\rm g\,cm^{-3}}}\right)^{-1} \\
&\quad\times\left(\frac{r}{10^2\,R_J}\right)^{\frac{3}{2}}\left(\frac{M}{M_J}\right)^{-\frac{1}{2}}
\end{aligned}
\tag{2.55}
$$

for each transport coefficient $\eta = \eta_O$, η_H, and η_A. This condition is equivalent to the condition $\Lambda > 1$, where $\Lambda = v_{a,z}^2/(\eta\Omega)$ is the Elsasser number. The coupling condition uses the Alfvén speed for the vertical component of the magnetic field. We calculate the vertical field component as $B_z \sim B_{\rm MRI}/\sqrt{28}$, using results from Sano et al. (2004).

If, instead, a vertical (rather than turbulent) field is responsible for angular momentum transport (e.g., through the action of a disc wind or jet), the condition is more relaxed as we only require that the magnetic field couples to the shear, with (Wardle, 2007)

$$
\begin{aligned}
\eta &< c_s^2/\Omega \\
&\approx 6.1\times10^{16}\,{\rm cm^2\,s^{-1}}\left(\frac{T}{10^3\,{\rm K}}\right)\left(\frac{r}{10^2\,R_J}\right)^{\frac{3}{2}}\left(\frac{M}{M_J}\right)^{-\frac{1}{2}}
\end{aligned}
\tag{2.56}
$$

for each non-ideal effect.

Magnetic interaction still occurs for non-ideal effects at, or above the coupling

[6]There is a typographical error in the expression Ohmic resistivity in equation (53) of Keith & Wardle (2014). The scaling of the diffusivity with the neutral density should be $\eta_O \propto \rho$ rather than the inverse proportionality given.

threshold, but weak coupling in these conditions diminishes the connection between the dynamics of the disc and field.

2.6 Disc models

We consider four circumplanetary disc models in this study. We present two Shakura-Sunyaev α discs developed for this work: (i) a constant-α model in which the viscosity parameter is radially-uniform (§2.6.1), and (ii) a self-consistent accretion model in which the level of angular momentum transport is consistent with the strength of magnetic coupling or gravitational instability at all radii (§2.6.2). For comparison we also describe two key circumplanetary disc models in the literature: (iii) the Minimum Mass Jovian Nebula (§2.6.3), and (iv) the Canup & Ward α disc (§2.6.4).

2.6.1 Constant-α model

Here we take the traditional approach, adopting the α-viscosity prescription with a radially-uniform α. This allows for direct comparison with existing steady state circumplanetary disc models which adopt a constant α. We take $\alpha = 10^{-3}$ in keeping with the results of simulations (with net zero magnetic flux). However, the disc may accrete a net field which enhances transport, and so we also consider $\alpha = 10^{-2}$.

To obtain the radial temperature profile for this model we insert equations (2.6) and (2.15) into equation (2.13), yielding (Bell et al., 1997)

$$T^{\frac{3}{2}a-b+5} = \frac{9\kappa_i}{2^{2a+8}\sigma}\left(\frac{\mu m_p}{k}\right)^{\frac{3}{2}a+1}\alpha^{-(a+1)}\left(\frac{\dot{M}}{\pi}\right)^{a+2}\left(\frac{GM}{r^3}\right)^{a+\frac{3}{2}}. \tag{2.57}$$

We calculate all other properties, such as column density, by inserting this temperature profile into the relations given in §2.2.

2.6.2 Self-consistent accretion model

The constant-α model implicitly assumes that the angular momentum transport mechanism operates at all radii, and to the right degree. Ionisation by cosmic rays and decaying radionuclides is insufficient to couple the disc and magnetic field (Fujii, Okuzumi & Inutsuka, 2011), and thermal ionisation is only active in the inner disc where $T \gtrsim 10^3$ K. Without gravitoturbulence from gravitational instability, or magnetically driven transport, which relies on magnetic coupling, little if any viscosity is produced throughout the bulk of the disc (i.e., $\alpha \approx 0$). Thus, equation (2.15) is invalid across the majority of the disc.

Motivated by the inconsistency of the constant-α disc, we present an enhanced steady-state α disc in which the level of angular momentum transport (i.e., α) driven by magnetic fields or gravitoturbulence is consistent with the level of magnetic coupling and strength of gravitational instability at all radii.

To achieve this we divide the disc into three regions according to the mode of transport:

1. Saturated magnetic transport - the inner disc is hot enough for significant thermal ionisation allowing for strong magnetic coupling (i.e., η_O, η_H, η_A are well below than the coupling threshold) and Toomre's $Q \gg 1$. Magnetically-driven angular momentum transport is maximally efficient and α saturates at its maximum value, which we take as $\alpha_{\rm sat} = 10^{-3}$. In this region the disc is identical to the constant-α disc.

2. Marginally coupled magnetic transport - in the majority of the disc, magnetic diffusivity exceeds the coupling threshold while self-gravity is still too weak for gravitoturbulence (i.e., Toomre's $Q > 1$). In this intermediate region accretion is magnetically-driven, although at a reduced efficiency. Sano & Stone (2002) determined the saturation level for MRI turbulence, and hence α, for Ohmic and Ohmic+Hall MHD simulations in the non-linear regime (i.e., $\eta\Omega/v_{a,z}^2 < 1$; see their Fig. 20). They find that α is proportional to the ratio of the coupling threshold, $v_{a,z}^2/\Omega$, to Ohmic diffusivity. By extension we also assume that the effective α for non-turbulent accretion (i.e., for a vertical field) also adjusts according to the level of resistivity, using the analogous coupling threshold, c_s^2/Ω. Thus, in this regime for the two modes of magnetic transport, we take α to be
$$\alpha = \begin{cases} \alpha_{\rm sat} v_{a,z}^2/\left(\eta_O \Omega\right) & \text{for an MRI field,} \\ \alpha_{\rm sat} c_s^2/\left(\eta_O \Omega\right) & \text{for a vertical field,} \end{cases} \tag{2.58}$$
which is at most $\alpha_{\rm sat}$ (Sano & Stone, 2002).

3. Gravoturbulent transport - in the outer disc magnetic coupling at the level required by equation (2.58) would result in a gravitationally unstable disc with Toomre's $Q < 1$, and so self-gravitational forces dominate. The cooling timescale determines whether the disc fragments or enters a gravoturbulent state. We find that the cooling time-scale is much longer than the dynamical

time-scale, Ω^{-1}, (Rafikov, 2007; Boley, 2009) with

$$\begin{aligned}\Omega t_{\rm cool} &= \frac{\Sigma c_s^2 \Omega}{\sigma T_s^4} \\ &= \frac{8 c_s^3}{3 G \dot{M} Q} \\ &\sim 1.9 \times 10^5 \left(\frac{T}{120\,\mathrm{K}}\right)^{\frac{3}{2}} \left(\frac{\dot{M}}{10^{-6}\,M_J/\mathrm{year}}\right)^{-1} Q^{-1}, \end{aligned} \qquad (2.59)$$

[using equations (2.2) and (2.10), for a minimum midplane temperature $T = 120\,\mathrm{K}$ set by the temperature of the Solar Nebula at the present day orbital radius of Jupiter according to the Minimum Mass Solar Nebula (Hayashi, 1981)] and so gravitoturbulence rather than fragmentation occurs (Meru & Bate, 2012). Either by the slow build up of surface density from inflow onto the disc coupled with heating by dissipation of turbulence (Gammie, 2001) or by time dependent evolution of gravitationally-unstable discs (Forgan et al., 2011; Shabram & Boley, 2013), the disc likely evolves towards a state with $Q \sim 1$. Thus, in this region we take $Q = 1$.

We solve for the disc profile by inserting equation (2.5), the scale height with self-gravity, into equation (2.13) requiring one final relation to close the set of equations. Each region has its own closing equation to account for the differences in the mode of transport:

1. In the saturated magnetic-transport region, we use equation (2.15) with constant $\alpha = \alpha_{\rm sat}$, inverted to give the surface density as a function of temperature.

2. In the marginally-coupled magnetic transport region we solve for the midplane temperature numerically using `fsolve` from the Python library `scipy.optimize` (Jones et al., 2001). The solution is determined so that α calculated by inverting equation (2.15) is consistent with that from equation (2.58). To achieve this, at each iteration of the temperature solver we calculate the surface density, scale height and Q through equations (2.2), (2.5) and (2.13) numerically using `fsolve`. These allow us to determine α from equation (2.15), and to also calculate the resulting ionisation fraction, magnetic field, and diffusivity (according to §2.3, §2.4, and §2.5 respectively) for determining α from equation (2.58). Necessarily, α varies radially [i.e., $\alpha \rightarrow \alpha(r)$].

3. In the Gravoturbulent region, we set $Q = 1$ and invert equation (2.2) to give

the surface density as a function of temperature. We post-calculate $\alpha(r)$ using equation (2.15).

We solve the complete set of equations using the routine `fsolve` from the Python library `scipy.optimize` (Jones et al., 2001).

2.6.3 Minimum Mass Jovian Nebula

The Minimum Mass Jovian Nebula (MMJN) is an adaptation of the Minimum Mass Solar Nebula used for modelling the Solar nebula (Weidenschilling, 1977; Hayashi, 1981). The MMJN is produced by smearing out the solid mass of satellites to form a disc, and augmenting it with enough gas to bring the composition up to solar (i.e., $f_{dg} \sim 10^{-2}$).

We use the surface density for the MMJN given in Mosqueira & Estrada (2003) which follows a $\Sigma \propto r^{-1}$ profile, except in a transition region ($20R_J < r < 26R_J$) where the profile steepens,

$$\Sigma = \begin{cases} 5.1 \times 10^5\,\mathrm{g\,cm^{-2}} \left(\dfrac{r}{14\,R_J}\right)^{-1} & r < 20\,R_J, \\ 3.6 \times 10^5\,\mathrm{g\,cm^{-2}} \left(\dfrac{r}{20\,R_J}\right)^{-13.5} & 20\,R_J < r < 26\,R_J, \\ 3.1 \times 10^3\,\mathrm{g\,cm^{-2}} \left(\dfrac{r}{87\,R_J}\right)^{-1} & 26\,R_J < r < 150\,R_J. \end{cases}$$

We use the opacity ($\kappa = 10^{-4}\,\mathrm{cm^2\,g^{-1}}$; appropriate for absorption by hydrogen molecules) and temperature profile given by Lunine & Stevenson (1982),

$$T = \left(240\,\mathrm{K} \left(\frac{r}{15\,R_J}\right)^{-1} + (130\,\mathrm{K})^4\right)^{1/4}. \tag{2.60}$$

The temperature profile follows $T \propto r^{-1}$ in the optically-thick inner regions, and is matched to the temperature of the ambient nebula ($T_{\mathrm{neb}} = 130\,\mathrm{K}$) at the outer edge of the disc.

2.6.4 Canup & Ward α disc

Canup & Ward (2002, 2006) model the circumplanetary disc as a steady-state, thin, axisymmetric, constant–α disc. They adopt the Lynden-Bell & Pringle (1974) surface density model, and use a plane-parallel stellar atmosphere model to calculate the midplane temperature. Heating sources are viscous dissipation, the ambient stellar nebula ($T_{\rm neb} = 150\,{\rm K}$), and the hot young planet. The midplane temperature and density are solved self-consistently for a uniform opacity, but a range of opacities ($\kappa = 10^{-4}$–$1\ {\rm cm}^2\ {\rm g}^{-1}$) are considered to account for uncertainty in the population of sub-micron grains.

A range of inflow rates ($\dot{M} = 10^{-8}$–$10^{-4} M_J/{\rm year}$), and viscosity parameters ($\alpha = 10^{-4}$–10^{-2}), are considered to model the disc at both early and late times. However, a low inflow rate ($\dot{M} = 2 \times 10^{-7} M_J/{\rm year}$) is needed to match the ice line with the present day location of Ganymede and to ensure solid accretion is slow enough to account for Callisto's partially differentiation. This indicates that the disc must be 'gas-starved' as compared with the MMJN.

We calculate this disc model using the method given in Canup & Ward (2002)[7], with parameters taken from Canup & Ward (2006) (i.e., $\alpha = 6.5 \times 10^{-3}$, $\dot{M} = 10^{-6} M_J/{\rm year}$, and $\kappa = 0.1\ {\rm cm}^2\,{\rm g}^{-1}$).

2.7 Results

We are now in a position to apply the tools developed in §2.2–§2.5 to the models described in §2.6. All figures are shown for a protoplanet in orbit around a solar-mass star at the current orbital distance of Jupiter (i.e., $M_* = M_\odot$, and $d = 5.2\,{\rm au}$), calculated with the standard parameter set $\alpha = 10^{-3}$, $\dot{M} = 10^{-6} M_J/{\rm year}$, and $M = M_J$, unless otherwise stated.

2.7.1 Disc structure

Fig. 2.2 shows the radial disc structure for each model. The constant-α disc, MMJN, and Canup & Ward discs are shown as the solid, long-dashed, and dot-dashed curves, respectively. The self-consistent accretion disc is shown for both an MRI (dotted curve) and vertical field (short-dashed curve). The curves are labelled α, MMJN, CW, MRI, and V respectively.

The temperature profiles are shown in the top-left panel. The temperature profile for the constant-α and self-consistent accretion discs follow a power law with index changes at the transitions between opacity regimes. The self-consistent accretion disc profiles follows the constant-α profile out to $\sim 30\,R_J$ where the temperature,

[7]The profiles shown in Fig. 2.2 are calculated using the full expression $\chi = 1 + \frac{3}{2}[r_c/r - \frac{1}{5}]^{-1}$ (given below equation (20) in Canup & Ward 2002), but we found $\chi = 1$ was needed to reproduce the profiles in Canup & Ward (2002). For the parameter set used here, we find that the approximation leads to at most a 37% increase in the surface density, and 27% reduction in the temperature profile. The difference is greatest at $r = 60R_J$, but decreases toward the inner and outer boundaries.

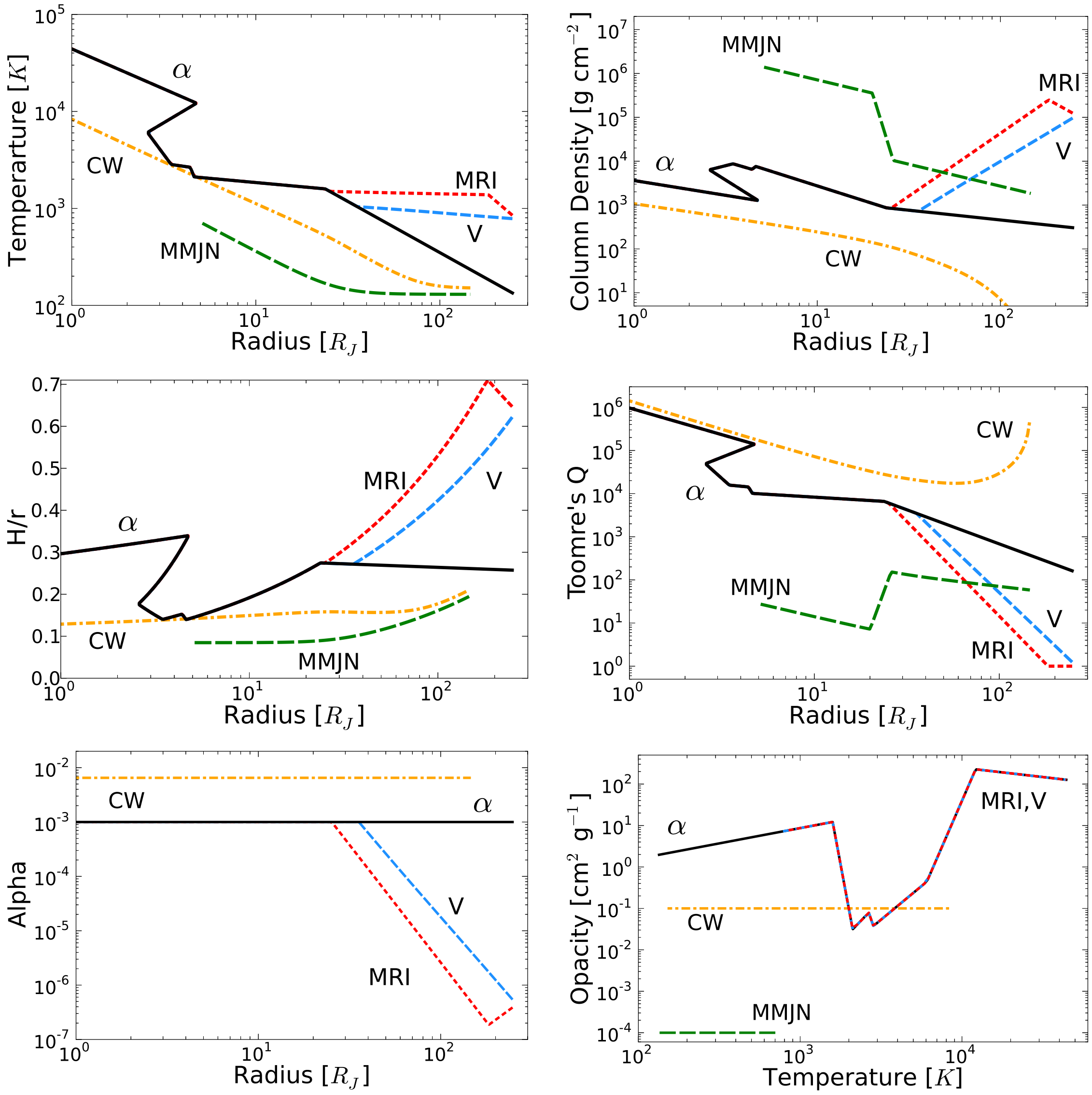

Figure 2.2: Radial dependence of the of the midplane temperature, T (top-left panel), column density, Σ (top-right panel), aspect ratio, H/r (centre-left panel), Toomre's Q (centre-right panel), and viscosity parameter α (bottom-left panel) for five circumplanetary disc models. Opacity as a function of temperature, $\kappa(\rho(T), T)$ is also shown (bottom-right panel). The constant-α model (solid curve; §2.6.1), and self-consistent accretion disc with an MRI field (dotted curve; §2.6.2), and vertical field (short-dashed curve; §2.6.2) are shown with the MMJN model (long-dashed curve; §2.6.3) and Canup & Ward disc (dot-dashed curve; §2.6.4) for comparison.

and thermal ionisation level is high enough for good magnetic coupling. The stronger coupling requirement for an MRI field makes for a slightly hotter and more dense disc than for accretion driven by a vertical field, and so the disc is gravoturbulent beyond $200\,R_J$, where the temperature profile steepens. There is no corresponding gravoturbulent region for the self-consistent accretion disc with vertical field. Nevertheless, the self-consistent accretion disc is remarkably similar when either the MRI or verticals used for drive accretion.

The profile for the constant-α disc follows $T \propto r^{-1.1}$ in the outer regions where the opacity is primary from grains [i.e., $a = 0, b = 0.74$; see equation (2.57)]. Of the parameter set α, $\dot{M}$ and M, the temperature profile is most sensitive to changes in the inflow rate. An order of magnitude change in $\dot{M}$ only corresponds to a factor ~ 3 change in the temperature across most of the disc, with little effect beyond $\sim 40\,R_J$.

The profiles are multivalued in the region $r \sim$ 2–5 R_J, with a characteristic 'S-shape'. Here the disc satisfies conditions for multiple opacity regimes, with the radially increasing, unstable branch corresponding to the H-scattering opacity regime. The viscous-thermal instability associated with this feature has been used to model outbursts in circumstellar discs surrounding T-Tauri stars - most notably FU Orionis outbursts by Bell et al. (1997).

The constant-α and self-consistent accretion discs are hotter than the Canup & Ward and MMJN discs, which aim to model a later phase of the disc when opacity is from ice grains (and necessarily lower; see the opacity profile in bottom-right panel of Fig. 2.2), and the disc is cool enough to form icy satellites. As inflow from the protoplanetary disc tapers, the disc cools, consistent with the evolution to an icy state recorded by the Solar System giant-planet satellite systems. For example, reducing the inflow rate by a factor of ten lowers the temperature to only 370 K at the disc outer edge.

The column density profile is shown in the top-right panel. The profile for the constant-α disc is generally shallow, decreasing by only a factor of ~ 12 between the inner and outer edge. Like the Canup & Ward disc, the column density is low compared with the MMJN, and so the disc is 'gas starved'. Consequently, the disc mass is also low, with $M_{\rm disc} = 1.6 \times 10^{-3} M_J$, validating our neglect of self gravity. On the other hand, the column density in the self-consistent accretion discs increase beyond $\sim 30\,R_J$ reaching $\Sigma = 9.6 \times 10^4\,{\rm g\,cm^{-2}}$ for a vertical field, and $\Sigma = 2.5 \times 10^5\,{\rm g\,cm^{-2}}$ for an MRI field. Consequently, the disc masses are large, with $M_{\rm disc} = 0.5\,M_J$ for the vertical field, and $M_{\rm disc} = 0.64\,M_J$ for the MRI field. The disc mass increases as the inflow rate from the protoplanetary discs tapers, such that a factor 10 reduction in the inflow rate leads to an inward extension of the gravoturbulent region, and a disc mass $M_{\rm disc} = 0.42\,M_J$, independent of the field geometry.

The centre-left panel of Fig. 2.2 shows the aspect ratio for each model. The aspect ratio for the constant-α model ranges between $H/r = 0.14$–0.34, with pressure dominating the scale height. Self-gravity is too weak to counteract strong thermal pressure in the outer regions of the self-consistent accretion discs and so the discs are very thick, with the aspect ratio reaching a maximum of $H/r = 0.63$, and 0.71 for a vertical and MRI field, respectively. Our results agree with Shabram & Boley (2013) in that circumplanetary discs may be more aptly described as 'slim' (i.e., $H/r \lesssim 1$) rather than 'thin'.

The thin-disc approximation is a cornerstone of analytic accretion disc models, as the vast difference in the length-scales in the vertical and radial directions lead to a clear separation of the treatment of processes in those two directions. Therefore, calculations beyond thin-discs are greatly complicated and simulations are often needed to resolve the behaviour. The large aspect-ratio of the solutions challenges the validity of our assumptions of vertical hydrostatic equilibrium, purely vertical heat transport, as well MRI relations [e.g., equation (2.38)] based on thin-disc simulations. The effect is greatest at the outer edge of our disc where conditions are so extreme as to be unrealistic. Unfortunately, little further can be said in the absence of simulations in the slim- and thick-disc regimes that are sorely needed to inform semi-analytic models.

In the outer regions where the aspect ratio is large ($r/H > 25$), mass accretion from spiral shocks may exceed that by gravitoturbulence (Savonije, Papaloizou & Lin, 1994). While it is not known how much accretion spiral shocks would contribute, the process may be self-limiting in this system as heating by spiral shocks nonlocal, reducing the disc temperature, and therefore the scale height.

The centre-right panel of Fig. 2.2 shows the radial profile for Toomre's Q. Toomre's Q is large for the low-mass constant-α disc, however, despite the high temperatures the self-consistent accretion discs reach $Q \sim 1$ at the outer edge where the column density is highest. We fix $Q = 1$ in the gravoturbulent region in the self-consistent accretion disc with MRI field.

The bottom-left panel of Fig. 2.2 shows the radial profile of the viscosity parameter, α. The viscosity parameter is constant across the Canup & Ward and constant-α discs, and in the inner regions of the self-consistent accretion discs where magnetic coupling is good and α is saturates at its maximum value. Once the temperature drops below $\sim 1000\,K$ thermal ionisation drops and with it the strength of magnetic coupling. Magnetic transport is less efficient with high diffusivity and so α is reduced, as per equation (2.58), reaching a minimum of 1.9×10^{-7} for an MRI field, and 4.8×10^{-7} for a vertical field. In the outer $\sim 60\,R_J$ of the self-consistent MRI accretion disc, α increases radially to compensate for the decreasing column density. However, such a low required effective viscosity is potentially overwhelmed by other processes, such as stellar forcing or satellitesimal wakes which may contribute additional torque exceeding this level (Rivier et al., 2012; Goodman & Rafikov, 2001).

Note that a property of this model is that temperature increases with decreasing α. This result is counter intuitive given that viscosity, and hence dissipation, are directly proportional to α. However, for a fixed $\dot{M}$, increasing α enhances the effectiveness of the turbulence and so reduces the required active column density [see equation (2.15)]. The associated reduction in optical depth lowers the midplane temperature relative to the surface temperature. Consequently, if we increase $\alpha_{\rm sat}$ to 10^{-2} which is appropriate for MRI with net magnetic flux, we find that the midplane temperature reaches at most 2100 K. We also find that the saturated magnetic transport region (i.e. where non-ideal effects are below the coupling threshold) only reaches out to $6\,R_J$, whereas the gravoturbulent region extends in as far as $120\,R_J$. However, we also note that increasing $\alpha_{\rm sat}$ requires a further reduction of the minimum value of α to 2.2×10^{-8} (at the boundary of the marginally coupled and gravoturbulent regions).

Opacity as a function of temperature is shown in the bottom–right panel of Fig. 2.2, using the corresponding density profile [i.e., $\kappa(\rho(r), T(r))$ vs $T(r)$]. The opacity is complex and varies by four orders of magnitude throughout the disc. Despite differences in the temperature and density profiles, the opacity profile for the self-consistent accretion discs follow that of the constant-α disc. This is because the discs only deviate in the Grains opacity regime where the opacity is density independent (i.e., $a = 0$).

2.7.2 Ionisation

Fig. 2.3 shows the electron (solid curve), ion (dashed curve), and charge-weighted grain (dotted curve) number density fraction for the constant-α model (top-left panel), and self-consistent accretion discs with MRI field (centre-left panel) and vertical field (bottom-left panel).

In the constant-α disc, the ionisation fraction is high within the inner disc. Close to the planet the disc is almost fully ionised by thermal ionisation of hydrogen and

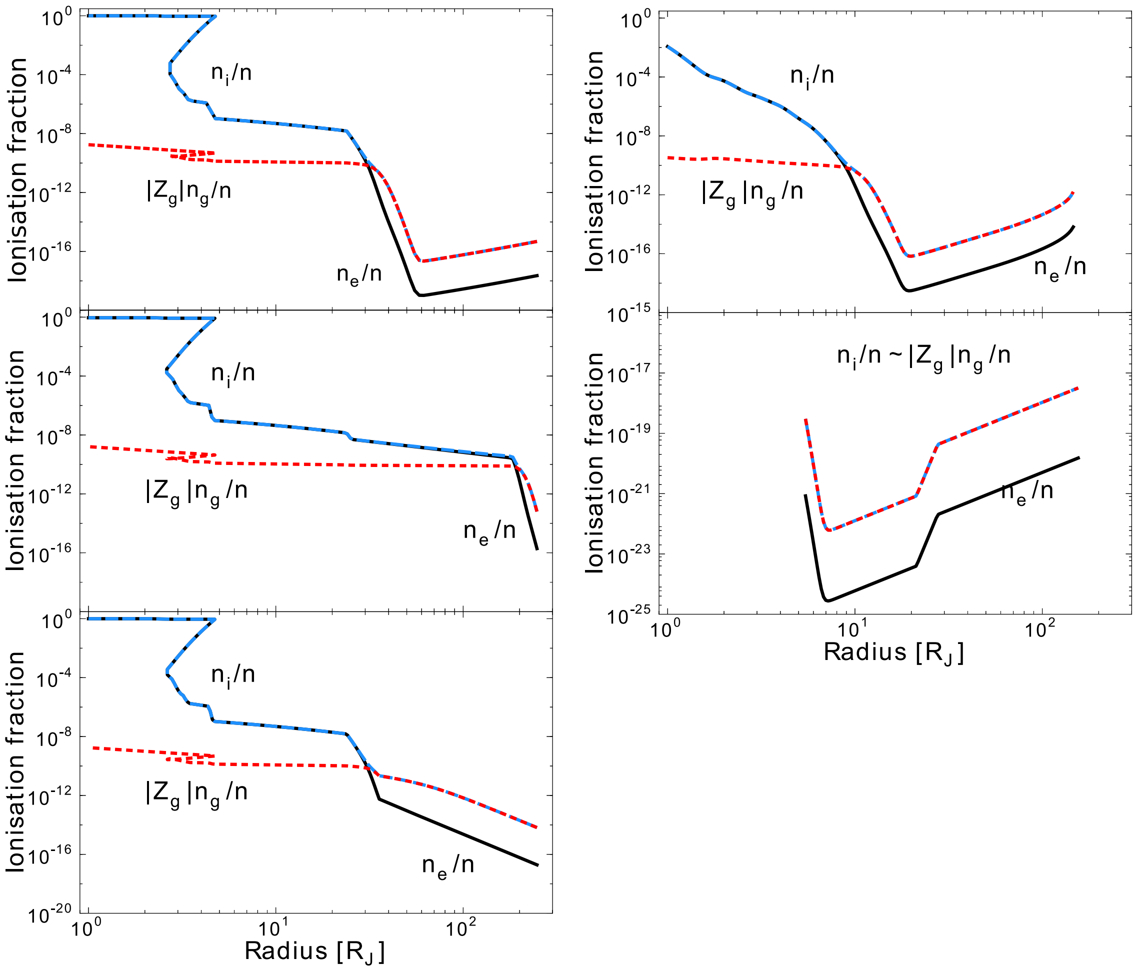

Figure 2.3: Radial dependence of the midplane ionisation fraction, n_e/n (solid curve), ion number density fraction, n_i/n (dashed curve), and charge-weighted grain number density fraction, $|Z_g|n_g/n$ (dotted curve) for the constant-α model (top-left panel) and self-consistent accretion disc with MRI field (centre-left panel), and vertical field (bottom-left panel). For comparison, charged number density fractions are also shown for the Canup & Ward α disc and MMJN in the top-right and bottom-right panels.

helium, and thermal ionisation continues out to $\sim 30\,R_J$ where the temperature exceeds $\sim 1000\,\mathrm{K}$ and potassium is thermally ionised. In the abundance of free electrons grains acquire a large negative charge, $Z_g \sim -660$, but with little effect on the total electron density. Beyond this distance, the disc is not hot enough for significant thermal ionisation and so the ionisation fraction drops sharply. Ionisation is primarily by radioactive decay beyond $60\,R_J$, and the ionisation fraction is low (i.e., $n_e/n \sim 10^{-19}$). In these conditions grains are mostly neutral, but still remove a large proportion of free electrons, reducing the electron density by a factor of ~ 190 relative to the ions.

Thermal ionisation is strong over a larger portion of the self-consistent accretion discs, as the disc structure is reliant on a higher level of ionisation in the marginally magnetically coupled region. We rely on thermal ionisation to achieve magnetic coupling, as midplane ionisation from radioactive decay, cosmic rays and X-rays is too weak (see §2.7.4). Grain charging is important beyond $\sim 40\,R_J$ for both field geometries, however it has a greater effect for the vertical field where the ionisation fraction is lower. All profiles are multivalued between $3\,R_J \leqslant r \leqslant 5\,R_J$, in keeping with the temperature profiles.

Depletion onto grains removes heavy elements from the gas phase, and consequently reduces the ionisation fraction between $3\,R_J \lesssim r \lesssim 60\,R_J$ in the constant-α disc. There is no depletion close to the planet where ionisation is from the non-depleted hydrogen and helium, and in the outer disc ionisation by radioactive decay is so weak that neutral metals are abundant (i.e., $n_i/n_n \ll x_{\mathrm{metals}}$) and the reaction rate is not limited by depletion. In the intermediate region depletion reduces the ionisation fraction by up to the depletion factor, $10^{-\delta} = 0.12$. The lowered electron density leads to a slight increase (up to 10%) in grain charge. Depletion at this level has no appreciable effect on the structure of the self-consistent accretion discs.

Additional ionisation from MRI is ineffective for both the constant-α and fixed-temperature discs. Grain capture through vertical mixing rapidly removes ionisation in eddies produced in MRI active surface layers. If grains are absent, charges are removed by recombination quickly over a time-scale $\tau_R \approx 4\Omega^{-1}$ at the outer edge. However, if grains are present, even at the level $f_{dg} \gtrsim 10^{-11}$, grain charge capture is rapid. Thus, free charges are rapidly removed as they are mixed into the dead zone and so do not contribute to midplane ionisation.

For ionisation produced through acceleration by MRI electric fields, we find that the electron energy is at most $\epsilon \approx 5 \times 10^{-3}\,\mathrm{eV}$ in the constant-α disc, and lower still in higher density self-consistent accretion discs. This energy is orders of magnitude

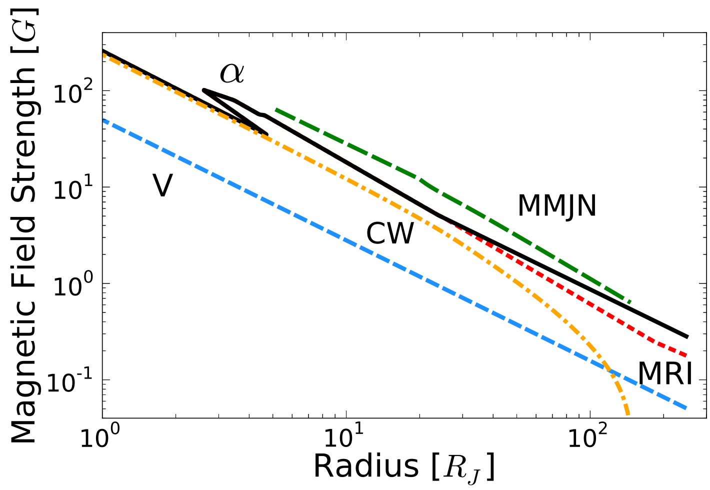

Figure 2.4: Radial dependence of the magnetic field strength, B, for the α model (solid curve), and fixed temperature model with MRI field (dotted curve), and vertical field (short-dashed curve), Canup & Ward α disc (dot-dashed curve), and MMJN (long-dashed curve).

too low to ionise any atomic species. Thus, there is no appreciable contribution from self-sustaining MRI ionisation in circumplanetary discs. Self-sustaining ionisation is more effective in protoplanetary discs where the density is lower such that electrons are able to be accelerated over a longer mean free path.

We have also calculated the charge number density fractions for the Canup & Ward α disc (top-right panel) and the MMJN (bottom-right panel) using the same method as given in §2.3. In the Canup & Ward α disc thermal ionisation is high close to the planet with cosmic ray ionisation dominant beyond $20\,R_J$, similar to the constant-α disc. In the MMJN the ionisation fraction is very low ($n_e/n < 10^{-16}$) due to both high surface density and low temperature.

2.7.3 Magnetic field strength

Fig. 2.4 shows the magnetic field strength for the constant-α model (solid curve), and self-consistent accretion discs with MRI field (dotted curve) and vertical field (dashed curve).

The MRI field strength for the constant-α disc varies between $B = 0.28$–$250\,$G, and follows $B \propto r^{-1.1}$ across most of the disc. The field strength for the self-consistent accretion disc with MRI field is almost identical to that of the constant-α disc, except for a small deviation at the outer edge where the temperature profiles diverge. The vertical field required for self-consistent accretion has a similar dependency, with

$B \propto r^{-5/4}$, but it is $\sim$5 times weaker and decreases monotonically. All disc model fields are sub-equipartition and are consistent with the estimate of B = 10–50 G at $10 R_J$ by Fendt (2003).

We have plotted the magnetic field strength required to drive accretion throughout the entire disc for the self-consistent accretion disc with MRI field. However, beyond 200 R_J accretion is powered by gravitoturbulence rather than magnetic fields. We have no information about the magnetic field in the gravoturbulent region.

For comparison we have calculated the MRI magnetic field strength for the Canup & Ward α disc and the MMJN, which we also show in Fig. 2.4. We calculate the field strength the Canup & Ward disc using equation (2.39) for their $\alpha = 6.5 \times 0^{-3}$, and for the MMJN using equation (2.41) assuming an accretion rate of $\dot{M} = 10^{-6}\, M_J$/year.

2.7.4 Magnetic coupling

Fig. 2.5 shows Ohmic resistivity (solid curve), Hall drift(dashed curve), and Ambipolar diffusion (dotted curve) scaled by the coupling threshold for the constant-α disc (top panel), and self-consistent accretion disc with MRI field (centre panel) and vertical field (bottom panel). The coupling threshold $\eta\Omega/v_a^2 = 1$ is used for the constant-α disc and self-consistent accretion disc with MRI field whereas $\eta\Omega/c_s^2 = 1$ is used for the self-consistent accretion disc with vertical field. The threshold is shown as a dotted horizontal line, with strong magnetic coupling in regions where each of the Ohmic, Hall and Ambipolar diffusivities are below the coupling threshold.

We find that all discs are dense enough that Ohmic diffusivity dominates over Hall and Ambipolar. The diffusivities follow the inverse of the ionisation fraction [i.e., $\eta \propto n/n_e$, see equations (2.52)–(2.54)]. Within 30 R_J, the ionisation fraction is high and so non-ideal effects are well below the coupling threshold, $\eta\Omega v_a^{-2} \ll 1$ or $\eta\Omega c_s^{-2} \ll 1$. At 30 R_J the diffusivities rise exponentially as thermal ionisation of potassium is suppressed by the low temperature. In the constant-α disc, ionisation from cosmic rays, X-rays and decaying radionuclides is too low for good magnetic coupling and so the majority of the disc, (i.e., $r > 30\, R_J$), is uncoupled from the magnetic field. The magnetically coupled region is larger at higher inflow rates where the midplane temperature is higher (i.e., the disc is coupled within 90 R_J for $\dot{M} = 10^{-5}\, M_J$/year), however this also produces a higher disc scale height, (aspect ratio up to 0.79), violating the 'thin-disc' approximation. Diffusivity below the coupling threshold in the inner disc indicates that the evolution of the disc and magnetic field are locked together, however the bulk of the disc is uncoupled to the magnetic field and accretion cannot proceed in these regions.

The boundary of the magnetically coupled region is controlled by the exponential rise in the diffusivity at the ionisation temperature of potassium. For instance, if a vertical field is used instead of an MRI field, the scaled diffusivity is reduced by a factor $(v_a/c_s)^2 = 4\alpha$ [using the MRI field to evaluate v_a; see equation (2.41)], but the steepness of the diffusivity profile at the coupling boundary means that there is no change in the magnetically-coupled boundary. Similarly, depletion of heavy elements onto grains increases the diffusivity between $3\,R_J \leqslant r \leqslant 60\,R_J$, but does not change the radius of the magnetically-coupled region.

The diffusivity profile for the self-consistent accretion disc with MRI field follows the constant-α disc profiles out until $30\,R_J$, where Ohmic diffusivity reaches the coupling threshold. Here, the disc enters the marginally magnetic coupled region and the rise in the diffusivity is not as steep. Although magnetic coupling is only weak, as the diffusivities are above the coupling threshold, it is still enough to drive accretion at the level given by equation (2.58). This state of marginal coupling occurs out to $200\,R_J$, with Ohmic diffusivity up to $\sim 10^4$ times greater than the coupling threshold. At the point where $Q = 1$ gravitoturbulence becomes the dominant transport mechanism and the diffusivities resume their exponential rise.

The coupling criterion for a vertical field is less stringent, and so non-ideal effects are lower relative to the coupling threshold within $r \sim 30\,R_J$. As with the self-consistent accretion disc with MRI field, the sharp rise in the diffusivity is reduced once the diffusivities reach the coupling threshold as the disc transitions to marginal magnetic coupling. However, in contrast, the disc never reaches $Q = 1$ and so there is no transition to the gravoturbulent region.

We have also calculated diffusivities for the Canup & Ward α disc (top-right panel) and the MMJN (bottom-right panel) for an MRI field. We show the absolute value of the Hall diffusivity for the Canup & Ward α disc as Hall diffusivity is negative beyond $r \sim 70\,R_J$ (shown by a dotted curve when $\eta_H < 0$). This occurs near the transition for ion re-coupling, and indicates that the Hall drift, between the field and neutrals, is in the opposite direction for a given field configuration. The diffusivities are above the coupling threshold for $r > 10\,R_J$ for the Canup & Ward α disc and at all radii for the MMJN, preventing magnetically-driven accretion in these regions.

2.8 Discussion

In this study we modelled steady-state accretion within a giant planet circumplanetary disc, and determined the effectiveness of magnetic fields and gravitoturbulence

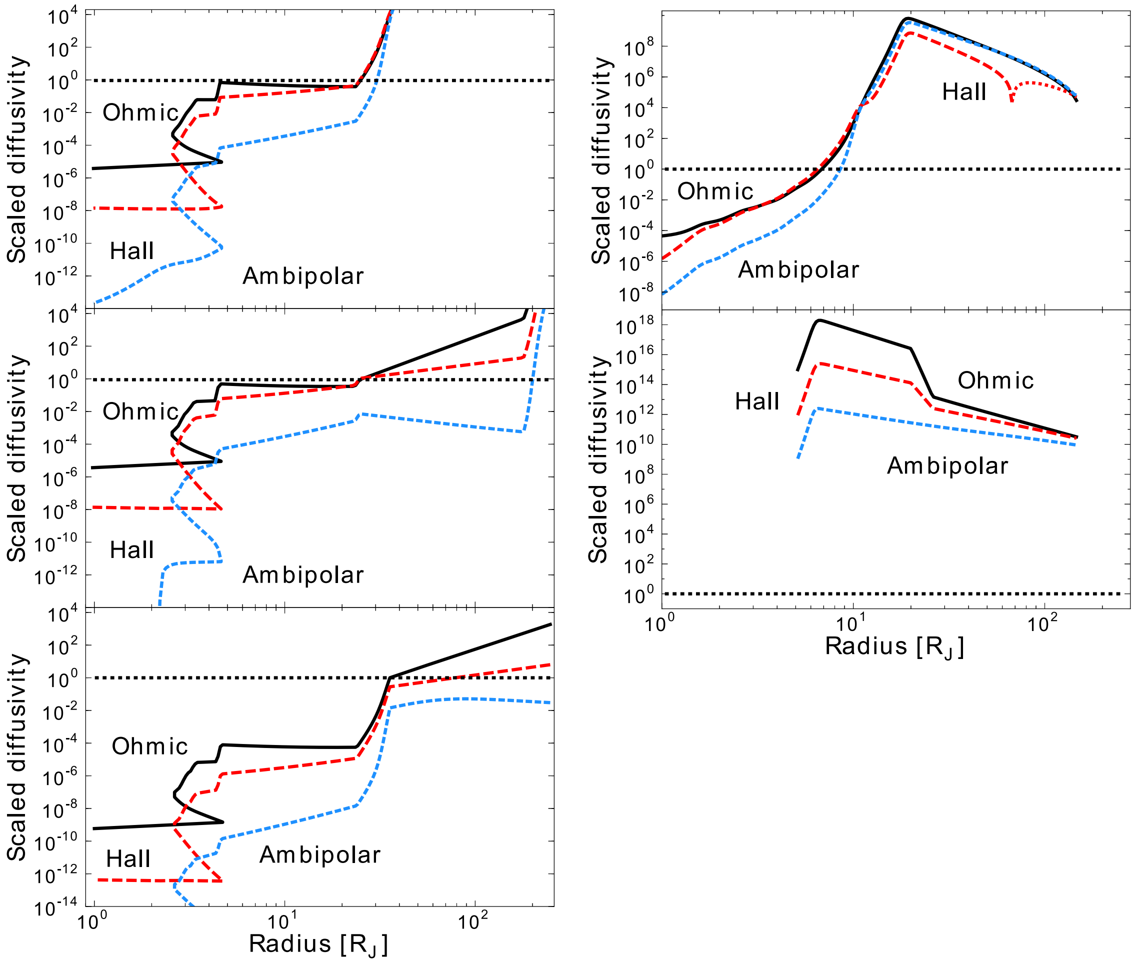

Figure 2.5: Radial dependence of Ohmic resistivity, η_O (solid curve), Hall drift, η_H (dashed curve) and ambipolar diffusion, η_A (dotted curve) scaled by the coupling threshold (dotted horizontal line). The MRI field coupling threshold, $\eta\Omega v_a^{-2} = 1$, is used for for the constant-α disc (top-left panel) and self-consistent accretion disc with MRI field (centre-left panel), whereas $\eta\Omega c_s^{-2} = 1$, is used for the self-consistent accretion disc with vertical field (bottom-left panel). Diffusivities for the Canup & Ward α disc and MMJN are calculated for an MRI field in the top-right and bottom-right panels for comparison.

in driving accretion. We modelled the disc as a thin Shakura-Sunyaev α disc, heated by viscous transport and solved for the opacity simultaneously with the disc midplane structure using the Zhu, Hartmann & Gammie (2009) opacity law, including the effects of self-gravity. Thermal ionisation dominates within $r \lesssim 30\,R_J$ where the disc reaches the ionisation temperature of potassium ($T \sim 10^3\,$K), but drops rapidly in cooler regions where ionisation is primarily by radioactive decay. The midplane is too dense for penetration of cosmic rays or stellar X-rays. We considered both an MRI field and a vertical field in driving accretion, and found that a field of order 10^{-2}–$10\,$G is needed to account for the inferred accretion rate onto the young Jupiter. To quantify the strength of interaction between the magnetic field and disc we calculated Ohmic, Hall, and Ambipolar diffusivities which cause slippage of the field lines relative to the bulk motion of the disc, decoupling their evolution.

In the standard constant-α disc, magnetic diffusivity is low enough for magnetic coupling in the inner region where potassium is thermally ionised. However, the remainder of the disc is too cool for thermal ionisation and so strong diffusivity prohibits magnetically-driven accretion throughout the bulk of the disc. The disc is gravitationally stable, with Toomre's $Q \gg 1$, and so there is no transport from gravitoturbulence either.

This is inconsistent with the assumption of a constant-α, and so we presented an alternate model in which α varies radially, ensuring that the accretion rate (taken to be uniform through the disc) is consistent with the level of magnetic coupling and gravitational instability. We achieved this by dividing the disc into three regions according to the mode of accretion: (i) the inner disc is hot enough for strong magnetic coupling through thermal ionisation and inflow is magnetically driven with α saturated at its maximum value; (ii) Beyond $30\,R_J$ the disc is too cool for sufficient thermal ionisation of potassium and diffusivity exceeds the coupling threshold. Accretion is still magnetically-driven, but as magnetic coupling reduces the efficiency with α inversely proportional to the level of magnetic coupling (Sano & Stone, 2002); (iii) The disc is gravitationally unstable in the outer regions where $Q \sim 1$, and so gravitoturbulence is produced and drives accretion. Accretion is self-regulated so that the disc maintains marginal stability with $Q = 1$. We calculated the disc structure for accretion driven by either MRI or vertical fields, finding very similar disc structures. With $Q \sim 1$ at the outer edge, the discs are massive with $M_{\rm disc} = 0.5\,M_J$.

MHD analysis by Fujii, Okuzumi & Inutsuka (2011) and Turner, Lee & Sano (2014) argue against magnetically driven accretion through the midplane where the cosmic-ray and X-ray fluxes are too low. We find that midplane magnetic coupling relies primarily on thermal ionisation and so the disc temperature is crucial. Fujii, Okuzumi & Inutsuka (2011) use the surface temperature which is necessarily cooler than the midplane temperature, and so no thermal ionisation is expected. Turner, Lee & Sano (2014) considers both MMJN models and actively supplied accretion disc models, appropriate for a later, and so cooler, phase than we consider here. MMJN models are necessarily cold to match conditions recorded by the final, surviving generation of Jovian moons, however these are likely formed late after a succession of earlier generations were accreted by the planet (Canup & Ward, 2006). Temperatures in actively accreting discs are controlled by the inflow rate which likely decreases as inflow from the protoplanetary disc tapers. Turner, Lee & Sano (2014) consider inflow rates that are lower than ours by a factor of 5–70, so these discs model a cooler stage and consequently thermal ionisation is limited to the inner $4\,R_J$ of their highest inflow disc. Additionally, we also consider accretion in regions which are only marginally coupled to the magnetic field. We find that while saturated magnetic transport (i.e. with strong magnetic coupling) is limited to the inner $30\,R_J$, magnetically driven accretion with marginal coupling can potentially occur across the entire disc.

We have modelled steady-state accretion within the disc, with the assumption that the disc evolves toward or through this state during the proto-planet accretion phase. Numerical simulations indicate that accretion discs, including circumplanetary discs, rapidly evolve away from a self-gravitating state toward a quasi-steady state (Forgan et al., 2011; Shabram & Boley, 2013), however there may be other time-dependent processes, such as short time-scale variability of inflow from the protoplanetary disc. Observations of accretion onto giant planets are needed to constrain accretion time-scales, and how rapidly the accretion rate can change.

The temperature profiles are multivalued in some regions of the disc, making the discs susceptible to viscous-thermal instability. This may lead to outbursts, undermining our steady-state assumption. This feature is only present when the inflow rate exceeds $\dot{M} = 2 \times 10^{-8}\,M_J/\text{year}$, and so outbursting from the viscous-thermal instability will not occur at later times when the inflow rate has tapered off to below this value. While there is certainly the potential for outbursting at earlier times, our analysis centres on whether inflow driven by magnetic fields is plausible, rather than advocating a steady state solution.

There may also be additional torques on the circumplanetary disc, from stellar forcing or spiral waves generated by satellitesimals (Rivier et al., 2012; Goodman & Rafikov, 2001; Szulágyi et al., 2014), which we have not included. It is not clear what level of transport these processes produce during this phase of giant planet accretion and whether they can be incorporated as additional sources within the Shakura-Sunyaev α formalism. We can model minor variations on the inflow parameters, such as a reduction in the accretion rate which reproduces cooling and disc-mass lowering as inflow from the protoplanetary disc tapers. However these results are uncertain as they require yet lower values of α in the self-consistent accretion disc which are likely overwhelmed by the additional torques mentioned above.

Strong magnetic coupling near the surface of the planet will affect accretion onto the planet surface. The planetary magnetic field may channel the accretion flow onto the planet surface (Lovelace, Covey & Lloyd, 2011), affecting the spin evolution of the planet (Takata & Stevenson, 1996; Lovelace, Covey & Lloyd, 2011), and temperature of the planet. However magnetospheric accretion requires diffusivity in order for the inflow to transfer onto the planetary magnetic field from the disc field. Loading onto the planetary field lines is only expected to occur close to the surface, if at all (at $r \sim 1$–$3\,R_J$; see Quillen & Trilling 1998; Lovelace, Covey & Lloyd 2011; Fendt 2003). However we find the diffusivity is very low at this distance, making loading of the gas onto the proto-planetary field lines from the disc field difficult. Magnetospheric accretion would require an additional source of diffusivity, such as electron momentum exchange with ion acoustic waves (e.g., see Petkaki et al., 2006), however it is not known how strong this effect is.

Circumplanetary discs are the formation site for satellites. The composition of the present day satellite systems around Jupiter and Saturn record conditions in their circumplanetary discs at the time of their formation. In particular, the rock/ice compositional gradients through the satellite systems set the disc ice line ($T \approx 250\,\mathrm{K}$) at the the location of Ganymede, $r = 15R_J$, and Rhea, $r = 8.7\,R_S$, in the Jovian and Saturnian systems, respectively (Mosqueira & Estrada, 2003). The location of the ice line is often incorporated or used as a measure of success in circumplanetary disc models (e.g., Lunine & Stevenson 1982; Mosqueira & Estrada 2003; Canup & Ward 2002), however no moons have been discovered beyond the Solar System and so it is not clear how typical the Jovian system is, nor to what degree these systems can vary (Kipping et al., 2013). It is not our aim to reproduce the conditions for moon formation, but rather we are focussed on modelling the early phase of the disc, in which the disc is hot and there is significant inflow onto Jupiter. Consequently, the ice line in our constant-α disc is at $r = 139\,R_J$, and the self-consistent accretion discs are too hot for ice. Several generations of satellites may have formed in these conditions, but the present day satellites likely form at a later stage when the disc has cooled as inflow into the circumplanetary disc tapers with the dispersal of the protoplanetary disc (Coradini et al., 1989; Canup & Ward, 2006; Sasaki, Stewart & Ida, 2010). Our results support the two stage circumplanetary disc evolution proposed by Coradini et al. (1989) in which the disc is initially hot and turbulent, but evolves to the cool quiescent disc as recorded by the giant planet satellite systems.

In summary, we have found that during the final gas accretion phase of a giant planet the circumplanetary disc is hot and steady-state accretion may be driven by a combination of magnetic fields and gravitoturbulence. Disc-wide, steady-state accretion requires a high temperature so that there is thermal ionisation through most of the disc.

3

Magnetic fields in gaps surrounding giant protoplanets

3.1 Introduction

Giant planets capture their massive atmospheres from the surrounding protoplanetary disc. As the planet grows, its gravitational sphere of influence expands so that the planet's tidal torque exceeds the viscous torque supplying gas to the vicinity of the planet, and a gap is evacuated in the nebula around the planet (Lin & Papaloizou, 1985; Artymowicz & Lubow, 1996; Bryden et al., 1999). Gaps have been seen in $\sim \mu$m scattered light around TW Hya and infrared polarimetry of surface dust around HD97048 (Debes et al., 2013; Garufi et al., 2014). Spiral waves, likely launched by a protoplanet, have also been seen in HCO^+ line emission within a gap in the HD 142527 circumstellar disc (Casassus et al., 2013).

A circumplanetary disc encircles the planet following the collapse and detachment of the protoplanet envelope from the nebula (Lunine & Stevenson, 1982; Ayliffe & Bate, 2009a). Gas flowing across the gap supplies the circumplanetary disc and controls the protoplanetary accretion rate (Lubow & D'Angelo, 2006). Gas with too much angular momentum to reach the planet directly is captured by the circumplanetary disc and its flow is controlled by angular momentum transport processes operating within the circumplanetary disc (Fujii, Okuzumi & Inutsuka, 2011; Lubow

& Martin, 2012; Rivier et al., 2012; Tanigawa, Ohtsuki & Machida, 2012, hereafter TOM12; Fujii et al., 2014; Keith & Wardle, 2014, hereafter KW14; Szulágyi et al., 2014; Turner, Lee & Sano, 2014). The circumplanetary flow pattern potentially comprises of high-altitude inflow, and midplane Keplerian and outflow components (Bate et al., 2003; D'Angelo, Kley & Henning, 2003, TOM12, Gressel et al., 2013). Although circumplanetary discs are yet to be observed, there are prospects for their detection through infrared spectral energy distributions observed with the James Webb Space Telescope or the Atacama Large Millimeter/submillimeter Array (ALMA; Isella et al., 2014; Dunhill, 2015; Zhu, 2015). This is strengthened by the recent observation of discs around three brown dwarfs, in infrared continuum and CO line emission (Ricci et al., 2014).

Magnetic fields likely play a role in the dynamics of the gap and circumplanetary disc system (Gressel et al., 2013; Uribe, Klahr & Henning, 2013, KW14, Turner, Lee & Sano, 2014). The field can have numerous effects, including generating hydromagnetic turbulence via the magnetorotational instability (MRI; Balbus & Hawley 1991; Hawley, Gammie & Balbus 1995), centrifugally-driven disc winds and jets (Blandford & Payne, 1982; Wardle & Königl, 1993), and magnetic braking (Matsumoto & Tomisaka, 2004).

Magnetic forces are transmitted by charged particles, and so these mechanisms require a minimum ionisation fraction. Collisions between charged and neutral particles give rise to non-ideal effects which counteract flux freezing - Ohmic resistivity, Hall drift, and ambipolar diffusion. Sufficiently strong resistivity and ambipolar diffusion decouple the motion of the gas and field (see Turner et al., 2014 and references within), and Hall drift can lead to complicated field evolution sensitive to the global field orientation (Wardle, 1999; Wardle & Salmeron, 2012; Kunz & Lesur, 2013; Lesur, Kunz & Fromang, 2014; O'Keeffe & Downes, 2014; Bai, 2015).

Gap-crossing dynamics is complex and so studies have relied on numerical simulations to model the flow. These include both grid-based (Bryden et al., 1999; Lubow, Seibert & Artymowicz, 1999; Bate et al., 2003; Lubow & D'Angelo, 2006, TOM12) and smoothed particle (Bryden et al., 1999; Ayliffe & Bate, 2009b, 2012) hydrodynamical, and ideal magnetohydrodynamical (MHD) simulations (Nelson & Papaloizou, 2003; Papaloizou, Nelson & Snellgrove, 2004; Uribe, Klahr & Henning, 2013). Global 3D MHD simulations of the wider system have also been used to generate synthetic observation maps for ALMA (Flock et al., 2015).

The recent inclusion of Ohmic resistivity adds an important level of realism to gap-crossing modelling (Gressel et al., 2013). Ohmic resistivity is strong in the dense circumplanetary disc, and can produce an MRI stable, dead zone with implications for planet growth and disc evolution. However, non-ideal effects are also at work in relatively low density regions where the Hall effect and ambipolar diffusion can be strong (Wardle, 2007). Their inclusion may enhance or suppress turbulence, affecting the flow and protoplanet growth rate. Indeed, the addition of ambipolar diffusion to resistive simulations radically alters the protoplanetary disc flow between 1–5 au, producing laminar accretion powered by a magnetocentrifugal wind, rather than the traditional accreting turbulent surface layers (Gressel et al., 2015).

In this chapter we perform a comprehensive study of the relative importance of Ohmic resistivity, Hall drift and ambipolar diffusion on fluid dynamics throughout the gap. Owing to the significant computational cost of including all three effects in a full, 3D simulation, we take an a posteriori, semi-analytic approach. We calculate MHD quantities using a snapshot from the TOM12 3D hydrodynamical simulation (described in §3.2.1). This allows us to calculate detailed ionisation maps including ionisation from cosmic-rays, stellar X-rays and radioactive decay, accounting for grain charging (§3.2.2 and §3.3.1). We determine the strength of non-ideal effects (§3.2.3 and §3.3.2) to estimate the field strength and geometry (§3.2.4 and §3.3.3). We find that the field would not alter the general fluid motion, justifying our use of an underlying hydrodynamical gap-crossing model (i.e., TOM12). The implications of incorporating magnetic fields and non-ideal effects in gap crossing, such as the additional force from large-scale fields, are considered (§3.4.1 and §3.4.2). Finally, we present a summary and discussion of findings in §3.5.

3.2 Model description

In this section we outline the disc model used to describe the protoplanetary disc and gap. We give details of the ionisation and diffusivity calculations, along with estimates for the magnetic field strength and geometry.

3.2.1 Disc and gap structure

We take a semi-analytic, a posteriori approach to the calculation. We use a snapshot of a pure hydrodynamical simulation as the basis for estimating MHD quantities. The protoplanetary disc and gap model that we use is the TOM12 three-dimensional, hydrodynamical simulation. The simulation models a protoplanetary disc surrounding a star of mass M_*, in which a gap has been carved out through gas capture by an embedded protoplanet of mass M_p, at fixed orbital radius d_p. The simulation corresponds to a protoplanet with the present-day mass and orbital radius of Jupiter (i.e., $M_p = M_J$, and $d_p = d_J$, where $d_J \equiv 5.2\,\text{au}$). Gas is treated as inviscid, and self-gravitational and magnetic forces are neglected.

The planet is located at the origin of a local cartesian coordinate system (x, y, z), which orbits the star at an orbital angular frequency Ω_p. The x-axis is oriented along the radial direction, $\hat{r}$, which extends from the star to the planet; the y-axis is oriented in the azimuthal direction, $\hat{\phi}$, parallel to the the protoplanet orbit; and the z-axis is parallel to the protoplanetary disc angular momentum vector. To capture details of the fine flow structure near the protoplanet the simulation has eleven levels of nested grids, each with $n_x \times n_y \times n_z = 64 \times 64 \times 16$ data points. The total simulated portion of the disc extends over $x \in [-12H_p, 12H_p]$, $y \in [-12H_p/d_p, 12H_p/d_p]$, and $z \in [0, 6H_p]$ where H_p is the scale height of the protoplanetary disc. The local cartesian approximation requires that the Hill radius,

$$\begin{aligned} R_H &= d_p \left(\frac{M}{3M_*}\right)^{\frac{1}{3}} \\ &\approx 0.36\,\text{au} \left(\frac{d_p}{5.2\,\text{au}}\right) \left(\frac{M}{M_J}\right)^{\frac{1}{3}} \left(\frac{M_*}{M_\odot}\right)^{-\frac{1}{3}}, \end{aligned} \tag{3.1}$$

which is roughly the feeding zone of the protoplanet, satisfies $R_H \ll d_p$. The simulation data used here was taken after 160.7 protoplanet orbits, allowing the simulation to approach a steady state. The gap reached a maximum density contrast relative to the unperturbed disc of ~ 9.

The simulation used a non-dimensionalised form for the MHD equations and so we must rescale the velocity $\mathbf{v} = (v_x, v_y, v_z)$ and density ρ data for our calculations. We rescale the column density using the minimum mass Solar nebula column density at the orbital radius of Jupiter $\Sigma_0 = 140\ \text{g}\,\text{cm}^{-2}$ (Kitamura et al., 2002; Williams & Cieza, 2011). This model estimates the gas mass in the Solar nebula by augmenting the solid material in Solar System planets with sufficient hydrogen and helium to bring the composition up to Solar (Weidenschilling, 1977; Hayashi, 1981). Observations of Class II Young Stellar Objects (i.e., those with discs and strong UV and Hα emission indicating active accretion) are currently limited to $\sim 20\,\text{au}$ resolution, however inferred disc column density profiles are broadly consistent with this profile. As the gap gas density naturally drops over time, we allow for simple reduction of the column density, $\Sigma(x, y, z)$, though multiplication of a constant parameter f_Σ, where $f_\Sigma = 1$ recovers the original TOM12 results.

The simulation is isothermal, and we adopt the temperature of a black body in radiative equilibrium with Solar luminosity, excluding any heating from inflow processes, at the orbital radius of Jupiter, $T = 120\,\mathrm{K}$ (Wardle, 2007). This is supported by interferometric CO images of T Tauri and dust temperatures from SED modelling (Guilloteau & Dutrey, 1998; Andrews & Williams, 2005; Piétu, Dutrey & Guilloteau, 2007).

We adopt Solar gas composition, with a mixture of 80% molecular hydrogen and 20% atomic helium. This corresponds to a mean molecular weight of $m_n = 2.34 m_p$, where m_p is the mass of a proton. This allows us to calculate the neutral number density, n, isothermal sound speed $c_s = 0.65\,\mathrm{km\,s^{-1}}$, and aspect ratio:

$$\frac{H_p}{d} = \frac{c_s}{v_k} \;=\; 4.5 \times 10^{-2} \left(\frac{d}{d_J}\right)^{\frac{1}{2}}, \tag{3.2}$$

where $v_k = (GM_*/d)^{\frac{1}{2}}$ is the Keplerian velocity.

The flow pattern within a gap transitions from orbiting the star [orbital radius $\sqrt{(x+d_p)^2 + y^2}$], to orbiting the planet (orbital radius $\sqrt{x^2+y^2}$) within the Hill sphere. In our analytic calculations we approximate the flow geometry by a composite Keplerian angular velocity functions:

$$\Omega = \begin{cases} \left[GM_p\,(x^2+y^2)^{-\frac{3}{2}}\right]^{\frac{1}{2}} & \text{for } \sqrt{x^2+y^2} \leqslant R_H, \\ \left[GM_*(x+d_p)^{-3}\right]^{\frac{1}{2}} & \text{otherwise.} \end{cases} \tag{3.3}$$

TOM12 also simulated the circumplanetary disc, but they note that as it is shear-dominated, artificial viscosity is strong and so the results are more reliable in the gap. Similarly we include the circumplanetary disc in our calculations with the caveat that the disc structure in this region is uncertain.

The scale height in the circumplanetary disc,

$$H_c \;=\; H_p \left(\frac{\sqrt{x^2+y^2}}{3R_H}\right)^{\frac{3}{2}} \tag{3.4}$$

$$\approx\; 5.2 \times 10^{-2} H_p \left(\frac{\sqrt{x^2+y^2}}{0.2\,R_H}\right)^{\frac{3}{2}}, \tag{3.5}$$

is significantly lower, and this needs to be accounted for when calculating gradients in the fluid flow (see §3.2.3). To that end we use a composite scale-height, H, which transitions at the boundary of the circumplanetary disc hydrostatic region:

$$H = \begin{cases} H_c & \text{for } \sqrt{x^2+y^2} < 0.2R_H,\ z/H_c < 5, \text{ and} \\ H_p & \text{otherwise.} \end{cases} \tag{3.6}$$

3.2.2 Degree of ionisation

Charged particles transmit magnetic forces to the bulk neutral flow. In the gap, ionisation is largely caused by penetrating cosmic-rays and stellar X-rays, but there is also a weak, pervasive contribution from decaying nuclides. We calculate the ionisation level by solving coupled rate equations for electron and ion number densities and mean grain charge subject to overall charge neutrality. We follow the method outlined in §2.3.2, but using a more detailed calculation of the grain charge. A summary of the method is given below.

We calculate the grain number density, n_g, for spherical grains with radius $a_g = 0.1\,\mu$m and bulk density $3\,\mathrm{g\,cm^{-3}}$ with a constant dust-to-gas mass ratio $f_{dg} \sim 10^{-4}$ to account for incorporation of solids into protoplanetary bodies (Pollack et al., 1994).

Internal ionisation from radioactive decay is primarily from the short-lived radionuclide ^{26}Al, which contributes an ionisation rate $\zeta_{\mathrm{R}} = 7.6 \times 10^{-19}\,\mathrm{s^{-1}}\,(f_{dg}/f_{\odot})$ (Umebayashi & Nakano, 2009). The ionisation rate has been scaled by the ratio of the dust mass fraction to the Solar photospheric metallicity, $f_{\odot} = 1.3\%$, so that the ^{26}Al abundance is consistent (Asplund et al., 2009). The midplane dust fraction will be enhanced by settling, however the consequent increase in the ionisation fraction will be small as ionisation is predominantly by external radiation.

External ionisation sources are attenuated by the column density above and below each location in the disc. Cosmic-ray ionisation occurs at the interstellar cosmic-ray ionisation rate, $\zeta_{\mathrm{CR}} = 10^{-17}\,\mathrm{s^{-1}}$, attenuated by the attenuation depth $\Sigma_{\mathrm{CR}} = 96\,\mathrm{g\,cm^{-2}}$ approaching from above and below the disc (Umebayashi & Nakano, 1981, 2009). We account for ionisation from diffuse scattered stellar X-rays but neglect direct illumination, instead assuming that shielding by the inner portion of the disc is effective. Ionisation for solar luminosity stellar X-rays occurs at a rate $\zeta_{\mathrm{XR}} = 9.6 \times 10^{-17}\,\mathrm{s^{-1}}\,(d/d_J)^{-2}$, with attenuation depth $\Sigma_{\mathrm{XR}} = 8\,\mathrm{g\,cm^{-2}}$ (Igea & Glassgold, 1999; Turner & Sano, 2008). The total ionisation rate, ζ, is the sum from the three sources $\zeta = \zeta_{\mathrm{R}} + \zeta_{\mathrm{CR}} + \zeta_{\mathrm{XR}}$.

We solve for the electron, ion and grain charge number densities by calculating the grain charge needed for overall charge neutrality in the steady state [see equations (2.25)–(2.28)]. We include charge focussing in the electron and ion capture rate coefficients for grains (Umebayashi & Nakano, 1980):

$$k_{ig} = \pi a_g^2 \sqrt{\frac{8k_bT}{\pi m_i}} \times \begin{cases} \exp\left(-\frac{e^2|Z_g|}{a_g k_b T}\right) & Z_g < 0 \\ \left(1 + \frac{e^2|Z_g|}{a_g k_b T}\right) & Z_g > 0 \end{cases} \tag{3.7}$$

$$k_{eg} = \pi a_g^2 \sqrt{\frac{8k_bT}{\pi m_e}} \times \begin{cases} \left(1 + \frac{e^2|Z_g|}{a_g k_b T}\right) & Z_g < 0 \\ \exp\left(-\frac{e^2|Z_g|}{a_g k_b T}\right) & Z_g > 0 \end{cases} \tag{3.8}$$

where $Z_g e$ is the mean grain charge, k_b is Boltzmann's constant, and m_e is electron mass. We model metals as a single species, adopting the mass, m_i, and abundance, x_i, of the most abundant metal - magnesium (Lide, 2004; Asplund et al., 2009). The recombination rate for ions and electrons is $k_{ei} = 1.20 \times 10^{-12}\ (T/1000\,\mathrm{K})^{-0.7}\,\mathrm{cm^3\,s^{-1}}$ (McElroy et al., 2013). If the grain charge is known these equations give the ion and electron number densities:

$$n_e = \frac{n_g k_{ig}}{2k_{ei}} \left[\left(1 + \frac{4k_{ei} n \zeta}{k_{eg} k_{ig} n_g^2}\right)^{\frac{1}{2}} - 1 \right] \tag{3.9}$$

$$n_i = n_e \frac{k_{eg}}{k_{ig}}. \tag{3.10}$$

Equations (3.7)–(3.10) are analogous to equations (2.29)–(2.32) except for the inclusion of a non-zero grain charge for charge focussing. The protoplanetary disc has a higher average ionisation fraction resulting in a higher grain charge which cannot be neglected (as it could be in our analysis of the circumplanetary disc analysis in Chapter 2). We determine the equilibrium values of n_e, n_i, and Z_g numerically by solving equations (3.7)–(3.10) along with charge neutrality, for the grain charge. We use the Brent-Dekker method, `gsl_root_fsolver_brent`, for root-finding implemented in the GNU Scientific Library to solve for the grain charge to an accuracy of 1% (Galassi et al., 2009). This method combines bisection and secant methods for rapid convergence.

We also determine the effectiveness of collisional ionisation produced in MRI turbulent regions. Currents generated by an MRI field may be sufficient to ionise neutral particles, providing additional ionisation (Muranushi, Okuzumi & Inutsuka, 2012; Okuzumi & Inutsuka, 2015). We calculate the kinetic energy of accelerated particles using equations (2.36)–(2.37) to determine if it exceeds the ionisation potential of neutral species (e.g., potassium has the lowest ionisation energy of the abundant elements, with $E \sim 4.34\,\mathrm{eV}$). We find that, although electrons reach energies of up to $1\,\mathrm{eV}$ in the disc atmosphere ($z \sim 5H_p$) where collisions are infrequent and the mean-free path is long, in the denser midplane electrons are not accelerated above 0.05 eV. This is too low to ionise any atomic species and so the MRI does not contribute significantly to ionisation. Thus, we neglect the effect in our calculation of the ionisation fraction.

Finally, we note that thermal ionisation is likely not effective in the gap surrounding Jupiter. At the orbital distance of Jupiter the protoplanetary disc is much cooler than the required $T \sim 1000\,\mathrm{K}$, and further shock heating of accreting material at the circumplanetary disc is weak. In the circumplanetary shock, shock heating flux $F_\mathrm{s} \sim \sigma(40\,\mathrm{K})^4$ (calculated for an accretion rate $10^{-6} M_J/\mathrm{year}$, at $r \sim 300 R_J$ from the protoplanet; Cassen & Moosman, 1981) is negligible compared with Solar irradiation, $F_\odot = \sigma(120\,\mathrm{K})^4$ at this orbital radius, precluding thermal ionisation.

3.2.3 Non-ideal MHD effects and magnetic coupling

The evolution of the magnetic field and its role in the gas dynamics depends on the strength and nature of the magnetic coupling between the field and gas. Magnetic coupling is manifest in the induction equation,

$$\frac{\partial \mathbf{B}}{\partial t} = \nabla \times (\mathbf{v} \times \mathbf{B}) - \nabla \times [\eta_O(\nabla \times \mathbf{B}) + \eta_H(\nabla \times \mathbf{B}) \times \hat{\mathbf{B}} + \eta_A(\nabla \times \mathbf{B})_\perp], \quad (3.11)$$

where η_O, η_H, and η_A are the transport coefficients for Ohmic resistivity, Hall drift, and ambipolar diffusion. These non-ideal effects cause the magnetic field to slip through the gas, and can dominate the field evolution if they are too strong. They are caused by neutral collisions disrupting the $\mathbf{E} \times \mathbf{B}$ drift of charged particles. Differences in the density dependence of these effects leads to three different regimes in which Ohmic resistivity, Hall drift and ambipolar diffusion are most effective in high, moderate, and low density regions, respectively. For a predominantly vertical magnetic field, Ohmic resistivity and ambipolar diffusion act similarly (and distinctly from the Hall drift), and so they are often combined into the Pedersen diffusion $\eta_P = \eta_O + \eta_A$. We calculate the strength of the three effects using the transport coefficients from equations (2.52)–(2.54).

How strong these effects must be to dominate the inductive term and decouple the motion of the field and gas depends on the field geometry. Below we outline the coupling conditions for MRI turbulent, toroidal, and poloidal components in turn.

The MRI dynamo harnesses shear to generate a turbulent field. Magnetic diffusion restricts MRI turbulence by limiting bending of the smallest-scale field modes. The MRI operates effectively if the fastest growing mode, with wavelength $\lambda =$

$2\pi v_a/\Omega$, survives diffusion. Magnetic diffusion counteracts dynamo growth of short-wavelength fluctuations with wavelength $\lambda < \eta/v_{a,z}$, for which the diffusion rate exceeds the growth rate. Here $v_{a,z} = B_z/\sqrt{4\pi\rho}$ the vertical Alfvén speed. Thus, the MRI operates in effectively ideal MHD conditions if Pedersen and Hall components are simultaneously below the threshold (Sano & Stone, 2002; Turner et al., 2014):

$$\eta_P \lesssim v_{a,z}^2 \Omega^{-1} \text{ and } |\eta_H| \lesssim v_{a,z}^2 \Omega^{-1}. \tag{3.12}$$

Here, the absolute value of the Hall term reflects its signed nature. The MRI also requires the field must be weak enough that the fastest-growing mode is confined within the disc scale height, so that for ideal MRI (Okuzumi & Hirose, 2011):

$$\beta_z = \frac{8\pi\rho c_s^2}{B_z^2} > 8\pi^2. \tag{3.13}$$

Unlike Ohmic resistivity and ambipolar diffusion, Hall drift is not diffusive[1] and can change the behaviour of MRI turbulence, even in the presence of strong Ohmic and ambipolar diffusion. Hall drift is antiparallel to the current density and may cooperate with, or act against, Keplerian shear according to the relative orientation of the protoplanetary disc angular momentum vector and vertical component of the magnetic field, $s = \mathrm{sign}(\mathbf{B} \cdot \boldsymbol{\Omega})$ (Wardle, 1999; Balbus & Terquem, 2001; Wardle & Salmeron, 2012). For example, if the field is aligned with the rotation axis, the Hall effect can destabilise the flow, enhancing turbulence. On the other hand, if the field and rotation axis are anti-aligned, Hall drift acts against the shear, suppressing turbulence.

In the Hall-MRI regime, the Hall effect counteracts Pedersen stabilisation against field tangling if it dominates and the vertical field orientation is favourable (Wardle & Salmeron, 2012; Lesur, Kunz & Fromang, 2014). Hall-MRI requires

$$|\eta_H| > \eta_P,\ |\eta_H| > v_{a,z}^2 \Omega^{-1}, \text{ and } s = 1, \tag{3.14}$$

along with a Hall-MRI weak-field criterion, which we show in Appendix A.1 is the same as equation (3.13). Indeed, Hall drift need not dominate diffusion to impact turbulence, as even weak Hall drift modifies the wave number and growth rate of the fastest growing mode (Wardle & Salmeron, 2012).

A toroidal field surrounding the star or protoplanet, must also be maintained

[1] Indeed, Kunz & Lesur (2013) found that the Hall effect can be *anti-diffusive* in unstratified shearing boxes.

against diffusion which would tend to unwrap and straighten field lines. The impact of non-ideal effects on a toroidal field are most important close to the central object where gradients are strongest. A toroidal field is preserved against diffusion if magnetic induction exceeds non-ideal effects, as captured by the coupling threshold derived in Appendix A.2 (c.f., Turner & Sano, 2008):

$$\eta_P \lesssim \Omega H^2, \text{ and } |\eta_H| \lesssim \Omega H^2. \tag{3.15}$$

A toroidal field can also be preserved against strong diffusion if Hall drift dominates. Hall drift is along the current, which is in the fluid rotation direction for both the aligned and anti-aligned cases (i.e., $s = 1$ and $s = -1$). So, either by enhancing field-wrapping (i.e., for $s = 1$) or by unwinding and rewrapping the field in the counter flow direction (i.e., for $s = -1$), the Hall effect produces a strong negative toroidal field. See Appendix A.2 for a discussion of the effect of vertical field direction dependence for coupling of a toroidal field. Simulations are needed to verify this behaviour, but we highlight Hall-dominated regions with the anticipation it may extend the reach of the toroidal field. We simply require that azimuthal winding from Hall drift exceeds diffusion:

$$|\eta_H| > \eta_P, \; |\eta_H| > \Omega H^2. \tag{3.16}$$

Finally, the disc contains a poloidal field component throughout. Although magnetic coupling limits the minimum field bending radius of the poloidal component, an essentially vertical field will always couple, owing to its small gradient. As we are not concerned with the exact geometry of the poloidal component, we simply assume that it is approximately vertical, couples everywhere and so permeates the gap.

3.2.4 Magnetic field strength and geometry

Protoplanetary discs inherit a large-scale magnetic field from their progenitor molecular cloud. Field measurements are difficult as current observations are limited to $\sim 100\,\mathrm{au}$ resolution (Stephens et al., 2014). The disc field is certainly compressionally enhanced over the cloud field ($B \sim 1$–$100\,\mathrm{mG}$; Shu, Adams & Lizano, 1987), while the equipartition field $B_{\rm eq} = \sqrt{8\pi p}$ provides a maximum field strength the disc will support before magnetic forces exceed the thermal pressure, $p = \rho c_s^2$.

Nevertheless, it is possible to gain a more precise estimate from the stellar accretion rate, $\dot{M} \sim 10^{-8}\,M_\odot\,\mathrm{year}^{-1}$, as the field is thought to play a principle role in angular momentum transport (Hartmann et al., 1998; see references in McKee & Ostriker, 2007). This can be made from the azimuthal component of the axisymmetric momentum equation, vertically integrated between the disc surfaces (Wardle, 2007),

$$\rho \left[(\mathbf{v} \cdot \nabla) \, \mathbf{v} \right]_\phi = \frac{(\mathbf{B} \cdot \nabla \mathbf{B})_\phi}{4\pi}. \tag{3.17}$$

This yields a minimum field strength for vertical, toroidal, and turbulent components in the disc (Wardle, 2007):

$$B_z = 6.0 \times 10^{-3}\,\mathrm{G} \left(\frac{\dot{M}}{10^{-8}\,M_\odot\,\mathrm{year}^{-1}} \right)^{\frac{1}{2}} \left(\frac{\Omega}{1.7 \times 10^{-8}\,\mathrm{s}^{-1}} \right)^{\frac{1}{2}} \left(\frac{d}{d_p} \right)^{-\frac{1}{2}}, \tag{3.18}$$

$$B_\phi = 2.8 \times 10^{-2}\,\mathrm{G} \left(\frac{\dot{M}}{10^{-8}\,M_\odot\,\mathrm{year}^{-1}} \right)^{\frac{1}{2}} \left(\frac{\Omega}{1.7 \times 10^{-8}\,\mathrm{s}^{-1}} \right)^{\frac{1}{2}} \left(\frac{H_p}{0.23\,\mathrm{au}} \right)^{-\frac{1}{2}}, \tag{3.19}$$

$$B_{\mathrm{MRI}} = 5.7 \times 10^{-2}\,\mathrm{G} \left(\frac{\dot{M}}{10^{-8}\,M_\odot\,\mathrm{year}^{-1}} \right)^{\frac{1}{2}} \left(\frac{\Omega}{1.7 \times 10^{-8}\,\mathrm{s}^{-1}} \right)^{\frac{1}{2}} \left(\frac{H_p}{0.23\,\mathrm{au}} \right)^{-\frac{1}{2}} \tag{3.20}$$

respectively. Components of the turbulent field are (Sano et al., 2004):

$$B_{\mathrm{MRI},r} = 0.35 B_{\mathrm{MRI}}, \tag{3.21}$$

$$B_{\mathrm{MRI},\phi} = 0.92 B_{\mathrm{MRI}}, \text{ and} \tag{3.22}$$

$$B_{\mathrm{MRI},z} = 0.19 B_{\mathrm{MRI}}. \tag{3.23}$$

We now turn to estimating the magnetic field strength in the gap. Turbulence would be continuously generated there so equations (3.20)–(3.23) remain valid, however our estimates of the vertical and toroidal fields are not sufficient in the gap.

A poloidal component would be drawn in with the flow and reduced or enhanced in keeping with the large density variation across the gap. We assume that the field is frozen into the gas at the outer edge of the gap (at $x_g = 1.45\,\mathrm{au}$), drawn into the gap by the flow. We verify the self-consistency of this assumption with our results (see §3.3.2 and §3.4.2). The field would be pinned to the flow at the lowest magnetically-coupled gas layer, reducing or enhancing the field according to $B \propto \Sigma^{-1}$. Nevertheless, for simplicity, we assume the field is pinned at the midplane, with a field strength $B_{z,g} = 4.4 \times 10^{-3}\,\mathrm{G}$, given by equation (3.18) at $x_g = 1.45\,\mathrm{au}$, $y = 0$ where $\Sigma_g = 97\,\mathrm{g\,cm}^{-2}$. Normalising to the field strength at the outer edge of the gap, this leads to a vertical field strength profile of

$$B_z = B_{z,g}\left(\frac{\Sigma}{\Sigma_g}\right) \tag{3.24}$$

in the gap.

Determining the toroidal field strength is considerably more difficult as the field would be wound up continually until field-line drift balances differential rotation. As this is beyond the scope of our treatment, we simply assume the constant ratio $\sqrt{d/H_p}$ between the toroidal and vertical components in the disc is preserved for our estimate in the gap. This leads to a gap toroidal field strength profile of:

$$B_\phi = B_{\phi,g}\left(\frac{\Sigma}{\Sigma_g}\right), \tag{3.25}$$

where $B_{\phi,g} = 2.0\times10^{-2}\,\mathrm{G}$ is the toroidal field strength, likewise taken at $x_g = 1.45\,\mathrm{au}$, $y = 0$. We cap the field strength so that the associated magnetic pressure does not exceed the gas pressure:

$$\beta_\phi \;=\; \frac{8\pi\rho c_s^2}{B_\phi^2} \geqslant 1. \tag{3.26}$$

This allows the field to expand in response to strong magnetic pressure at high altitude, correspondingly reducing the field strength.

Numerical simulations suggest that the toroidal component may be subject to periodic polarity reversals, as it is lost through magnetic buoyancy every ~ 40 orbits (Miller & Stone, 2000; Shi, Krolik & Hirose, 2010; Hirose & Turner, 2011; Flock et al., 2012). The magnitude of the toroidal field would also vary vertically between its surface value, $B_{\phi,s}$, and zero at the midplane, with the approximate scaling $B_\phi \sim B_{\phi,s}(z/H_p)$, appropriate for a thin, rotationally-supported disc that is well coupled to the magnetic field (Wardle & Königl, 1993).

For simplicity we take B_ϕ constant with height, but account for vertical gradients (e.g., in Appendix A.2), and probe the effect of uncertainty by global enhancement or reduction of the the poloidal and toroidal components through multiplication by a constant parameter f_B.

Self-consistent coupled field geometry

The variation of diffusion and field gradients across the gap means that not all three field components are present everywhere. Here we determine where non-ideal effects

Table 3.1: List of parameters varied in this study.

Parameter	Standard value	Description
$f_{\rm dg}$	10^{-4}	Gas-to-dust mass ratio
f_Σ	1	Global multiplying factor for disc column density
f_B	1	Global multiplying factor for net magnetic field strength
s	1	$\mathrm{sign}(\mathbf{B}\cdot\mathbf{\Omega}) = \pm 1$ according to orientation of magnetic axis

permit each field component. We use the diffusivities to determine the magnetic structure based on the level of coupling for each field component (poloidal, toroidal, and turbulent), and only include the components where they couple.

Our procedure for calculating the field geometry is:

1. Poloidal field - we include a poloidal component at all locations, calculated with equation (3.18) in the main protoplanetary disc (i.e., $|x| > x_g$), or using the flux-conserved form, equation (3.24), inside the gap. It is safe to include a poloidal component everywhere as a pure vertical field always couples and any radial bending will adjust to the level of diffusion.

2. Toroidal field - we calculate the toroidal component strength using equation (3.19) in the bulk protoplanetary disc flow, and equation (3.25) in the gap. We cap the field strength by the gas pressure through equation (3.26). We calculate η_O, η_H, and η_A using the net field strength, $B = \left(B_z^2 + B_\phi^2\right)^{1/2}$, and determine if the field is coupled using equations (3.15) and (3.16). If the field is coupled the toroidal component is kept; otherwise it is set to zero.

3. MRI turbulent field - finally, we determine if an MRI turbulent field is sustained. We calculate the turbulent field strength in both the protoplanetary disc and the gap using equations (3.20)–(3.23). We calculate η_O, η_H, and η_A using the net field strength, $B = \left[B_{\mathrm{MRI},r}^2 + (B_\phi + B_{\mathrm{MRI},\phi})^2 + (B_z + B_{\mathrm{MRI},z})^2\right]^{1/2}$, and determine if the field is sustained using equations (3.12)–(3.13).

3.3 Results

Here we present the results of the calculations developed in §3.2, including the ionisation fraction, magnetic field, and strength of non-ideal MHD effects. Figures are shown for a Jupiter-mass planet, orbiting a Solar-mass star, at the present orbital distance of Jupiter. Unless otherwise stated, we take $f_{dg} = 10^{-4}$, $f_\Sigma = 1$, $f_B = 1$, and $s = 1$ (see Table 3.1).

3.3.1 Degree of ionisation

Fig. 3.1 shows the resulting ionisation profiles within the gap and disc. The top and centre panels show 2D slices through the gap, with the colour scale showing the ionisation fraction. The top panel shows the top-down view in the x–y plane at the midplane, and the centre panel shows the edge-on profile in the x–z plane at $y = 0$. The star is located beyond the simulation boundary at $x = -d_J$, $y = 0$. Small white patches in the top- and bottom-right corners of the edge-on profiles are beyond the simulation boundary. The bottom panel shows the dependence of the vertical ionisation profile on the dust-to-gas mass ratio, at $x = 0.3\,\mathrm{au}$, $y = 0$.

Shielding from the overlying gas reduces the ionisation fraction with decreasing height and in denser regions. X-rays penetrate to $z \sim H_p$, while cosmic rays reach everywhere except for the circumplanetary disc (located at $x, y \lesssim 0.1\,\mathrm{au}$), owing to its high column density. Instead, ionisation in the circumplanetary disc is from radioactive decay, which is a much weaker ionising source. Consequently, the ionisation fraction in the circumplanetary disc is much weaker than in the protoplanetary disc, as supported by previous studies (Fujii, Okuzumi & Inutsuka 2011; Fujii et al. 2014, KW14, Turner, Lee & Sano 2014). The sharp drop in the ionisation fraction profile at $z \sim H_p$ occurs at the shock boundary surrounding the circumplanetary disc, visible as a halo of poorly ionised gas in the edge-on view shown in the centre panel of Fig. 3.1.

Dust grains reduce the ionisation fraction by soaking up free electrons. Grain charge capture is significant, and most efficient, at the midplane where grains are abundant. It also reduces radioactive decay, influencing ionisation, and hence the potential for magnetic coupling, in the circumplanetary disc.

3.3.2 Non-ideal MHD effects and magnetic coupling

Fig. 3.2 shows diffusivity profiles for the gap. The top and centre panels show 2D slices through the gap, with the colour scale showing the field perpendicular diffusivity $\eta_\perp = (\eta_P^2 + \eta_H^2)^{1/2}$, along with logarithmically-spaced contour levels. The top panel shows the top-down view at the midplane, and the centre panel shows the edge-on profile at $y = 0$. The bottom panel shows the vertical profiles of the transport coefficients of Ohmic resistivity, Hall drift and ambipolar diffusion, along with the coupling threshold for toroidal and MRI fields.

Ohmic resistivity traces high density structures such as the spiral arms and circumplanetary disc and is lowest in the evacuated regions to the upper-right and

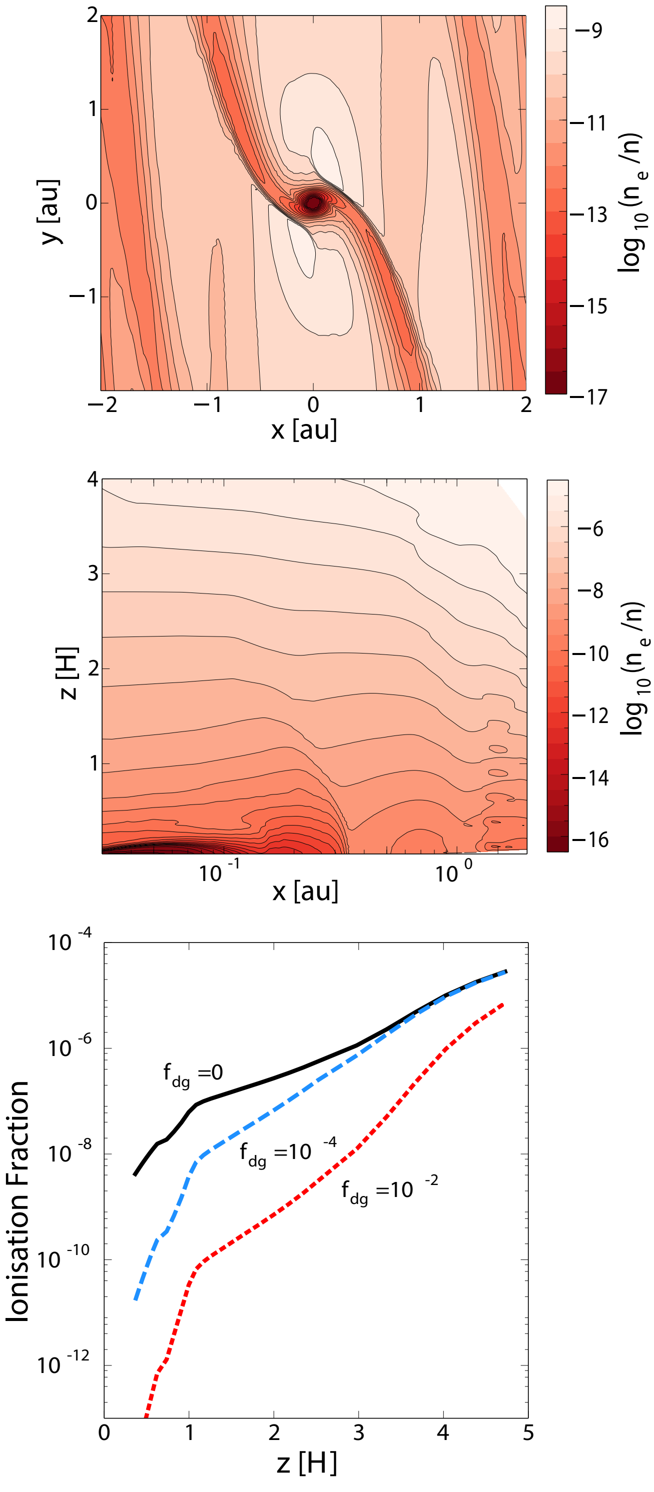

Figure 3.1: Ionisation fraction profile slices through the gap, a posteriori computed for the hydrodynamical simulation of Tanigawa, Ohtsuki & Machida (2012). Top and centre panels show 2D slices of the ionisation fraction $\log_{10}(n_e/n)$ as contour plots with logarithmically-spaced contours for $y = 0$ and $z = 0$, respectively, and for $f_{dg} = 10^{-4}$. Bottom panel shows n_e/n as a function of height for $x = 0.3\,\mathrm{au}, y = 0$ for dust-to-gas mass ratios $f_{dg} = 0, 10^{-4}, 10^{-2}$ with solid, dashed, and dotted curves respectively.

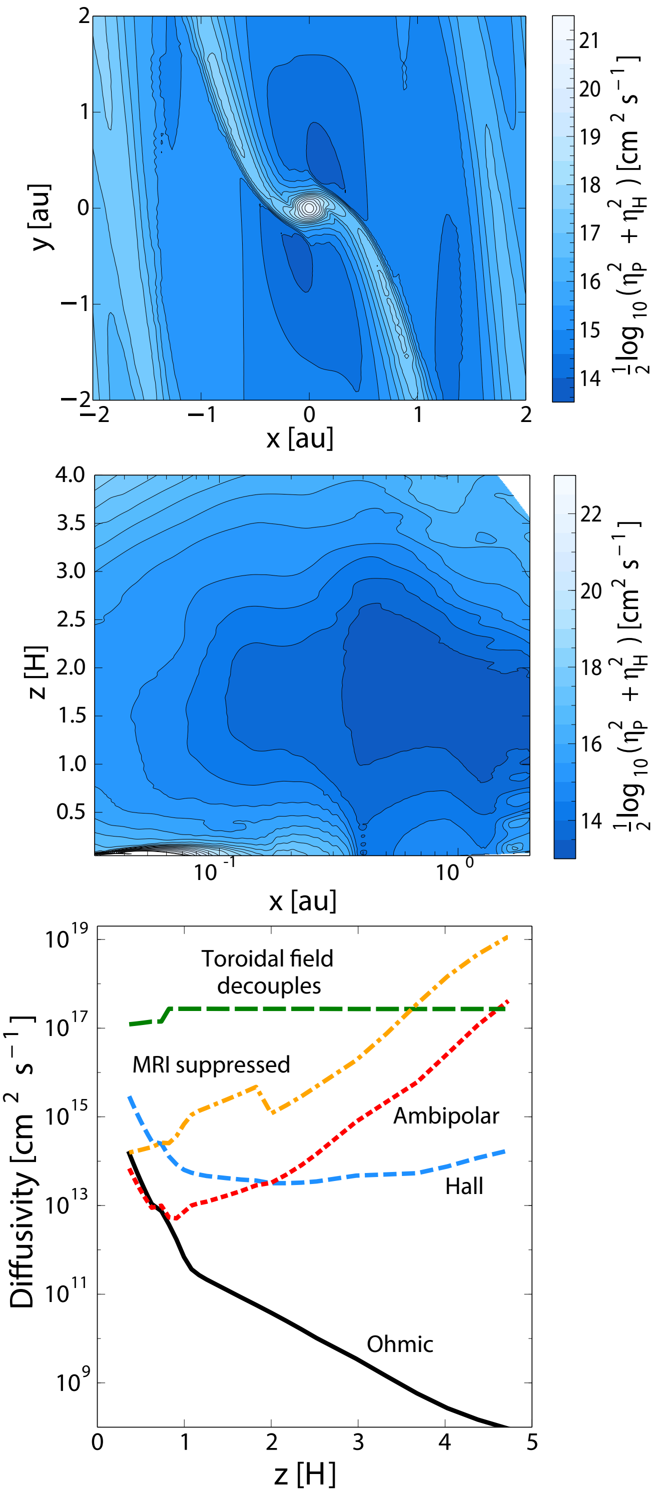

Figure 3.2: As for Figure 3.1 but showing a contour plot of the field-perpendicular diffusivity, $\eta_\perp = \sqrt{\eta_P^2 + \eta_H^2}$ at the midplane (top panel), and $y = 0$ (centre panel). Ohmic resistivity (solid curve), Hall drift (dashed curve), and ambipolar diffusion (dotted curve) are also shown as functions of height at $x = 0.3\,\text{au}$, $y = 0$ (bottom panel). The long-dashed and dot-dashed curves show the coupling thresholds for toroidal and MRI fields, ΩH^2 and $v_{a,z}^2\Omega^{-1}$, respectively.

lower-left of the circumplanetary disc. It decreases with height in keeping with the exponential density profile. Hall drift is relatively constant with height above the midplane and dominates up to $z = 2.5\,H_p$. Ambipolar diffusion is strongest in the low density atmosphere where neutrals are too sparse to influence electron and ion motion.

Non-ideal effects are orders of magnitude below the level at which the toroidal field decouples, except in the circumplanetary disc. Here the field is uncoupled to the midplane gas flow, but is anchored to, and transported by, gas in the overlying coupled region.

Non-ideal effects are below the MRI suppression threshold in the disc atmosphere, $z \gtrsim H_p$. The turbulent region is limited by the weak field condition [equation (3.13)], rather than diffusion. Magnetic pressure is weaker than gas pressure at $z \lesssim 2H_p$, and the field is weak enough to bend. The strong field region reaches towards the midplane near the planet where field enhancement from flux-conservation is greatest.

3.3.3 Magnetic field strength and geometry

Fig. 3.3 shows the magnetic field strength and geometry. The top panels are contour plots, in the top-down (top-left panel) and edge-on (top-right panel) views, with colour scale showing $\log_{10}(B)$, calculated for $s = 1$. The bottom-left panel shows vertical profiles for the poloidal, toroidal and turbulent magnetic field components evaluated at $x = 0.3\,\mathrm{au}, y = 0$. A turbulent field is only present in the active zone between $0.5 \lesssim z \lesssim 2\,H_p$ for $s = -1$ and for $z \lesssim 2\,H_p$ for $s = 1$. The bottom-right panel is an edge-on view of the gap, colour coded according to the dominant field component. The gap is divided into the following regions: (a) poloidal (yellow), (b) toroidal (green), and (c) MRI turbulent (blue) field. Orange, dark green, and dark blue regions indicate the corresponding regions where the Hall effect maintains coupling of the toroidal component, and so the field may be counter-wrapped when B_z is aligned with the rotation axis. Hatched blue regions are Hall-MRI unstable and so they are predominantly turbulent if $s = 1$, or predominantly toroidal if $s = -1$.

The field strength is relatively uniform in the gap but flux conservation enhances the field in the circumplanetary disc. A toroidal field would easily couple and permeate the gap, but is limited by magnetic pressure in the disc atmosphere, and so the field would be increasingly poloidal with height. The gap would be turbulent between $z \sim 0.5$–$2\,H_p$, except in the circumplanetary disc where the field is too strong. The Hall effect extends the turbulent region to the protoplanetary disc and circumplanetary disc midplanes if $s = 1$, however the midplanes are MRI stable if

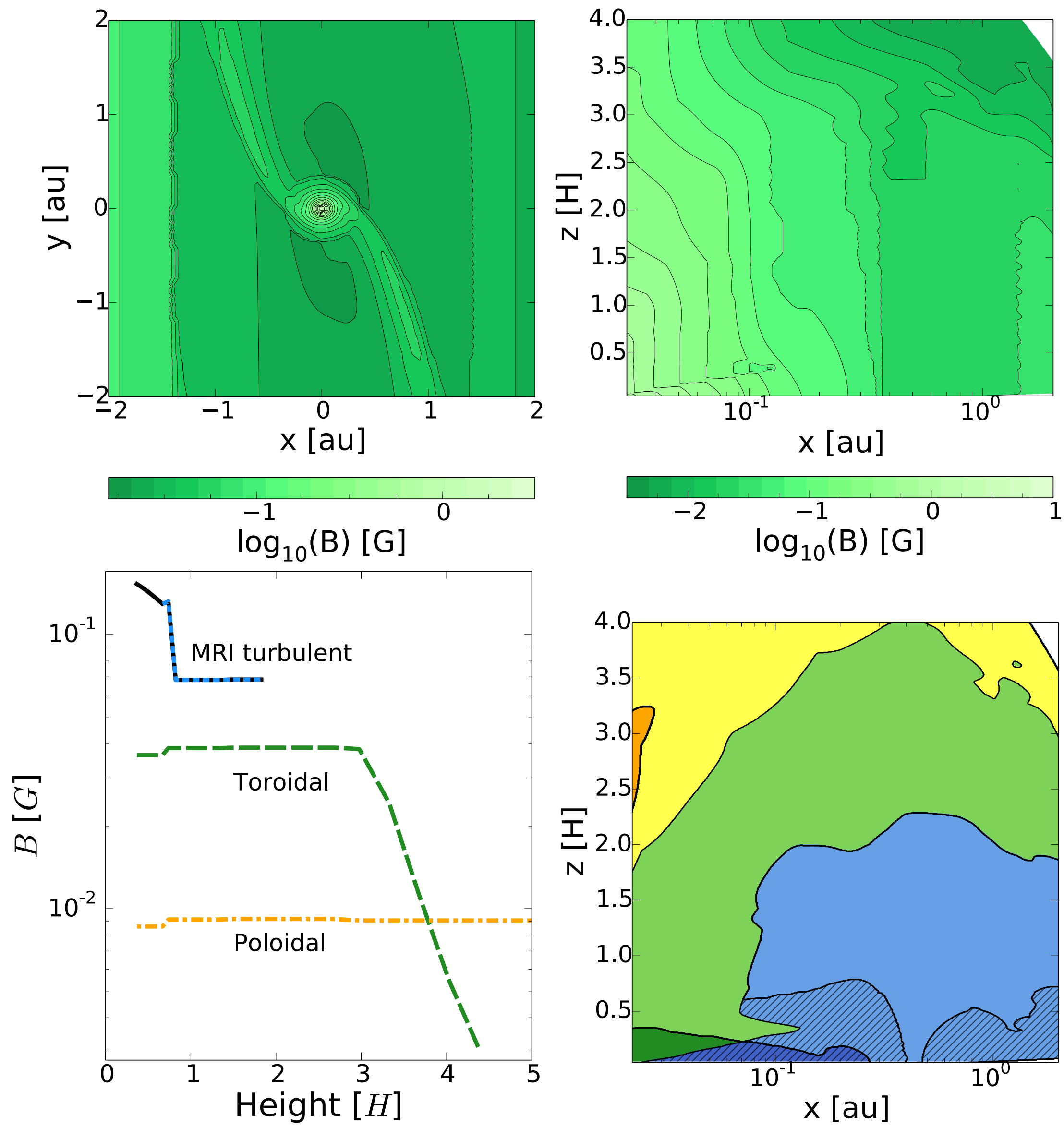

Figure 3.3: Properties of the estimated magnetic field in the gap for the standard parameter set $f_{dg} = 10^{-4}$, $f_\Sigma = 1$, $f_B = 1$. Top-left and -right panels show contour plots of the field strength, B, at the midplane and $y = 0$, respectively. Bottom-left panel shows the vertical profile of field components at $x = 0.3\,\mathrm{au}$, $y = 0$. The vertical, toroidal, MRI field with $s = 1$, and MRI field with $s = -1$ are shown as the dot-dashed, dashed, solid, and dotted curves respectively. Bottom-right panel shows the edge-on view of the field geometry, colour-coded according to the dominant field component for $s = 1$: (a) poloidal field (yellow), (b) toroidal field (green), and (c) MRI turbulent field (blue). Orange, dark green, and dark blue regions indicate where the Hall effect sustains and influences the toroidal field. Hatched MRI unstable regions show where Hall effect dominates, so that the field is predominantly turbulent if $s = 1$, and toroidal if $s = -1$.

$s = -1$. The upper boundary of the turbulent zone is limited by the weak field requirement, rather than non-ideal effects.

Fig. 3.4 shows the effect of varying parameters on the field geometry: $f_{dg} = 0$, 10^{-2} (top- and bottom-left panels), $f_\Sigma = 0.1$, 10 (top-and bottom-centre panels), and $f_B = 0.1$, 10 (top- and bottom-right panels). In general, we find that the gap is either predominantly toroidal, ideal MRI, or Hall-MRI unstable. The upper MRI boundary only depends on β_z through the column density and magnetic field strength, whereas the boundary of the Hall-MRI layer is controlled by the height at which the Hall drift exceeds the MRI threshold, $\Omega v_{a,z}^{-2}$. Thus, the Hall-MRI region extends by lowering the ionisation fraction, caused either through enhanced surface density attenuating ionising radiation (e.g., for $f_\Sigma > 1$), or by grains soaking up free electrons (e.g., for $f_{dg} = 10^{-2}$). Lowering the magnetic field strength reduces the Alfvén speed, and consequently lowers the MRI threshold to below the Hall drift (e.g., for $f_B < 1$).

On the other hand, the circumplanetary disc may host a wide range of conditions. Here the Hall-MRI zone in the circumplanetary disc is resilient to changes in f_{dg}, but recedes if β_z increases through enhanced density or reduce field strength, so that the field is predominantly toroidal. The field would be predominantly poloidal if Ohmic resistivity exceeds Hall drift, either by enhanced resistivity through higher density, or reduced Hall electromotive force (EMF) from a lower field strength. However, further analysis into the potential for MRI turbulence in the circumplanetary disc will rely on models which are not affected by numerical viscosity.

3.4 Implications for MHD gap modelling

In this section we consider the implications of including non-ideal effects in MHD modelling of gas flow. We determine the extent to which magnetic diffusion limits small-scale field gradients to calculate the minimum field bending radius. We discuss the implications of diffusion-limited field bending on the resolution needed for simulations. We also estimate the strength of large-scale magnetic forces, to compare with the hydrodynamical forces included in the TOM12 simulation. This allows us to determine where, if at all, magnetic forces have the most influence on gas flow.

3.4.1 Minimum field-gradient length-scale

Non-ideal effects, particularly Ohmic resistivity and ambipolar diffusion, can wash out magnetic field gradients and limit the field bending length-scale, L_B. Here we calculate the smallest length-scale that the field can bend on, $L_{\min}$, given the level

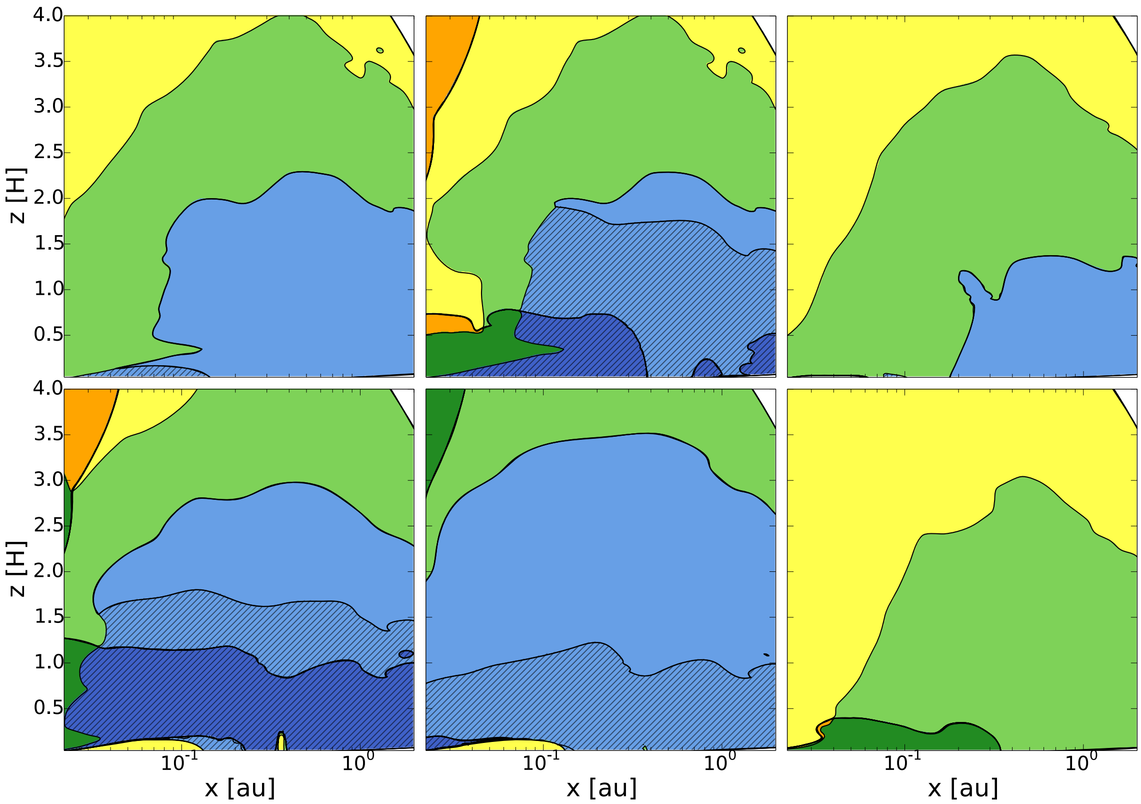

Figure 3.4: Same as bottom-right panel in Fig. 3.3, (i.e., $f_{dg} = 10^{-4}$, $f_\Sigma = 1$, $f_B = 1$), except varying the dust-to-gas mass ratio $f_{dg} = 0, 10^{-2}$ (top- and bottom-left panels, respectively), column density enhancement factor $f_\Sigma = 0.1, 10$ (top-and bottom-centre panels, respectively), and magnetic field enhancement factor $f_B = 0.1, 10$ (top- and bottom-right panels, respectively).

of magnetic resistivity and diffusion throughout the gap as calculated in §3.3.2. The impact of Hall drift on magnetic field gradients is highly uncertain, being able to enhance or resist gradients. Therefore we neglect its effect in this simple calculation, but note the potential key impact it can have on the large-scale structure we consider here.

Just as equations (3.12), (3.14), (3.15) specify the maximum diffusivity which permits the gradients needed for a turbulent or toroidal field, we can invert this relationship to specify the minimum bending length-scale given the magnetic diffusivity. This is applicable to large-scale, quasi-static magnetic field structures (as opposed to rapidly fluctuating turbulence), for which magnetic induction is balanced by magnetic diffusion. We derive the relation between magnetic diffusion and a general field geometry using the induction equation [equation (3.11)]. Although it is generally necessary to treat each component of the induction equation separately, we can estimate the diffusion limit for the minimum gradient length-scale,

$$\eta_P < vL_B \left(\frac{L_B^{-1} + L_v^{-1}}{L_B^{-1} + L_\eta^{-1}} \right). \tag{3.27}$$

We calculate the velocity and diffusivity gradient length-scales, L_v, and L_η, using

$$L_f = f/|\nabla f|, \tag{3.28}$$

with f set to the relevant fluid velocity or Pedersen diffusivity, respectively. Note that as we use the velocity in the frame orbiting with the planet to calculate L_v, we remove the Keplerian component with respect to the star, which acts as a large constant offset in equation (3.28).

We invert equation (3.27) to determine the *minimum* field gradient length-scale $L_{\min}$:

$$L_{\min} = \frac{2\eta_P}{v} \left[1 - \frac{\eta}{vL_\eta} + \sqrt{\left(1 - \frac{\eta}{vL_\eta}\right)^2 + \frac{4\eta}{vL_v}} \right]^{-1}. \tag{3.29}$$

Figure 3.5 shows a contour plot of $\log_{10}(L_{\min}/\mathrm{au})$ at $y = 0$, with logarithmically-spaced contour level. The minimum field bending length-scale follows $L_{\min} \propto \eta_P/v$ everywhere except the circumplanetary disc where the η_P is large and L_v, L_η are small. It increases toward the planet, and is smallest at $z \sim H_p$ in the protoplanetary disc where the diffusivity is lowest.

This can be used to gauge the minimum resolution required for MHD simulations. For example, as the minimum field bending length scale is large in the circumplanetary disc, the resolution is determined by velocity and pressure gradients length-scales instead. In the protoplanetary disc, significantly higher resolution is needed to resolve turbulence which can be tangled on a very small length-scales. The Hall effect can pose an additional challenge to simulations as it is dissipationless and so can introduce small-scale field structure (e.g. Sano & Stone, 2002, Kunz & Lesur, 2013; Lesur, Kunz & Fromang, 2014; O'Keeffe & Downes, 2014; Bai, 2015).

3.4.2 Relative strength of magnetic forces

Large-scale magnetic fields have the potential to influence gas dynamics, rather than being merely passively drawn along with the gas. We touched on this in §3.2.4 when we compared the toroidal component of magnetic pressure with gas pressure.

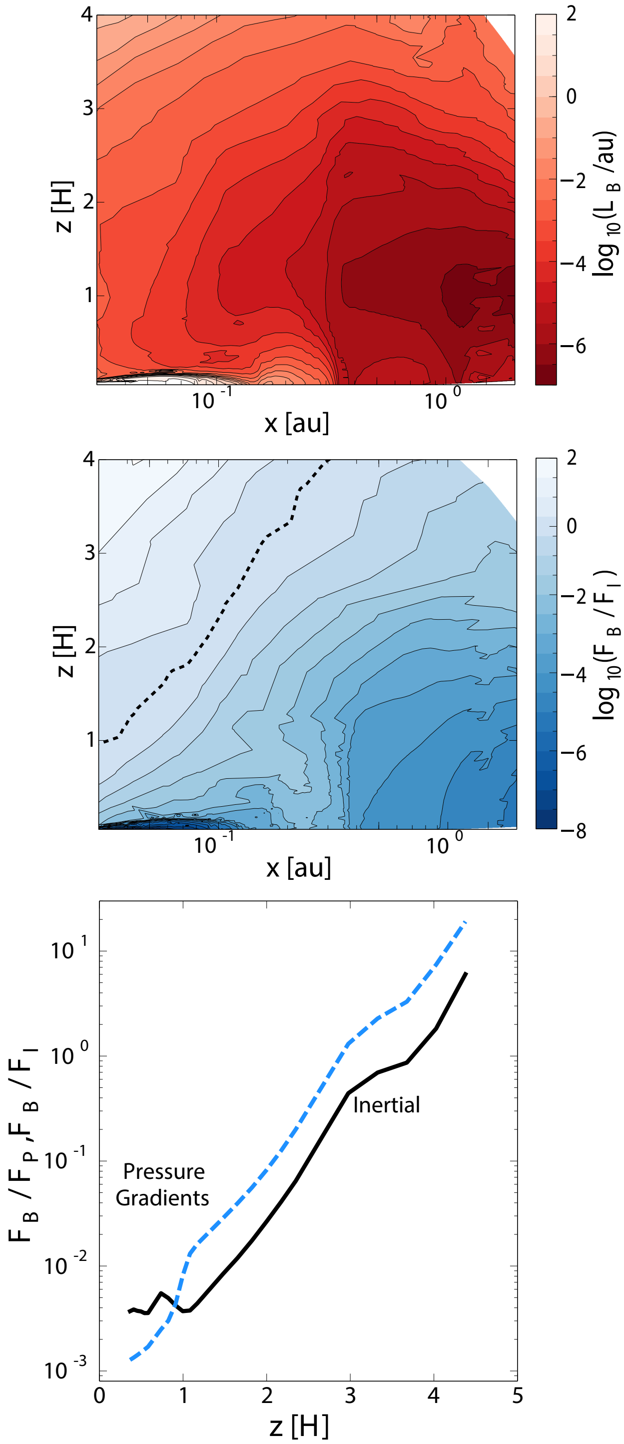

Figure 3.5: Top panel shows contours of the minimum field bending-scale, $L_{\rm min}$, shown in the edge-on view at $y = 0$. Centre and bottom panels shows the strength of magnetic forces relative to hydrodynamical forces. The centre panel shows the logarithm of the ratio of the magnetic force to the inertial force, $\log_{10}(F_B/F_I)$ at $y = 0$. The dashed contour shows the location of $F_B = F_I$. The bottom panel shows vertical profiles of $\log_{10}(F_B/F_I)$ and $\log_{10}(F_B/F_P)$, the logarithm of the ratio of the magnetic force to the inertial and pressure gradient forces at $x = 0.3\,$au, $y = 0$ as the solid and dashed curves, respectively.

For example, circumplanetary jets have been launched in ideal and resistive MHD simulations (Machida, Inutsuka & Matsumoto, 2006; Gressel et al., 2013).

The TOM12 simulation is not magnetised; nevertheless we can estimate the size of magnetic forces and compare them with hydrodynamic forces in the simulation. This will indicate where, if at all, they have the greatest potential to alter the balance of forces and so influence the gas flow. It also acts as a consistency check, validating (or otherwise) our adoption of a hydrodynamic simulation as the underlying model.

The full momentum equation, including both hydrodynamic and magnetic forces is

$$\begin{aligned}\frac{1}{\rho}\frac{\partial \mathbf{v}}{\partial t} + (\mathbf{v}\cdot\nabla)\,\mathbf{v} &= -2\Omega_p\hat{\mathbf{z}}\times\mathbf{v} - \Omega_p^2\hat{\mathbf{z}}\times(\hat{\mathbf{z}}\times\mathbf{r}) - \nabla\Phi \\ &\quad -\frac{1}{\rho}\nabla p + \frac{1}{4\pi\rho}(\nabla\times\mathbf{B})\times\mathbf{B}, \end{aligned} \tag{3.30}$$

where $\mathbf{r} = (x, y, z)$ and Φ is the combined gravitational potential from the star and planet:

$$\Phi = -\frac{GM_*}{|\mathbf{r}-\mathbf{r}_*|} - \frac{GM_p}{|\mathbf{r}|}. \tag{3.31}$$

The hydrodynamic terms in equation (3.30) are the time derivative and inertial force on the left hand side, and the Coriolis, centrifugal force, gravitational, and pressure gradient force on the right hand side. These are calculated in the frame co-orbiting with the protoplanet in the TOM12 simulation. We neglect the time derivative because it is small, with the simulation in almost steady state.

The addition of a magnetic force [the final term on the right hand side of equation (3.30)] will inevitably change the balance of forces, however the impact will be negligible unless the magnetic force is strong compared to the inertial force. We calculated the inertial force $F_I = |(\mathbf{v}\cdot\nabla)\,\mathbf{v}|$ and its associated gradient length scale

$$L_I = \frac{\mathbf{v}^2}{|(\mathbf{v}\cdot\nabla)\,\mathbf{v}|}, \tag{3.32}$$

from the TOM12 simulation, using second-order finite differencing, with good convergence compared with first-order differencing.

We estimate the magnetic force from large-scale, non-turbulent fields using,

$$F_B \equiv \frac{1}{4\pi\rho}|(\nabla\times\mathbf{B})\times\mathbf{B}| \sim \frac{v_a^2}{L_B}. \tag{3.33}$$

We do this by using the Alfvén speed calculated for the total, non-turbulent field strength. Our magnetic force estimate relies on a knowledge of the field gradient length-scale, L_B. We expect that, in general, L_B traces the fluid gradient length-scales because either the field is dragged along with the fluid or visa versa. If this is the case, we take $L_B = L_I$, and it cancels from the ratio of the magnetic and hydrodynamic forces F_B/F_I. If, instead, the gas varies over a shorter length-scale than diffusion permits the field to bend, we take $L_B = L_{\rm min}$ as calculated in §3.4.1. In this way, we compare the magnetic force over the same scale as the hydrodynamic forces, to the extent that diffusion permits. We have not included the force arising from effective MRI turbulent viscosity, as it is already the subject of extensive study within the literature (see Turner et al., 2014).

We also consider the effect magnetic forces have on the scale height by comparing them with the pressure gradient force, $F_P = |(\nabla p)/\rho|$, with length-scale L_P calculated using equation (3.28).

The centre panel of Fig. 3.5 shows a contour plot of the logarithm of the ratio of the magnetic force to the inertial force, $\log_{10}(F_B/F_I)$ at $y = 0$. The dashed contour denotes $F_I = F_B$. The bottom panel shows the vertical profile of the ratio of the magnetic force to the inertial, and pressure gradient forces. Magnetic forces are strongest in the atmosphere, exceeding the inertial and pressure gradient forces above $z \gtrsim$ 2.5–3.5 H_p, where they are able to influence the protoplanetary disc scale-height.

Magnetic forces are weakest in the circumplanetary disc where strong magnetic diffusion limits the field bending length scale to the diffusion length-scale. Although artificial diffusion lessens the reliability of the circumplanetary disc structure in the TOM12 simulation, our study in Chapter 2 shows that magnetic diffusion is strong across a range of circumplanetary disc models, owing to the column high density shielding the disc from external ionising radiation. The strong diffusion increases the minimum field bending length scale, thereby reducing the magnetic force. This indicates that large-scale magnetic forces cannot yield any significant accretion in the circumplanetary disc, which must come from the MRI or gravitational instability-MRI limit-cycles (e.g., Martin & Lubow, 2011a; Lubow & Martin, 2012).

3.5 Discussion

In this study we examined the importance of non-ideal effects in determining the magnetic field structure in a gap surrounding a giant protoplanet. We modelled the gap using a snapshot from the pure-hydrodynamical gap-crossing simulation by Tanigawa, Ohtsuki & Machida (2012). Our approach was to use this snapshot as a basis to a posteriori estimate key MHD quantities semi-analytically, which would otherwise be very challenging to incorporate into simulations. We calculated the ionisation fraction produced by cosmic-rays, stellar X-rays and radioactive decay, including the effect of grains. We calculated Ohmic resistivity, ambipolar diffusion and Hall drift to determine whether an MRI field could be generated and if a toroidal field could couple to the gas flow. We estimated the magnetic field strength in the protoplanetary disc from inferred accretion rates, and determined the gap field strength from flux-freezing.

We found that a magnetic field would be easily drawn from the protoplanetary disc into the gap and circumplanetary disc. A toroidal field permeates the gap, but is weakened by expansion from magnetic pressure above $z > 2$–$3\,H_p$. The gap is MRI unstable at $z > 0.5\,H_p$ with turbulence extending down to the midplane if the vertical component of the magnetic field is along the rotation axis (i.e., if $s = 1$). However, if the vertical field and rotation axis are anti-aligned, the conditionally unstable regions are non-turbulent. As protoplanetary discs exhibit a range of field/rotation axis misalignment angles we expect the size of the MRI turbulent region to differ between systems, with significant implications for the flow dynamics (Hull et al., 2013; Krumholz, Crutcher & Hull, 2013).

This direction dependence of the MRI originates with the Hall effect. The Hall effect is strong below $z < 2\,H_p$ and plays an important role in generating MRI instability. We found that it can also facilitate coupling of a toroidal field, despite strong magnetic Pedersen diffusion, and influences the orientation of the toroidal component. This may lead to counter-wrapping of the toroidal field if $s = 1$, where the field drift opposes the Keplerian gas flow. Further simulations are needed to probe the role of the Hall effect in this system.

By testing the sensitivity of the calculations to dust content, column density, and magnetic field strength, we found that gaps are generally susceptible to the Hall- or ideal-MRI. On the other hand, the MRI in the circumplanetary disc may be quite sensitive to disc conditions and could have a turbulent, toroidal or vertical field. As the circumplanetary disc evolves, the disc may experience a range of different field configurations in keeping with the varying column density and dust content. Understanding the evolution of a circumplanetary disc is key for satellite formation studies, which is believed to be the formation site of moons. Bimodality in circumplanetary disc dynamics caused by the Hall effect may transfer to the growth of moons within the system. For example, turbulent heating will affect the location of the circumplanetary ice-line.

Finally, we have calculated the minimum magnetic field gradient length-scale limited by magnetic diffusion. Magnetic diffusion resists field gradients, and so minimal field bending is permitted in the circumplanetary disc where Ohmic resistivity is strong. We find that large-scale (non-turbulent) magnetic forces are unable to drive accretion in circumplanetary discs. Turbulence aside, we found the large scale-flow features are well modelled by a hydrodynamical fluid as large scale magnetic forces as small outside the protoplanetary disc atmosphere. Here, magnetic coupling is good and so a strong field may be able to produce a jet, winds, or other variability.

In summary, we find that the magnetic field surrounding a giant protoplanet is mostly toroidal, with large bands of ideal- and Hall-MRI turbulent zones. The magnetic field geometry is dependent on the orientation of the vertical field component, established during the collapse of the protostellar core. Non-ideal effects are important in the gap and need to be included in future MHD simulations of gap crossing.

4

Structure and stability of magnetically-braked accretion discs

4.1 Introduction

Accretion flow is fundamental in governing the structure and dynamics of protoplanetary discs. It is a hallmark of the T Tauri phase ($\dot{M} \sim 10^{-13}$–$10^{-7}\,M_{\odot}$/year; see references in Zhou et al., 2014), with wide-ranging implications for planet formation. Grain growth (Youdin & Goodman, 2005; Rice et al., 2004; Lorén-Aguilar & Bate, 2015), core growth and envelope capture (Okuzumi & Ormel, 2013; Ormel & Okuzumi, 2013), and planet migration (Lin & Papaloizou, 1986; Ward, 1997) are all sensitive to accretion processes at work in the disc.

A small but significant subset of young stellar objects show considerable excess infrared and ultraviolet luminosity variability, interpreted as a changing accretion supply from the circumstellar disc. FU Ori is the archetypal eruptive T Tauri star, characterised by a rapid (rise time $\sim$ 1–10 years) 100 fold increase in the optical luminosity originating in the inner 1 au of the disc (Herbig, 1977; Zhu et al., 2007). The outburst luminosity decays slowly, over a period of years to decades, back to the pre-eruptive level [e.g., V1515 Cygni (Clarke et al., 2005), and V900 Mon (Reipurth, Aspin & Herbig, 2012)]. Objects like Ex Lupis exhibit smaller, repeated accretion-bursts lasting several months at a time (Herbig, 1977). Such events may account for the Herbig Haro jets which show well defined knots. These presumably correspond to intermittent accretion bursts punctuating long phases of ordinary quiescent accretion in young stellar objects (Reipurth & Bally, 2001; Ioannidis & Froebrich, 2012).

Inherent disc instability is the likely origin of accretion outbursts. Disc instability has been successful in modelling outbursts in similar accretion disc systems (i.e., describing light curves of dwarf novae outbursts in binary systems; Meyer & Meyer-Hofmeister, 1981), and do not rely on an external, perturbing influence from another star (Bonnell & Bastien, 1992; Pfalzner, 2008; Forgan & Rice, 2010) or giant protoplanet (Lodato & Clarke, 2004; Clarke et al., 2005).

Candidate instabilities include the (i) thermal-viscous instability in which increasing H-scattering opacity with temperature can exceed radiative cooling, leading to a rapid temperature rise which triggers enhanced hydromagnetic transport (Pringle, 1981; Bell & Lin, 1994); (ii) accretion of fragments formed through gravitational instability (Vorobyov & Basu, 2015, 2005; Dunham & Vorobyov, 2012), and (iii) hybrid gravo-magneto limit-cycles in which a mismatch in the transport rate between the inner (MRI-unstable) and outer (gravitationally-unstable) disc leads to a pile up and subsequent enhanced turbulent transport (Armitage, Livio & Pringle, 2001; Zhu et al., 2009; Martin & Lubow, 2011a; Lubow & Martin, 2012; Bae et al., 2014; O'Keeffe & Downes, 2014).

Disc instability is related to the wider challenge of identifying the accretion mechanism. Magnetic fields are generally considered the most promising candidate for driving accretion in these discs. Provided that the disc is a good enough conductor, a magnetic field is able to interact with, and influence, the bulk neutral flow. The MRI has been studied extensively for its propensity to generate efficient, turbulent inflow from a weak initial field (Balbus & Hawley, 1991; Hawley, Gammie & Balbus, 1995). Strong evidence for an MRI-inactive zone in the critical planet formation region has renewed interest in accretion by large-scale fields (Gammie, 1996; see Armitage, 2011 for a review), such as magnetic braking (Matsumoto & Tomisaka, 2004; Braiding & Wardle, 2012) or disc winds (Blandford & Payne, 1982; Wardle & Königl, 1993).

In this chapter we construct a steady-state model of a thin, magnetically-braked accretion disc. We determine the radial structure using the axisymmetric, vertically-averaged MHD equations of Krasnopolsky & Königl (2002) [see also Braiding & Wardle 2012; Braiding 2011; §4.2 and §4.3]. Non-ideal MHD effects are included to provide the necessary field drift relative to the accreting fluid. We determined an approximate force-free model for the orientation of field lines at the outer surface of the disc to account for the tendency of strong fields to splay out (§4.4). Power-law, equilibrium solutions are presented in §4.5. We then perform a local, linear analysis of this system to determine the stability of axisymmetric, radial modes in §4.6. We conclude with a summary of the results and a discussion of the implications for protoplanetary disc accretion in §4.7.

4.2 Formulation

We begin by outlining the basic set-up and physical assumptions underlying our accretion disc model. The disc is described in cylindrical coordinates (r, ϕ, z) by a mass density ρ, velocity $\mathbf{v} = (v_r, v_\phi, v_z)$, and magnetic field $\mathbf{B} = (B_r, B_\phi, B_z)$. The evolution of the disc is governed by the continuity equation, momentum equation, Gauss' law for magnetism, and the induction equation,

$$\frac{\partial \rho}{\partial t} + \nabla \cdot (\rho \mathbf{v}) = 0, \tag{4.1}$$

$$\rho \frac{\partial \mathbf{v}}{\partial t} + \rho \left(\mathbf{v} \cdot \nabla\right) \mathbf{v} = \rho \mathbf{g} - \nabla p + \frac{1}{4\pi} \left(\nabla \times \mathbf{B}\right) \times \mathbf{B}, \tag{4.2}$$

$$\nabla \cdot \mathbf{B} = 0, \tag{4.3}$$

$$\frac{\partial \mathbf{B}}{\partial t} = -c \nabla \times \mathbf{E}, \tag{4.4}$$

where c is the speed of light, and $\mathbf{E}$ is the electric field.

The pressure

$$p = \rho c_s^2 \tag{4.5}$$

is related to the isothermal sound speed, $c_s = \sqrt{kT/m_n}$, where T is the temperature, k is Boltzmann's constant, and m_n is the mean molecular weight. We adopt a solar composition of 80 per cent molecular hydrogen and 20 percent atomic helium, giving a mean molecular weight of $m_n = 2.34 m_p$, where m_p is the mass of a proton. This corresponds to a sound speed of $c_s = 1\,\mathrm{km\,s^{-1}}\sqrt{T/280\,\mathrm{K}}$.

We consider a low-mass, thin disc for which the gravitational force of the central object of mass M, dominates over the disc's self-gravity. This produces a gravitational field

$$\mathbf{g} = \nabla \left[\frac{GM}{(r^2 + z^2)^{\frac{1}{2}}} \right]. \tag{4.6}$$

The magnetic field threading the disc emerges into a tenuous atmosphere, above and below the disc. The density is so low that magnetic forces dominate, and the field adjusts to a force-free configuration, i.e. $(\nabla \times \mathbf{B}) \times \mathbf{B} = 0$. The orientation of the field at the outer surface of the disc sets the boundary conditions for the field in the disc.

Magnetic braking by a massive cloud is adopted as the driver of accretion. The magnetic field emerges into a tenuous atmosphere above and below the disc, and connects to a massive, distant cloud, such as remnant material from the progenitor molecular cloud. The disc's rotation winds up the field, which transmits torques and deposits angular momentum into the cloud. As the cloud is massive it resists acceleration and pulls back on the field. The field transmits this back to the disc, decelerating the rotation and consequently brakes the disc. Magnetic braking produced in this way does not require an outflow so we set $v_z = 0$. Other braking mechanisms, such as torsional Alfvén waves (Krasnopolsky & Königl, 2002) or a disc wind (Blandford & Payne, 1982; Wardle & Königl, 1993), are also possible.

Magnetically-driven accretion relies on an interplay between gas flow and magnetic field. For example, perfect conduction freezes the magnetic field into the gas, so that the gas and field evolve together as a coupled system. However, in a partially ionised gas, collisions with neutral particles disrupt the $\mathbf{E} \times \mathbf{B}$ drift of electrons and ions relative to the magnetic field. A higher neutral particle density is needed to disrupt ions than electrons giving rise to three non-ideal regimes: Ohmic resistivity, Hall drift, and ambipolar diffusivity. These non-ideal effects, with associated transport coefficients η_O, η_H, η_A, appear in the induction equation though Ohm's law,

$$\mathbf{E} = -\mathbf{v} \times \mathbf{B} + \nabla \times [\eta_O(\nabla \times \mathbf{B}) + \eta_H(\nabla \times \mathbf{B}) \times \hat{\mathbf{B}} + \eta_A(\nabla \times \mathbf{B})_\perp], \tag{4.7}$$

where the subscript $\perp$ refers to the orientation with respect to the local magnetic field.

Non-ideal effects are an essential ingredient of MHD accretion disc theory as they allow the field to slip through accreting gas, rather than being dragged inward toward the central object. On the other hand, if they are too strong they may suppress magnetically-driven accretion. These effects are only important if the ionisation fraction is very low (ionisation fraction $\lesssim 10^{-13}$; Balbus & Hawley, 2000), but it appears that this encompasses most of a protoplanetary disc [for a review, see Armitage (2011)]. In fact, it is likely that non-ideal effects confine magnetically-accreting regions to surface layers ionised by high-energy incident radiation and the thermally ionised inner disc (Gammie, 1996).

In this first pass at the calculation we simplify the analysis by using an approximate model for non-ideal effects. We assume that accretion occurs through ionised surface layers and parametrise the transport coefficients rather than calculating them exactly (see §4.5).

4.3 Vertically integrated disc

Using cylindrical coordinates, under the assumption of axisymmetry, equations (4.1)–(4.3), and the vertical components of equation (4.4) are given by

$$\frac{\partial \rho}{\partial t} + \frac{1}{r}\frac{\partial}{\partial r}(r\rho v_r) = 0, \tag{4.8}$$

$$\rho\frac{\partial v_r}{\partial t} + \rho v_r\frac{\partial v_r}{\partial r} - \rho g_r + c_s^2\frac{\partial \rho}{\partial r} - \rho\frac{v_\phi^2}{r} - \frac{B_z}{4\pi}\frac{\partial B_r}{\partial z} + \frac{\partial}{\partial r}\left(\frac{B_z^2}{8\pi}\right) + \frac{1}{8\pi r^2}\frac{\partial}{\partial r}(rB_\phi)^2 = 0, \tag{4.9}$$

$$\frac{\rho}{r}\frac{\partial}{\partial t}(rv_\phi) + \frac{\rho v_r}{r}\frac{\partial}{\partial r}(rv_\phi) - \frac{B_z}{4\pi}\frac{\partial B_\phi}{\partial z} - \frac{B_r}{4\pi r}\frac{\partial}{\partial r}(rB_\phi) = 0, \tag{4.10}$$

$$c_s^2\frac{\partial \rho}{\partial z} = \rho g_z - \frac{\partial}{\partial z}\left(\frac{B_\phi^2}{8\pi} + \frac{B_r^2}{8\pi}\right) + \frac{B_r}{4\pi}\frac{\partial B_z}{\partial r}, \tag{4.11}$$

$$\frac{\partial B_z}{\partial z} + \frac{1}{r}\frac{\partial (rB_r)}{\partial r} = 0, \tag{4.12}$$

and

$$\begin{aligned} r\frac{\partial B_z}{\partial t} &+ \frac{\partial}{\partial r}\left[rv_rB_z + r\eta_O\left(\frac{\partial B_r}{\partial z} - \frac{\partial B_z}{\partial r}\right)\right] + \frac{\partial}{\partial r}\left(r\frac{\eta_H}{B}\left[\frac{B_r}{r}\frac{\partial}{\partial r}(rB_\phi) + B_z\frac{\partial B_\phi}{\partial z}\right]\right) \\ &+ \frac{\partial}{\partial r}\left\{r\frac{\eta_A}{B^2}\left[B_rB_\phi\frac{\partial B_\phi}{\partial z} - \frac{B_\phi B_z}{r}\frac{\partial (rB_\phi)}{\partial r} - \left(B_r^2 + B_z^2\right)\left(\frac{\partial B_r}{\partial z} - \frac{\partial B_z}{\partial r}\right)\right]\right\} = 0, \end{aligned} \tag{4.13}$$

where $B = \sqrt{B_r^2 + B_\phi^2 + B_z^2}$ is the total field strength.

To simplify the analysis, we construct a 1D model of the radial structure (Lubow, Papaloizou & Pringle, 1994). This involves integrating the MHD equations vertically through the disc to form height-averages of disc quantities. We follow the method given in Krasnopolsky & Königl (2002), and described in detail in Braiding (2011), to perform the integration. We give a brief summary of this procedure below.

As far as possible, we have tried to avoid assuming explicit functional forms for vertical profiles by estimating gradients and using the thin-disc approximation to discard negligible terms. We solve the equation up to first order in the aspect ratio, so $1 + \mathcal{O}(H/r) \approx 1$. Disc properties vary much more gradually in the radial direction than the vertical direction in a thin disc. Approximating gradients with radial and vertical gradient length-scales (i.e., r and H, respectively) makes clear which terms are of $\mathcal{O}(H/r)$, and are therefore negligible.

We extend this to cross-compare terms involving B_r and B_z. Assuming the poloidal components satisfy (Wardle & Königl, 1993)

$$B_r \gg \frac{H}{r} B_z, \text{ and } B_z \gg \frac{H}{r} B_r, \tag{4.14}$$

we may discard terms such as B_r/r and B_z/r as being small compared to B_r/H and B_z/H. We confirm the validity of this assumption by post-calculating $HB_r/(rB_z)$ and $HB_z/(rB_r)$, and find that they are, indeed, negligible. We do not apply the corresponding assumptions to the azimuthal magnetic field as the field may be so tightly wound that the azimuthal component exceeds the poloidal components.

For example, we can apply this approximation to the solenoidal condition, equation (4.12). The radial derivative of B_r is of $\mathcal{O}(H/r)$ relative to the vertical variation of B_z, and so, to first order, B_z is constant in height (Lovelace, Romanova & Newman, 1994).

Symmetries are used to re-express integrals through full vertical extent of the disc as an integral extending upwards from the midplane. The density, velocities and vertical field component have an even symmetry, whereas radial and azimuthal magnetic field components are antisymmetric. When integrating magnetic terms, we adopt a linear vertical profile for B_r and B_ϕ. This is the simplest function satisfying the symmetry requirement (e.g., Lubow, Papaloizou & Pringle 1994):

$$B_r(r,z) = B_{rs}(r)\left(\frac{z}{H(r)}\right), \tag{4.15}$$

$$B_\phi(r,z) = B_{\phi s}(r)\left(\frac{z}{H(r)}\right). \tag{4.16}$$

As integration removes any z dependence in disc properties, we will not need to refer to $B_r(r,z)$ and $B_\phi(r,z)$ again. To simplify the equations we drop the subscript 's' and rename $B_{rs}(r)$ and $B_{\phi s}(r)$ to B_r and B_ϕ in what follows.

The remaining terms are represented by their typical values in a density-averaged sense. Although this is not formally defined, the approximated set of equations we obtain is sufficient for our analysis.

Implementing this, the continuity equation and angular momentum equations integrate to:

$$\frac{\partial \Sigma}{\partial t} + \frac{1}{r}\frac{\partial}{\partial r}(r\Sigma v_r) = 0, \tag{4.17}$$

$$\Sigma\frac{\partial v_r}{\partial t}+\Sigma v_r\frac{\partial v_r}{\partial r}-\Sigma g_r+c_s^2\frac{\partial\Sigma}{\partial r}-\Sigma\frac{v_\phi^2}{r}-\frac{B_zB_r}{2\pi}+\frac{H}{12\pi r^2}\frac{\partial}{\partial r}(r^2B_\phi^2)-\frac{1}{6\pi}B_\phi^2\left(\frac{dH}{dr}\right)=0, \tag{4.18}$$

$$\frac{\partial(rv_\phi)}{\partial t}+v_r\frac{\partial(rv_\phi)}{\partial r}=\frac{rB_zB_\phi}{2\pi\Sigma}, \tag{4.19}$$

which are equivalent to equations (A5), (A9), and (A11) in Krasnopolsky & Königl (2002). The vertically averaged condition of hydrostatic equilibrium can be written as

$$\frac{g_r\Sigma}{r}H^2-\frac{1}{8\pi}\left(B_r^2+B_\phi^2\right)H+\Sigma c_s^2=0. \tag{4.20}$$

This is equivalent to equation (7) in Krasnopolsky & Königl (2002), up to factors of order unity which we have dropped to match the standard definition $H=c_s/\Omega$ in the absence of magnetic fields.

The vertical component of the induction equation is the only component to survive integration. Recasting the magnetic field using the magnetic flux, Ψ,

$$B_z=\frac{1}{2\pi r}\frac{\partial\Psi}{\partial r}, \tag{4.21}$$

simplifies the integration significantly, giving:

$$\frac{H}{2\pi r}\frac{\partial\Psi}{\partial t}+Hv_rB_z+\eta_OB_r+\frac{\eta_H}{B}B_zB_\phi+\frac{\eta_A}{B^2}\left(\frac{1}{3}B_rB_\phi^2+\frac{1}{3}B_r^3+B_z^2B_r\right)=0. \tag{4.22}$$

This pair of relations are equivalent to equations (2.49) and (2.65) in Braiding (2011).

4.4 External magnetic field

We require one further relation to close our set of equations. The geometry of the external field at the outer surface of the disc provides the necessary boundary conditions for our model. In this section we calculate the field structure in the atmosphere to determine the orientation of the field lines at the disc surface (e.g. B_r/B_z). We seek a solution which matches to our power-law solution at the disc surface,

$$B_z=B_{z0}(r/r_0)^{-\frac{5}{4}}. \tag{4.23}$$

Gas density is so low in the atmosphere that magnetic forces dominate and the field adopts a force-free configuration satisfying

$$\mathbf{J}\times\mathbf{B}=0, \tag{4.24}$$

where the current density $\mathbf{J} = c(\nabla \times \mathbf{B})/4\pi$. Magnetic tension balances magnetic pressure in this geometry.

There are two classes of non-trivial solutions this equation; we can search for a current-free solution, where $\mathbf{J} \propto \nabla \times \mathbf{B} = 0$, or we can seek a more general solution for which the current is parallel to the field, $\mathbf{J} \,||\, \mathbf{B}$. The latter is preferred, as it allows for a non-trivial B_ϕ, but we found that determining an exact solution is exceptionally difficult. Instead we build up a solution, beginning with a current-free field configuration in §4.4.1 and then use it to develop an approximate force-free field configuration in §4.4.2.

Our analysis determining the current-free solution is identical to that of Guilet & Ogilvie (2014), but it is nevertheless instructive to include details of the calculation here.

4.4.1 Current-free field

A current-free magnetic field is a potential field, meaning that $\mathbf{B} = \nabla f$ for some function f. Gauss' law requires that the function satisfies $\nabla \cdot \mathbf{B} = \nabla^2 f = 0$, which is

$$\nabla^2 f = \frac{1}{R^2}\frac{\partial}{\partial R}\left(R^2\frac{\partial f}{\partial R}\right) + \frac{1}{R^2 \sin\theta}\frac{\partial}{\partial \theta}\left(\sin\theta\frac{\partial f}{\partial \theta}\right) = 0, \tag{4.25}$$

in spherical co-ordinates, (R, θ, ϕ). We solve this subject to the boundary conditions $B_\theta = B_r = 0$ at the pole, and that at the disc surface $B_\theta = -B_z$, as given in equation (4.23):

$$\frac{\partial f}{\partial \theta} = 0 \text{ at } \theta = 0, \text{ and} \tag{4.26}$$

$$-\frac{\partial f}{\partial \theta} = B_{z0}(R/r_0)^{-\frac{5}{4}} \text{ at } \theta = \pi/2. \tag{4.27}$$

Motivated by the boundary conditions, we seek a separable power-law solution $f = P(x)r^{1-p}$, where $x = \cos\theta$. Inserting this into equation (4.25) gives

$$(1 - x^2)\frac{d^2 P}{dx^2} - 2x\frac{dP}{dx} + (1 - p)(2 - p)P = 0. \tag{4.28}$$

The solution is a linear combination of Legendre polynomials of the first and second kind. The pole boundary condition prohibits any contribution from a Legendre polynomial of the second kind, whereas the boundary condition at the disc surface sets the normalisation,

$$f = \frac{B_{z0} r_0}{P'_{1-p}(0)} \left(\frac{r}{r_0}\right)^{1-p} P_{1-p}(\cos\theta). \tag{4.29}$$

The resulting magnetic field is

$$B_R = \frac{\partial f}{\partial R} = \frac{(1-p)B_0}{P'_{1-p}(0)} \left(\frac{R}{r_0}\right)^{-p} P_{1-p}(\cos\theta), \tag{4.30}$$

$$B_\theta = \frac{1}{R}\frac{\partial f}{\partial \theta} = -\frac{B_0}{P'_{1-p}(0)} \left(\frac{R}{r_0}\right)^{-p} \sin\theta P'_{1-p}(\cos\theta), \tag{4.31}$$

$$B_\phi = 0. \tag{4.32}$$

We are now in a position to determine the boundary condition at the disc surface. We specify this as the ratio of the radial and vertical field components,

$$\frac{B_r}{B_z} = \frac{B_R(\pi/2)}{-B_\theta(\pi/2)} \tag{4.33}$$

$$= (1-p)\frac{P_{1-p}(0)}{P'_{1-p}(0)} \tag{4.34}$$

$$= -\frac{\Gamma\left(\frac{p}{2}-\frac{1}{2}\right)\Gamma\left(1-\frac{p}{2}\right)}{\Gamma\left(\frac{p}{2}\right)\Gamma\left(\frac{1}{2}-\frac{p}{2}\right)}. \tag{4.35}$$

$$\approx 1.428 \text{ for } p = 5/4.$$

This was simplified using equations (8.756.1), (8.756.2), (8.334.3), and (8.331.1) in Gradshteyn & Ryzhik (2007).

Equation (4.35) gives simple functional form for the field geometry, and reproduces the tabulated values for $B_r/B_z (\equiv I_{p-1})$ given in Table 1 of Shu et al. (2007). The resulting profile for B_r/B_z as a function of power-law index, p, is shown as the black curve in Fig. 4.1.

4.4.2 Force-free field

A toroidal field is an essential component of our magnetic braking model. A current-free field is too restrictive as our assumption of axisymmetry then sets $B_\phi = 0$. Instead, we determine the relationship between external field components for the general case that the field is parallel to the induced current. This involves solving

$$(\nabla \times \mathbf{B}) \times \mathbf{B} = 0 \tag{4.36}$$

for the field in cylindrical coordinates (r, ϕ, z). As in the disc, we assume axisymmetry so that $\partial/\partial\phi = 0$.

Combining Gauss' law with the force-free condition yields a triplet of simultaneous equations:

$$\frac{1}{r}\frac{\partial}{\partial}(rB_r) + \frac{\partial B_z}{\partial z} = 0, \tag{4.37}$$

and

$$\frac{(\nabla \times B)_r}{B_r} = \frac{(\nabla \times B)_\phi}{B_\phi} = \frac{(\nabla \times B)_z}{B_z},$$

which expands to

$$-\frac{1}{B_r}\frac{\partial B_\phi}{\partial z} = \frac{1}{B_\phi}\left(\frac{\partial B_r}{\partial z} - \frac{\partial B_z}{\partial r}\right) = \frac{1}{rB_z}\frac{\partial}{\partial r}\left(rB_\phi\right). \tag{4.38}$$

We attempted to find an exact, separable, force-free solution, but we were unable to do so analytically or numerically.

Instead, we present an approximate solution for the field near the disc surface. We seek a relation for B_r/B_z similar to equation (4.35), accounting for the modification due to a toroidal field. To achieve this, we equate the azimuthal and vertical components of equation (4.38),

$$\frac{1}{B_\phi}\left(\frac{\partial B_r}{\partial z} - \frac{\partial B_z}{\partial r}\right) = \frac{1}{rB_z}\frac{\partial}{\partial r}\left(rB_\phi\right). \tag{4.39}$$

We only require a solution near the disc surface to connect with our disc equation set. As we have stipulated that the solution is a power-law near the disc surface, we can use the radial profile given in equation 4.23 to evaluate the radial derivatives. Applying this and rearranging gives

$$\frac{\partial B_r}{\partial z} = -\frac{pB_z}{r}\left[1 + \frac{(p-1)}{p}\left(\frac{B_\phi}{B_z}\right)^2\right], \tag{4.40}$$

We need to evaluate the vertical derivative to find a solution. Although we cannot evaluate the z-derivative exactly, we can estimate it in the limit of vanishing B_ϕ (i.e., the current-free case). In this case, the solution has vertical and radial gradients with a length-scale $\approx \sqrt{r^2 + z^2}$, which is r at the disc surface. Therefore, we can estimate this term as

$$\frac{\partial B_r}{\partial z} \approx A\frac{B_r}{r}, \tag{4.41}$$

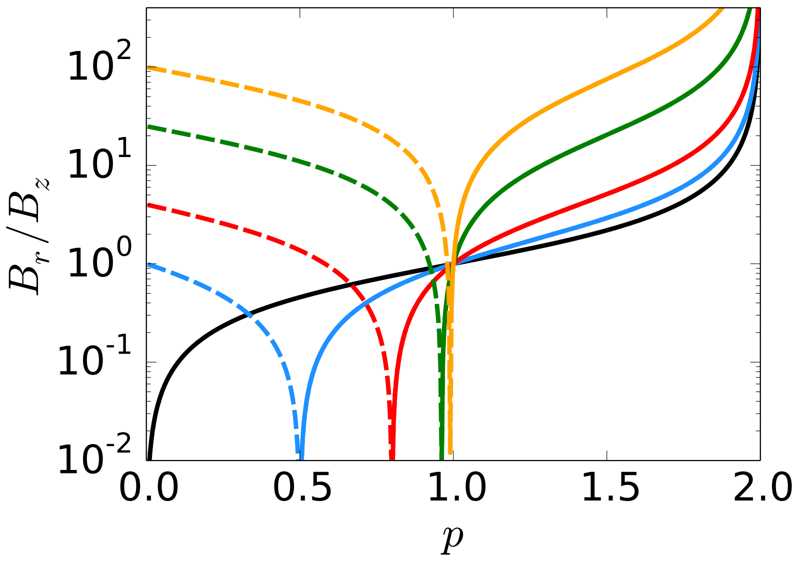

Figure 4.1: Ratio of the radial and vertical field components at the disc surface plotted against the radial power-law index of the magnetic field, p. The black, blue, red, green and orange curves correspond to $-B_\phi/B_z = 0$, 1, 2, 5, and 10, respectively. The dashed and solid curves correspond to portions of the graph which are negative and positive, respectively.

where A is an unknown constant. Inserting this into equation (4.40) gives

$$\frac{B_r}{B_z} = -\frac{p}{A}\left[1 + \frac{(p-1)}{p}\left(\frac{B_\phi}{B_z}\right)^2\right]. \tag{4.42}$$

We solve for A by ensuring that this relation reduces to the current-free case, equation (4.35), when $B_\phi = 0$. Thus, our estimate for the relationship between B_r/B_z is

$$\frac{B_r}{B_z} = -\frac{\Gamma\left(\frac{p}{2}-\frac{1}{2}\right)\Gamma\left(1-\frac{p}{2}\right)}{\Gamma\left(\frac{p}{2}\right)\Gamma\left(\frac{1}{2}-\frac{p}{2}\right)}\left[1 + \frac{(p-1)}{p}\left(\frac{B_\phi}{B_z}\right)^2\right]. \tag{4.43}$$

The behaviour of this relationship changes from $B_r \propto B_z$ for small B_ϕ, to $B_r \propto B_\phi^2/B_z$ for large B_ϕ. We find that B_r always exceeds B_ϕ and B_z for the power-law index $p = 5/4$, which we adopt throughout our analysis. The ratio B_ϕ/B_r is maximised at $B_\phi/B_z = \sqrt{p/(p-1)}$ with a value of $B_\phi/B_r = 0.78$ for $p = 5/4$.

The result is shown in Fig. 4.1 as a function of power-law index, p. Curves are shown for the current-free case (i.e., for $B_\phi/B_z = 0$), and $B_\phi/B_z = 1$, 2, 5, and 10. Only positive values of B_r/B_z (shown with a solid curve) correspond to the physical case of outward bending field lines. Therefore, a power-law index to the upward of the asymptote is negative, and unphysical. The effect of increasing the toroidal component is to increase $|B_r/B_z|$, and to move the asymptote to increasing p.

A toroidal field can substantially increase the inclination of magnetic field from the rotation axis. A poloidal field inclined at an angle 30° to the z-axis launches a magnetocentrifugal wind (Blandford & Payne, 1982), although the inclusion of a (strong) toroidal field may modify this criterion. It seems likely that strongly magnetised solutions may be susceptible to a wind, compromising our neglect of an outflow, although further analysis is needed to confirm this.

Unfortunately, the need for an approximate solution limits the validity of our equilibrium solution. This will impact disc properties we calculate, as this relation is part of a set of equations we solve simultaneously. More importantly, it will affect our stability analysis in §4.6, as the disc is not in exact equilibrium. Nevertheless, our approximate solution should perform well in regions where the toroidal component is much less than the poloidal components.

4.5 Equilibrium disc model

Having assembled our complete set of equations, equations (4.17)–(4.21), and (4.43), we are now in a position to compute the equilibrium structure of our disc.

4.5.1 Disc description

We search for a radial power-law solution characterised by a uniform inflow rate (i.e., $\partial\dot{M}/\partial r = 0$). This constrains the radial indices to: (i) velocities, $v_r, v_\phi, c_s \propto r^{-\frac{1}{2}}$, (ii) column density, $\Sigma \propto r^{-\frac{1}{2}}$, (iii) scale height $H \propto r$, (iv) magnetic field, $B_r, B_\phi, B_z \propto r^{-\frac{5}{4}}$ [the same scaling as the Blandford & Payne (1982) disc wind solution], and (v) non-ideal effects, $\eta_O, \eta_H, \eta_A \propto r^{\frac{1}{2}}$.

We use these scalings to evaluate radial derivatives, and set time derivatives to zero $\partial/\partial t = 0$. This forms a closed set of equations to solve for v_r, v_ϕ, H, B_r and B_ϕ:

$$\frac{v_r^2}{2r} + g_r + \frac{1}{2}\frac{c_s^2}{r} + \frac{v_\phi^2}{r} + \frac{1}{2\pi}\left(\frac{B_z^2}{\Sigma}\right)\frac{B_r}{B_z} + \frac{5H}{24\pi r}\left(\frac{B_z^2}{\Sigma}\right)\left(\frac{B_\phi}{B_z}\right)^2 = 0, \tag{4.44}$$

$$v_r v_\phi = \frac{r^2}{\pi}\left(\frac{B_z^2}{\Sigma}\right)\left(\frac{B_\phi}{B_z}\right), \tag{4.45}$$

$$\frac{g_r}{r}H^2 - \frac{1}{8\pi}\left[\left(\frac{B_r}{B_z}\right)^2 - \left(\frac{B_\phi}{B_z}\right)^2\right]\left(\frac{B_z^2}{\Sigma}\right)^2 H - c_s^2 = 0, \tag{4.46}$$

$$\frac{v_r}{c_s} + \frac{\left(\eta_O + \frac{1}{3}\eta_A\right)}{Hc_s}\frac{B_r}{B_z} + \frac{\eta_H}{Hc_s}\frac{B_\phi}{B_z}\left(\frac{B}{B_z}\right)^{-1} + \frac{\eta_A}{Hc_s}\frac{B_r}{B_z}\left(\frac{B}{B_z}\right)^{-2} = 0, \tag{4.47}$$

$$\frac{B_r}{B_z} = -\frac{\Gamma\left(\frac{p}{2}-\frac{1}{2}\right)\Gamma\left(1-\frac{p}{2}\right)}{\Gamma\left(\frac{p}{2}\right)\Gamma\left(\frac{1}{2}-\frac{p}{2}\right)}\left[1+\frac{(p-1)}{p}\left(\frac{B_\phi}{B_z}\right)^2\right]. \tag{4.48}$$

We compute the inflow rate using the continuity equation,

$$\dot{M} = 2\pi r v_r \Sigma. \tag{4.49}$$

Therefore, aside from constraining the power-law indices the continuity equation is an auxillary equation in our setup.

We solve these equations for v_r, v_ϕ, H, B_r and B_ϕ. Given a guess value for B_ϕ we calculate the chain B_r, H, v_r, v_ϕ using equations (4.48), (4.46), (4.47), and (4.44), respectively. Solutions for B_ϕ are those for which the trial for B_ϕ is the same as that computed using equation (4.45). We first locate the solutions approximately by searching for sign changes in the residual between the magnetic braking and inflow for an array of B_ϕ. We then hone in on the solution numerically using Powell's hybrid routine for root-finding, as detailed in §2.3.1, above.

Our choice to solve for v_r, v_ϕ, H, B_r and B_ϕ leaves us with needing to specify the following as parameters: mass of the central object, sound speed, vertical magnetic field strength, Ohmic, Hall and ambipolar transport coefficients, and column density.

Our model is suitable for accretion discs in general (e.g., discs around planets, black holes, etc.), but we give representative solutions appropriate to the proto-Solar nebula. Therefore, we consider a disc in orbit a Solar-mass central object $M = M_\odot$. The remaining parameters are specified for a normalisation orbital distance of $r = 1\,\mathrm{au}$.

We take the sound speed $c_s = 0.99\,\mathrm{km\,s^{-1}}$, corresponding to the temperature of a blackbody in thermal equilibrium with Solar-luminosity radiation ($T = 280\,\mathrm{K}$; Wardle, 2007). We also take $B_z = 1\,\mathrm{G}$ consistent with meteoritic estimates of the magnetic field strength in the solar nebula (Cisowski & Hood, 1991; although see Weiss et al., 2010).

We specify non-ideal effects in terms of a coupling threshold, which stipulates a maximum value for non-ideal effects so that they do not wash out field gradients. The coupling threshold depends on the gradient length-scale of the field. We use the coupling threshold for vertical gradients, $\eta \leqslant Hc_s$ as it is more stringent than the radial-gradient threshold by a factor of r/H [Wardle, 2007; see also equation (A.5)]. That is, if non-ideal effects are not so strong as to wash out magnetic field structure on a length-scale H then structure on a length-scale r will also be preserved.

Our approach is to parametrise non-ideal effects through the ratio of the transport coefficients, η_O, η_H, and η_A and coupling threshold, Hc_s. For example, we take $\eta_O/(Hc_s) = 0.1$, $\eta_H = \eta_A = 0$ as our standard parameter set. This choice of the Ohmic resistivity corresponds to 10% of the (de-)coupling threshold (Wardle, 2007). However, the transport coefficients could be calculated exactly if the ionisation fraction is known [e.g., using the expressions in equations (2.52)–(2.54); Pandey & Wardle, 2008)].

Ionisation in protoplanetary discs is primarily by external, high-energy radiation. Cosmic rays and X-rays ionise the disc surfaces to an attenuation depth of $\Sigma_{\rm CR} = 96\,{\rm g\,m^{-2}}$, and $\Sigma_{\rm XR} = 8\,{\rm g\,m^{-2}}$, respectively (Umebayashi & Nakano, 1981; Igea & Glassgold, 1999; Umebayashi & Nakano, 2009). The outer layers absorb the radiation and shield the midplane. Other ionisation mechanisms are at work, but they are either highly localised (e.g., thermal ionisation in the inner disc $r \lesssim 0.3\,{\rm au}$), or are too weak to be effective (e.g., ionisation by radioactive decay is very slow).

Therefore, the requirement for sufficient magnetic coupling, (i.e., non-ideal effects below the coupling threshold), confines magnetically-driven inflow to the ionised surfaces of the disc. The 'layered accretion' model envisages inflow passing along ionised, surface layers while the underlying midplane 'dead zone' is too poorly ionised to carry any inflow (Gammie, 1996).

We consider a range of values for the accreting column density, but note that the column density ionised by cosmic rays, $\Sigma = 2\Sigma_{\rm CR} = 196\,{\rm g\,m^{-2}}$, is a natural choice for protoplanetary discs. Of course, our requirement for a power-law scaling of Σ means that our accreting column density decreases with orbital radius. It would be straightforward to drop the requirement for a power-law solution and solve the equations numerically for Σ constant in radius, fixed at the active column density.

The vertically-averaged MHD equations include contributions from the dead zone and active layers. However, the equations decouple into a pair of essentially independent equation sets, allowing us to focus on the active layer structure alone. Therefore, equations (4.44)–(4.49) should be considered as describing the active layer in the remainder of the analysis.

Not all parameter combinations are independent of one another. We have arranged the equation set to highlight degeneracies in parameter combinations. For example, aside from the continuity equation, the column density only appears in combination with the vertical magnetic field, B_z^2/Σ. So a solution for, say, B_r/B_z

will be identical if the B_z is halved and the column density is simultaneously quartered. This allows us to determine the behaviour of the solution to varying both B_z and Σ, while fixing one (we choose to fix $B_z = 1\,\mathrm{G}$ and allow Σ to vary).

Ambipolar diffusion also acts in essentially the same manner as Ohmic resistivity and so we focus on the effect of the resistivity on the solution. We have not combined them to form Pedersen diffusion $\eta_P = \eta_O + \eta_A$ as they do not appear in this combination in the perturbation analysis.

4.5.2 Results

Fig. 4.2 shows the resulting equilibrium model. The panels show the accretion rate, aspect ratio, inflow and azimuthal velocities, and radial and azimuthal magnetic field strengths. Solutions are shown for the standard parameter set given above, but with curves showing the effect of varying Hall drift as η_H/η_O =-3, 0, and 3, respectively.

The solution comprises three solution branches; the accretion rate shows monotonically increasing lower and upper branches connected by an intermediate branch. The solution is multivalued in the column density range 50–120 $\mathrm{g\,cm^{-2}}$. The three branches correspond to different physical regimes in the solution. Fig. 4.3 shows the relative strength of terms in the radial momentum equation for the three solution branches; the upper, middle and lower branches are shown in the top, middle, and bottom panels, respectively.

The lower branch is a slowly-accreting solution, with an accretion rate range $\dot{M} = 10^{-8}$– $5 \times 10^{-6}\, M_{\odot}$/year consistent with quiescent accretion in young circumstellar discs. The solution is an essentially Keplerian disc, with $v_\phi \approx v_K \equiv \sqrt{GM/r}$, except at low column density. There is a column-density cutoff at $\Sigma = 0.4\,\mathrm{g\,cm^{-2}}$ below which magnetic tension provides overwhelming radial support. Very little magnetic braking is needed to produce the low accretion rates on this branch, and so B_ϕ is correspondingly small. As such, our approximate relation for the external magnetic field based on a poloidal, current-free solution is good on this branch and B_r/B_z is constant in Σ. Hall drift is negligible compared to resistivity as it is weighted by the toroidal field component, whereas the radial field multiplies the Ohmic term. As such, the inflow velocity $-v_r = (B_r/B_z)\eta_O/(Hc_s)$ is constant in column density, reproducing the linear relationship between the accretion rate and column density $\dot{M} = -2\pi r \Sigma v_r$.

The solution doubles-back on itself, entering the intermediate branch at $\Sigma = 120\,\mathrm{g\,cm^{-2}}$. The transition between branches occurs as the toroidal component becomes large enough to influence the external field, $B_\phi = -\sqrt{p/(p-1)}B_z \approx -2.2 B_z$

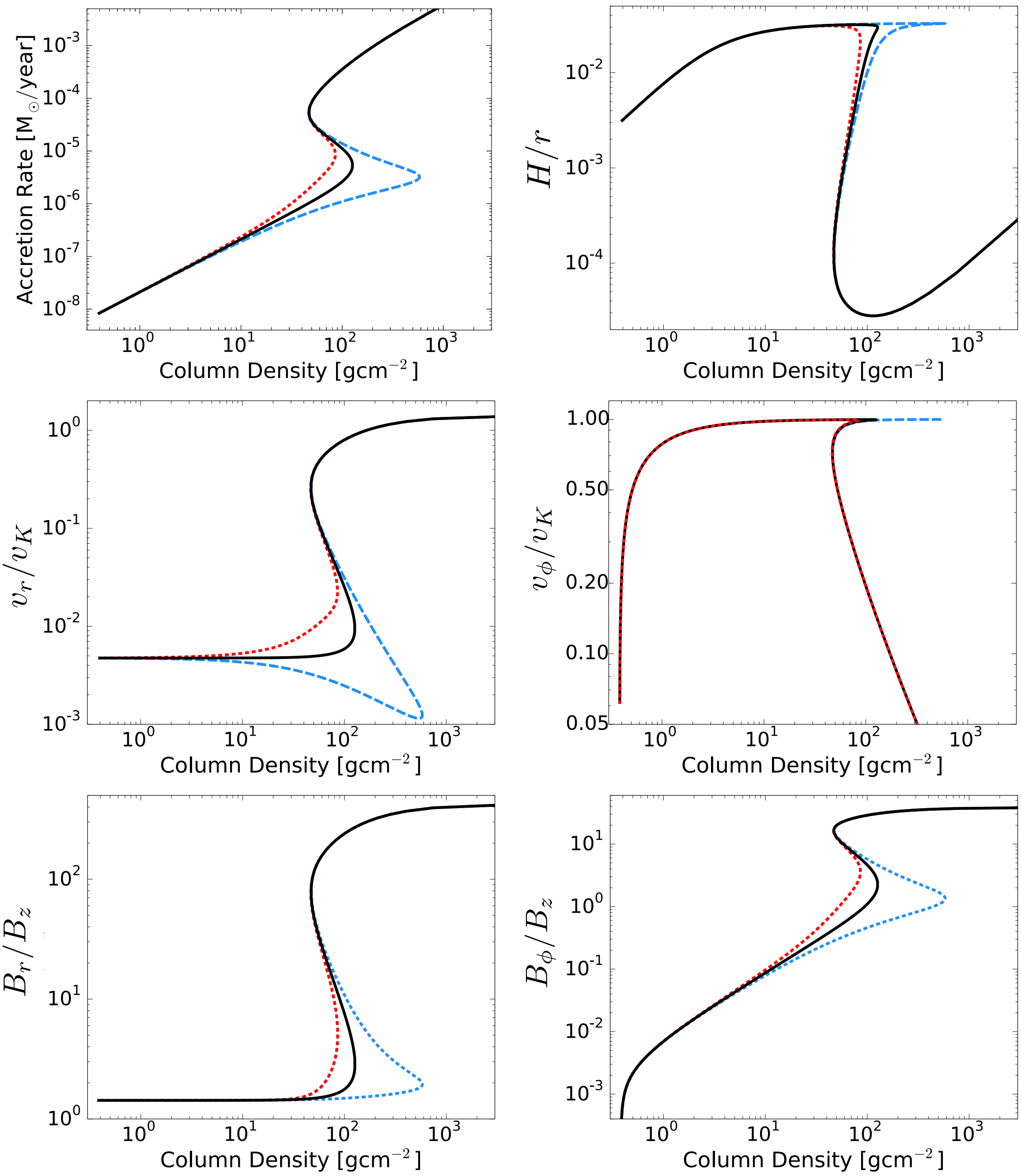

Figure 4.2: Equilibrium model as a function of column density, with the standard parameter set for a protoplanetary disc (see text). The panels show $\dot{M}$ (top-left panel), H/r (top-right panel), v_ϕ/v_K and $-v_r/v_K$ (centre-left and -right panel, respectively), B_r/B_z and $-B_\phi/B_z$ (bottom-left and -right panels, respectively). Solutions are shown for $\eta_H/(Hc_s)$ =-0.3, 0, and 0.3, as shown by the red, black, and blue curves, respectively.

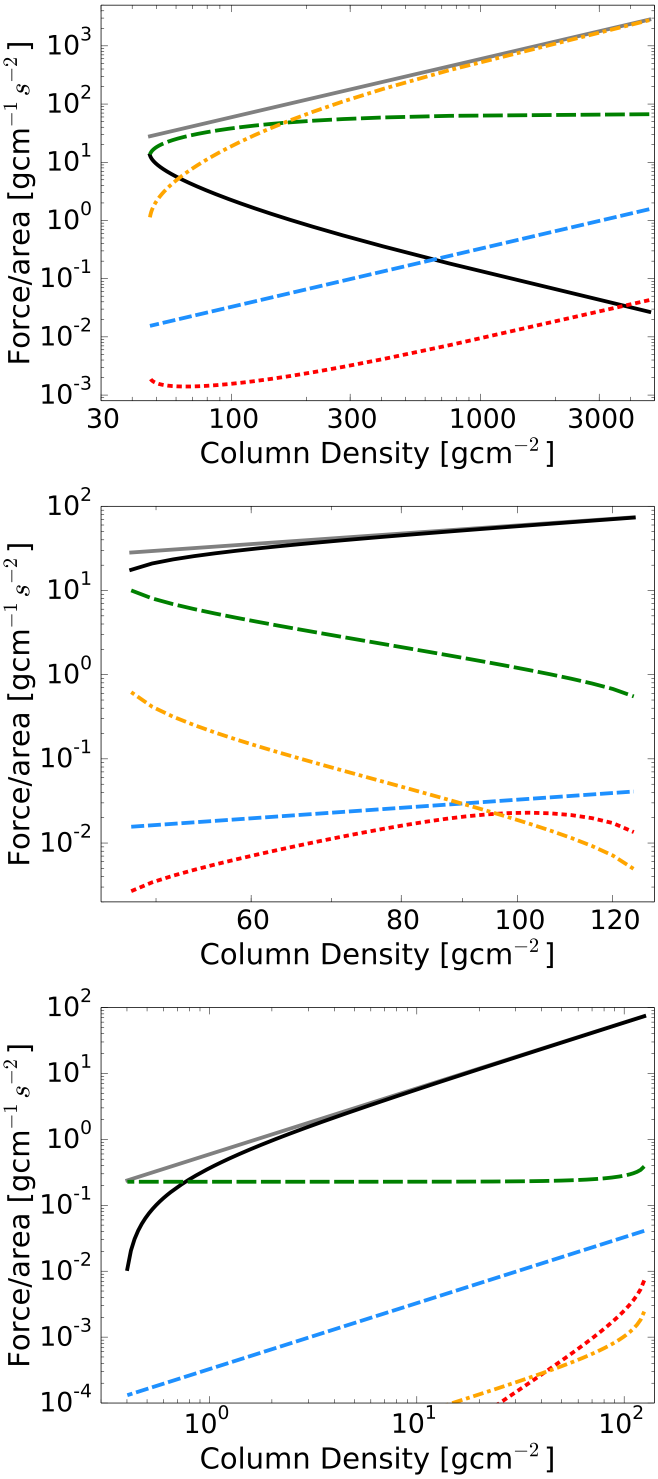

Figure 4.3: Terms in the radial momentum equation, equation (4.18), plotted against column density for $\eta_O = 0.1Hc_s$, η_H, η_A=0. The panels show the upper (top panel), middle (middle panel), and lower (bottom panel) solution branches. Terms shown are the gravitational (grey solid curve) and centripetal forces (black solid curve), pressure gradients (blue dashed line), magnetic tension (green long dashed line), magnetic pressure (red dotted curve) forces, and inertia (orange dot-dashed curve).

for our power-law index $p = 5/4$. Therefore, the azimuthal momentum equation, equation (4.45), shows that the turn-around occurs at a fixed accretion rate. The turning point can be calculated using equations (4.45), (4.47), and (4.48) using this value for B_ϕ and $v_\phi = v_K$:

$$\Sigma = 125\mathrm{g\,cm^{-2}} \left(\frac{r}{\mathrm{au}}\right) \left(\frac{B_z}{1\,\mathrm{G}}\right)^2 \left(\frac{\eta_O/(Hc_s)}{0.1}\right)^{-1} \left(\frac{c_s}{1\,\mathrm{km\,s^{-1}}}\right)^{-1}. \tag{4.50}$$

The enhanced magnetic field compresses the disc vertically, so that the scale height drops sharply with decreasing Σ. The ratio of the toroidal and radial field components is greatest at the base of the intermediate branch. Therefore, Hall drift has the greatest impact here, and is able to shift the turning-point to higher and lower column densities when it cooperates ($\eta_H < 0$) and counteracts ($\eta_H > 0$) the resistivity, respectively. This branch is unstable in the sense that the accretion rate grows with decreasing column density. This behaviour means that column density fluctuations are enhanced as $\dot{M}$ drops in denser regions (leading to pile up), and increases to empty under-dense regions.

The solution transitions from a rotationally-supported disc to a free-fall solution on the upper branch. This branch is characterised by rapid accretion at a rate $\dot{M} \gtrsim 10^{-5}\, M_\odot/\mathrm{year}$ similar to accretion outbursts. The solution enters the upper branch once magnetic tension becomes comparable to gravity, and the reducing the required centripetal acceleration. The transition can, again, be calculated using equations (4.45), (4.47), and (4.48), except that now we use $B_\phi/B_z \gg \sqrt{p/(p-1)}$ and the relation between the radial forces: $v_\phi^2/r = B_z B_r/(2\pi\Sigma) = -\frac{1}{2}g_r$:

$$\Sigma = 46\mathrm{g\,cm^{-2}} \left(\frac{r}{\mathrm{au}}\right)^{1/3} \left(\frac{B_z}{1\,\mathrm{G}}\right)^2 \left(\frac{\eta_O/(Hc_s)}{0.1}\right)^{-2/3} \left(\frac{c_s}{1\,\mathrm{km/s}}\right)^{-2/3}. \tag{4.51}$$

Here the inflow rate reaches the Keplerian velocity $v_r \sim v_K$ and $v_\phi \ll v_r$. As with the lower branch this yields a linear relationship between $\dot{M}$ and Σ, and the radial field adjusts to support this inflow. The field is tightly wrapped, yielding a strong radial field component. Our model would benefit from an improved treatment of the force-free field, as the extreme azimuthal field wrapping on this branch is at odds with the current-free solution we used to estimate field gradients in our approximation. Furthermore, as the field is highly inclined to the rotation axis it may be susceptible to a disc wind or magnetic reconnection. Although the radial field is much stronger than the vertical field, our approximation of dropping terms of order $(H/r)B_r/B_z$ is still valid, reaching at most 12% for $\eta_O = 0.1Hc_s$, and 35% for $\eta_H = 0.01Hc_s$.

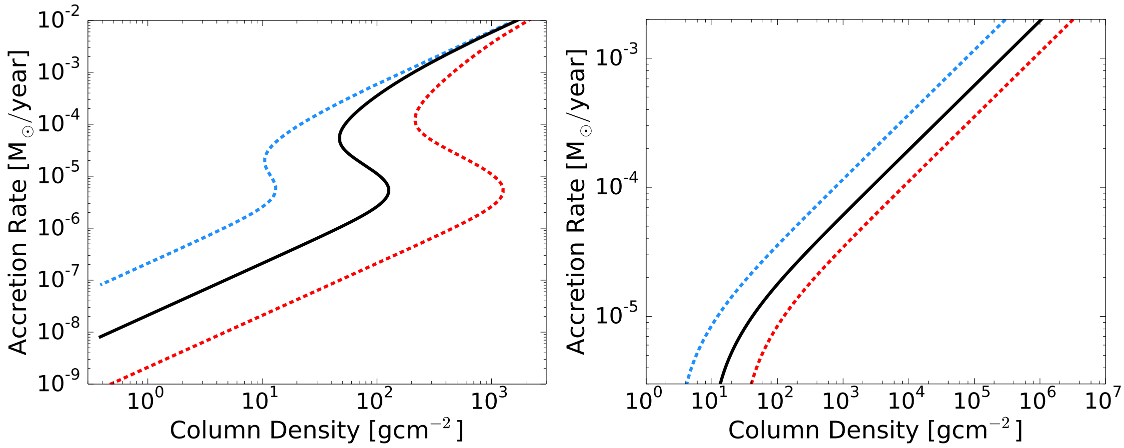

Figure 4.4: Mass accretion rate plotted as a function of active column density. The left panel shows the effect of varying Ohmic resistivity, with $\eta_O/(Hc_s)$ =0.01, 0.1, and 1, as the red dotted, black solid, and blue dashed curves, respectively. The right panel shows case of pure Hall (i.e., $\eta_O = 0$) with $\eta_H/(Hc_s)$ =-1, -3, and -10, as the red dotted, black solid, and blue dashed curves, respectively.

In many respects, our solution appears to connect the Keplerian and free-fall solutions of Braiding & Wardle (2012) with an intermediate branch. In their study, the azimuthal field was capped at $B_\phi \leqslant -B_z$ under the assumption that MHD instabilities would limit the toroidal field from becoming much stronger than the poloidal field (see Krasnopolsky & Königl, 2002). We do not cap B_ϕ, but we do find that B_ϕ plateaus at $B_\phi/B_z \approx -40$ on the upper branch.

Fig. 4.4 shows the effect of the magnetic diffusivities on the accretion rate. The left panel of 4.4 shows the effect of reducing (red-dotted curve) and increasing (blue-dashed curve) Ohmic resistivity by a factor of ten. This shifts the curve across in column density, and increasing resistivity reduces the range of column density with multiple solutions. The reason for this is that while the lower turning-point is for a fixed $\dot{M}$ the upper turning-point marks the transition to free-fall inflow. Higher resistivity increases field-line drift, and consequently gas inflow in equilibrium. Therefore, higher resistivity solutions have a larger v_r meaning that a shorter intermediate branch is needed for v_r to reach free-fall velocity. The right panel shows the pure Hall case. The curves show $\eta_H/(Hc_s)$ =-1, -3, and -10, but no solutions exist for the pure Hall case for $B_z < 0$ as it would produce $v_r > 0$. Similarly, no solution exists for $\eta_H, \eta_O, \eta_A = 0$ and $\eta_O, \eta_A = 0$, $B_z > 0$.

This 'S-shape' formed by the branches is typically associated with models of accretion outbursts, such as the thermal-viscous instability and gravo-magneto limit cycles (Pringle, 1981; Bell & Lin, 1994; Martin & Lubow, 2011a). A limit cycle can develop between the upper and lower branches if the accreting column flowing into a region is not matched to the local inflow speed. (Faulkner, Lin & Papaloizou, 1983; Latter & Papaloizou, 2012). If, through the build up of material, the column density of a lower branch solution somehow exceeds the upper limit of the branch, the solution is pushed out of equilibrium. Typically the solution follows a hysteresis loop, rising up to the upper branch and then, travelling down along to the end of the upper branch as the enhanced accretion rate empties the region; the solution jumps back onto the lower branch, and the cycle begins again (Faulkner, Lin & Papaloizou, 1983; Latter & Papaloizou, 2012). Simulations are needed to determine whether our model follows an analogous hysteresis loop.

4.6 Linear perturbation analysis

We would like to know whether this equilibrium is stable to small, axisymmetric, radial perturbations. We write perturbed quantities as a linear combination of the equilibrium solution $f_0(r)$ and perturbation $\delta f(r,t)$.

$$f = f_0(r) + \delta f(r,t). \tag{4.52}$$

We consider the linear growth regime, so that terms of $\mathcal{O}(\delta f^2)$ and above are set to zero.

We consider perturbations with a wavelength much less than the radial gradient length-scale of the equilibrium solution. This means that we can neglect terms of $\mathcal{O}(1/r)$ as compared with the perturbation wavenumber, k, taking $k + \mathcal{O}(1/r) \approx k$ in our analysis. This restriction is necessary as we discarded or approximated radial gradients in our equilibrium model.

We do not need to model the vertical structure to study radial wave modes, as we assume it responds and readjusts sufficiently rapidly that it can be taken to be constant in our analysis. However, this limits the validity of our equilibrium model on length-scales less than the scale-height and restricts our choice of wavenumber k to

$$r^{-1} \ll k \ll H^{-1}. \tag{4.53}$$

The equilibrium can then be considered as essentially constant on the perturbation length-scale. This allows us to use the WKB approximation to describe the perturbations as $\delta f(r,t) \propto \exp(ikr - i\omega t)/r$, appropriate in a cylindrical system. Derivatives of perturbed quantities, δf are reduced to $\partial(\delta f)/\partial t = -i\omega\delta f \exp(ikr - i\omega t)/r$, and $\partial(\delta f)/\partial r = (ik - r^{-1})\,\delta f \exp(ikr - i\omega t)/r \approx ik\delta f \exp(ikr - i\omega t)/r$.

4.6.1 Perturbed disc model

The aim is to develop a linearised set of equations, which we can solve to determine the corresponding solutions for ω. We will then determine whether or not there are any modes with significant growth to destabilise our equilibrium.

We allow for perturbations in Σ, H, v_r, v_ϕ, B_r, B_ϕ, and B_z but hold the non-ideal effects fixed [i.e. $\delta\eta_O$, $\delta(\eta_H/B)$, $\delta(\eta_A/B^2) = 0$].

Perturbing equations (4.17)–(4.21) is straightforward. As an example, we show the linearisation of the continuity equation using the local, and first-order approximations below:

$$\begin{aligned}
0 &= \frac{\partial(\Sigma + \delta\Sigma)}{\partial t} + \frac{1}{r}\frac{\partial}{\partial r}[r(\Sigma + \delta\Sigma)(v_r + \delta v_r)] \\
&\approx \frac{\partial \delta\Sigma}{\partial t} + \frac{1}{r}\frac{\partial}{\partial r}(r\Sigma\delta v_r + r\delta\Sigma v_r), \\
&= -i\omega\delta\Sigma + \left(ikv_r + \frac{v_r}{r} + \frac{dv_r}{dr}\right)\delta\Sigma + \left(ik\Sigma + \frac{\Sigma}{r} + \frac{d\Sigma}{dr}\right)\delta v_r, \\
&\approx (-i\omega + ikv_r)\,\delta\Sigma + ik\Sigma\delta v_r. \qquad (4.54)
\end{aligned}$$

Applying the same procedure to the remaining MHD equations for the disc yields:

$$\left(ikc_s^2 + \frac{1}{2}\frac{\partial v_r^2}{\partial r} - g_r - \frac{v_\phi^2}{r}\right)\delta\Sigma + \Sigma\,(-i\omega + ikv_r)\,\delta v_r - \frac{2}{r}\Sigma v_\phi \delta v_\phi$$
$$-\frac{1}{6\pi}ikB_\phi^2\delta H - \frac{1}{2\pi}B_r\delta B_z - \frac{1}{2\pi}B_z\delta B_r + \frac{ikH}{6\pi}B_\phi\delta B_\phi = 0, \qquad (4.55)$$

$$(-i\omega + ikv_r)\,\delta v_\phi + \frac{1}{r}\frac{\partial(rv_\phi)}{\partial r}\delta v_r - \frac{B_\phi}{2\pi\Sigma}\delta B_z - \frac{B_z}{2\pi\Sigma}\delta B_\phi + \frac{B_zB_\phi}{2\pi\Sigma^2}\delta\Sigma = 0, \qquad (4.56)$$

$$\left(\frac{g_rH^2}{r} + c_s^2\right)\delta\Sigma + \left(\frac{2Hg_r\Sigma}{r} - \frac{B_r^2}{8\pi} - \frac{B_\phi^2}{8\pi}\right)\delta H - \frac{HB_r}{4\pi}\delta B_r - \frac{HB_\phi}{4\pi}\delta B_\phi = 0, \qquad (4.57)$$

$$-i\omega\frac{H}{2\pi r}\delta\Psi_z + HB_z\delta v_r + v_rB_z\delta H + \left[\eta_O + \frac{\eta_A}{B^2}\left(\frac{1}{3}B_\phi^2 + B_r^2 + B_z^2\right)\right]\delta B_r$$
$$+\left(v_rH + \frac{\eta_H}{B}B_\phi + 2\frac{\eta_A}{B^2}B_zB_r\right)\delta B_z + \left(\frac{\eta_H}{B}B_z + \frac{2}{3}\frac{\eta_A}{B^2}B_rB_\phi\right)\delta B_\phi = 0, \quad (4.58)$$

and

$$\delta B_z = \frac{ik}{2\pi r}\delta\Psi_z, \quad (4.59)$$

4.6.2 Perturbed atmosphere model

Solving for the external field perturbations is complicated by the need to account for vertical, as well as radial, waves. We avoided treating vertical waves in the disc by vertically-averaging and so limiting our analysis to modes with a length-scale larger than the scale-height, i.e. $kH \gg 1$. However, in the atmosphere radial and vertical waves will have a similar length-scale and will travel at the same velocity.

We perturb Gauss' law and the force-free equation set, equations (4.37) and (4.38), respectively. We perturb the exact, rather than the approximate [i.e., equation (4.43)], force-free relation as it retains key gradient information. Our solution for the perturbed field will depend on the equilibrium field configuration, which we have approximated; however, we find that the resulting error in our solution is of $\mathcal{O}[(kr)^{-1}]$, which is no greater than error introduced by our use of the local approximation.

The linearised Gauss' law and force-free condition are

$$\nabla\cdot(\delta\mathbf{B}) = 0, \quad (4.60)$$
$$(\nabla\times\mathbf{B})\times\delta\mathbf{B} + (\nabla\times\delta\mathbf{B})\times\mathbf{B} = 0. \quad (4.61)$$

The gradient length scale of unperturbed field is of $\mathcal{O}(r)$, and so it is much larger than the perturbation wavelength. Therefore, the second term in equation (4.61) dominates in our local approximation, so that the perturbed current is parallel to the unperturbed magnetic field,

$$(\nabla\times\delta\mathbf{B})\times\mathbf{B} = 0. \quad (4.62)$$

We only require the solution immediately above the disc surface to connect to the disc solution, and so a locally-cartesian coordinate system, $\hat{\mathbf{x}} = \hat{\mathbf{r}}$, $\hat{\mathbf{y}} = \hat{\phi}$, $\hat{\mathbf{z}} = -\hat{\theta}$, will suffice. As in the disc, we assume axisymmetry, dropping azimuthal derivatives (i.e., $\partial/\partial y = 0$). Without loss of generality, we take $z > 0$.

Pairing equation (4.62) with Gauss' law yields a triplet of coupled equations:

$$\begin{aligned} \frac{\partial \delta B_x}{\partial x} + \frac{\partial \delta B_z}{\partial z} &= 0, &(4.63)\\ \frac{(\nabla \times \delta \mathbf{B})_x}{B_x} - \frac{(\nabla \times \delta \mathbf{B})_y}{B_y} &= 0, &(4.64)\\ \frac{(\nabla \times \delta \mathbf{B})_y}{B_y} - \frac{(\nabla \times \delta \mathbf{B})_z}{B_z} &= 0. &(4.65)\end{aligned}$$

We still evaluate radial derivatives of the perturbed field with the local approximation $\partial/\partial x \to ik$,

$$\begin{aligned} ik\delta B_x + \frac{\partial \delta B_z}{\partial z} &= 0, &(4.66)\\ B_x \frac{\partial \delta B_x}{\partial z} - ikB_x\delta B_z + B_y \frac{\partial \delta B_y}{\partial z} &= 0, &(4.67)\\ B_z \frac{\partial \delta B_x}{\partial z} - ikB_z\delta B_z - ikB_y\delta B_y &= 0. &(4.68)\end{aligned}$$

However, we will have to solve for the wavenumber of vertical modes, k_z, by solving this set of linear ordinary differential equations.

We recast this equation set in matrix form,

$$\frac{d\delta \mathbf{B}}{dz} = A\delta \mathbf{B}, \tag{4.69}$$

where

$$A = \begin{bmatrix} 0 & ik\frac{B_y}{B_z} & ik \\ 0 & -ik\frac{B_x}{B_z} & 0 \\ -ik & 0 & 0 \end{bmatrix} \tag{4.70}$$

Our local treatment allows us to treat B_x, B_y, and B_z as constant in height, so A is a constant matrix. This system admits a solution of the form

$$\delta \mathbf{B} = \sum_{n=1}^{3} c_n \delta \mathbf{B}_n \equiv \sum_{n=1}^{3} c_n \delta \mathbf{B}_{\lambda n} \exp(\lambda_n z), \tag{4.71}$$

where $\delta \mathbf{B}_{\lambda n}$, λ_n, and c_n are the n^{th} eigenvector, eigenvalue, and constant coefficient, respectively. There are three perturbation mode solutions,

$$\delta \mathbf{B}_1 = \begin{bmatrix} 1 \\ 0 \\ i\frac{k}{|k|} \end{bmatrix} \mathrm{e}^{-|k|z+ikx-i\omega t} \tag{4.72}$$

$$\delta\mathbf{B}_2 = \begin{bmatrix} 1 \\ 0 \\ -i\frac{k}{|k|} \end{bmatrix} \mathrm{e}^{|k|z+ikx-i\omega t} \tag{4.73}$$

$$\delta\mathbf{B}_3 = \begin{bmatrix} 1 \\ -\frac{B_x^2+B_z^2}{B_x B_y} \\ \frac{B_z}{B_x} \end{bmatrix} \mathrm{e}^{-ik\frac{B_x}{B_z}z+ikx-i\omega t}. \tag{4.74}$$

Fig. 4.5 shows the vector field for the local orientation of the total magnetic field $\mathbf{B} + f_n\delta\mathbf{B}_n$, as a function of radius and height. The net field is shown projected in the x–z, and y–z planes for each mode, n. A factor f_n exaggerates the perturbation relative to the background field $\mathbf{B}$ to make the effect of the perturbation $\delta\mathbf{B}_n$ clear.

Modes 1 and 2 correspond to the modes found by Lizano et al. (2010). They are purely poloidal modes (i.e., $\delta B_y = 0$), and have $\pm\pi/2$ phase difference between the radial and vertical components. They are also independent of the equilibrium field components Bx, B_y, and B_z. The vertical wavenumber, $k_z = \pm i|k|$ governs the vertical profile of the perturbations. Mode 1 damps with height, and so the net field $\mathbf{B} + f_1\delta\mathbf{B}_1 \to \mathbf{B}$ at large z. Perturbations for this mode do not propagate far from the disc.

On the other hand, mode 2 grows with height and become large relative to the background field. The exponential increase in the perturbation amplitude with height is unphysical and so we discard this solution.

The third mode is fundamentally different. It has a non-zero azimuthal perturbation, and is oscillatory in both radius and height. Fig. 4.5 shows that the poloidal components of the perturbation and unperturbed field are parallel (i.e., $\delta B_{z3}/\delta B_{x3} = B_z/B_x$). However, the perturbation is also perpendicular to the field (i.e., $\delta\mathbf{B}_3 \cdot \mathbf{B} = 0$). The equilibrium field controls the vertical wavenumber, $k_z = kB_x/B_z$ and relative strength of the field perturbation components.

It is not clear whether $\delta\mathbf{B}_3$ is physically relevant. Our magnetic-braking model assumes that the field is connected to a distant, massive object, such as remnant molecular cloud material. This mode does not decay with height, and so it relies on perturbations in the cloud as well as the disc. We have not accounted for the finite travel time of modes in the atmosphere and so we do not have a sense of whether it is the disc or the cloud which is driving the perturbation. A more detailed model of magnetic braking is needed to determine whether this solution is viable. We discard this mode in our study, but suggest that further analysis is needed.

In summary, we have retained only $\delta\mathbf{B}_1$ as being physically relevant, as it does

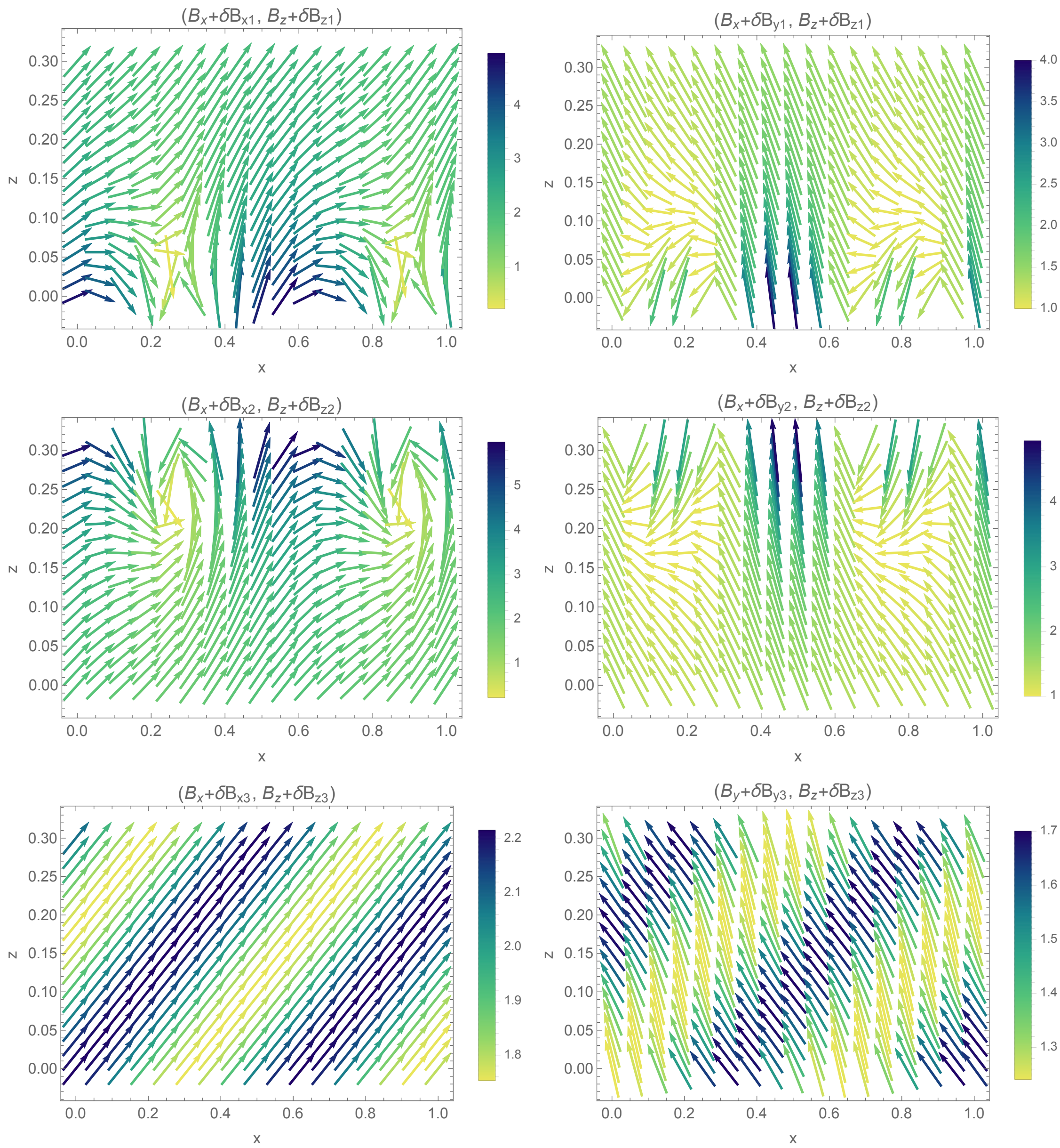

Figure 4.5: Vector plot of the orientation of the total perturbed magnetic field, $\mathbf{B} + f_n\delta\mathbf{B}_n$, as a function of radius, x, and height, z. Top, centre, and bottom pairs of panels show the perturbations for modes n = 1, 2, and 3, respectively. Left and right panels show the projection in the x–z, and y–z planes, respectively. Colour scale indicates field strength, but perturbations have been exaggerated relative to the background field using pre-factor f_n = 3, 0.35, and 0.25 to make the effect of the perturbations clear. The results are presented for $kx = 10$ and a background field of $\mathbf{B} = (1.73, -1, 1)$.

$$
\begin{bmatrix}
-i\omega + ikv_r & ik\Sigma & 0 & 0 & 0 & 0 & 0 \\
\begin{matrix} ikc_s^2 + \frac{1}{2}\frac{\partial v_r^2}{\partial r} \\ -\frac{1}{r}v_\phi^2 - g_r \end{matrix} & (-i\omega + ikv_r)\Sigma & -\dfrac{2\Sigma v_\phi}{r} & -\dfrac{B_r}{2\pi} & -\dfrac{ikB_\phi^2}{6\pi} & -\dfrac{B_z}{2\pi} & \dfrac{ikHB_\phi}{6\pi} \\
\dfrac{B_z B_\phi}{2\pi\Sigma^2} & \frac{1}{r}\frac{\partial(rv_\phi)}{\partial r} & -i\omega + ikv_r & -\dfrac{B_\phi}{2\pi\Sigma} & 0 & 0 & -\dfrac{B_z}{2\pi\Sigma} \\
0 & HB_z & 0 & \begin{matrix} \frac{-i\omega H}{ik} + Hv_r \\ +\eta_H \frac{B_\phi}{B} + 2\eta_A \frac{B_r B_z}{B^2} \end{matrix} & v_r B_z & \eta_0 + \eta_A - \eta_A \dfrac{2B_\phi^2}{3B^2} & \eta_H \dfrac{B_z}{B} + \eta_A \dfrac{2B_r B_\phi}{3B^2} \\
\dfrac{g_r H^2}{r} + c_s^2 & 0 & 0 & 0 & \dfrac{2Hg_r\Sigma}{r} - \dfrac{B_\phi^2 + B_r^2}{8\pi} & -\dfrac{HB_r}{4\pi} & -\dfrac{HB_\phi}{4\pi} \\
0 & 0 & 0 & 0 & 0 & 0 & 1 \\
0 & 0 & 0 & \dfrac{i|k|}{k} & 0 & 1 & 0
\end{bmatrix}
$$

Figure 4.6: Matrix, $\mathcal{M}$, summarising the linearised equation set, as referenced in equation (4.77).

not induce perturbations in the cloud. We are interested in the perturbation at the disc surface, and so setting $z = 0$ gives the relationship between the components of the perturbation $\delta\mathbf{B}_1[\equiv (\delta B_r, \delta B_\phi, \delta B_z)]$,

$$
\delta B_r = -i\frac{|k|}{k}\delta B_z \tag{4.75}
$$

$$
\delta B_\phi = 0. \tag{4.76}
$$

4.6.3 Dispersion relation

Having assembled the relationships between perturbed quantities, we are in a position to solve for the modes of the system. The complete system of equations, equations (4.54)–(4.59) and (4.75)–(4.76), can be summarised by the matrix relation

$$
\mathcal{M}\delta\mathbf{x} = 0, \tag{4.77}
$$

where $\delta\mathbf{x} = [\delta\Sigma, \delta v_r, \delta v_\phi, \delta B_z, \delta H, \delta B_r, \delta B_\phi]^T$ is the vector of perturbed variables, and the matrix $\mathcal{M}$ is given in Fig. 4.6.

It is helpful to rescale the equations into a dimensionless form to identify dominant terms and isolate parameter combinations. We rescale using ΣH^2, H, and H/c_s, as units of mass, distance and time, respectively. For example, the corresponding unit of magnetic field strength is $(H/\Sigma)^{1/2}c_s^{-1}$, and the scaled magnetic field, $B_z' = B_z c_s\sqrt{\Sigma/H}$. We apply the scaling to $\omega' = \omega H/c_s$, $k' = kH$, and $\delta\mathbf{x}'$. Henceforth we drop the primes, and quantities are expressed in their dimensionless form.

We subdivide $\mathcal{M}$ into four smaller units,

$$\mathcal{M}\delta\mathbf{x} \equiv \begin{bmatrix} \mathcal{A} - i\omega\mathcal{I} & \mathcal{B} \\ \mathcal{C} & \mathcal{D} \end{bmatrix} \begin{bmatrix} \mathbf{x_1} \\ \mathbf{x_2} \end{bmatrix} \tag{4.78}$$

where $\mathbf{x_1} = [\delta\Sigma, \delta v_r, \delta v_\phi, \delta B_z]^T$, and $\mathbf{x_2} = [\delta H, \delta B_r, \delta B_\phi]^T$, and I is the 4×4 identity matrix. The submatricies $\mathcal{A}$, $\mathcal{B}$, $\mathcal{C}$ and $\mathcal{D}$ are 4×4, 4×3, 3×4 and 3×3 matrices, respectively, and are as shown below:

$$\mathcal{A} = \begin{bmatrix} ikv_r & ik & 0 & 0 \\ \begin{matrix} ik - g_r - {v_\phi}^2/r \\ + \frac{d\log v_r}{d\log r}{v_r}^2/r \end{matrix} & ikv_r & -\frac{2v_\phi}{r} & -\frac{B_r}{2\pi} \\ \frac{B_\phi B_z}{2\pi} & \frac{d\log rv_\phi}{d\log r}\frac{v_\phi}{r} & ikv_r & -\frac{B_\phi}{2\pi} \\ 0 & ikB_z & 0 & \begin{matrix} ikv_r + ik\eta_H\frac{B_\phi}{B} \\ +2ik\eta_A\frac{B_r B_z}{B^2} \end{matrix} \end{bmatrix} \tag{4.79}$$

$$\mathcal{B} = \begin{bmatrix} 0 & 0 & 0 \\ -\frac{ik{B_\phi}^2}{6\pi} & -\frac{B_z}{2\pi} & \frac{ikB_\phi}{6\pi} \\ 0 & 0 & -\frac{B_z}{2\pi} \\ ikv_r B_z & \begin{matrix} ik(\eta_0+\eta_A) \\ -\frac{2}{3}ik\eta_A\frac{{B_\phi}^2}{B^2} \end{matrix} & \begin{matrix} ik\eta_H\frac{B_z}{B} \\ +\frac{2}{3}ik\eta_A\frac{B_r B_\phi}{B^2} \end{matrix} \end{bmatrix} \tag{4.80}$$

$$\mathcal{C} = \begin{bmatrix} \frac{g_r}{r} + 1 & 0 & 0 & 0 \\ 0 & 0 & 0 & 0 \\ 0 & 0 & 0 & \frac{i|k|}{k} \end{bmatrix} \tag{4.81}$$

$$\mathcal{D} = \begin{bmatrix} \frac{2g_r}{r} - \frac{{B_r}^2 + {B_\phi}^2}{8\pi} & -\frac{B_r}{4\pi} & -\frac{B_\phi}{4\pi} \\ 0 & 0 & 1 \\ 0 & 1 & 0 \end{bmatrix} \tag{4.82}$$

This forms a pair of simultaneous equations,

$$(\mathcal{A} - i\omega\mathcal{I})\mathbf{x_1} + \mathcal{B}\mathbf{x_2} = 0 \tag{4.83}$$

$$\mathcal{C}\mathbf{x_1} + \mathcal{D}\mathbf{x_2} = 0, \tag{4.84}$$

allowing us to eliminate $\mathbf{x_2}$:

$$\mathbf{x_2} = -\mathcal{D}^{-1}\mathcal{C}\mathbf{x_1}. \tag{4.85}$$

Inserting this relation into equation (4.83) reduces the task of solving for ω to an eigenvalue problem,

$$(\mathcal{A} - \mathcal{B}\mathcal{D}^{-1}\mathcal{C})\mathbf{x_1} = i\omega\mathbf{x_1}. \tag{4.86}$$

We solve for the eigenvalues and eigenvectors using LAPACK's routine `geev`, implemented in `eig` from the Python library `numpy.linalg` (Anderson et al., 1999; Jones et al., 2001). This yields four complex solutions for ω, given by the eigenvalues. The associated eigenvectors describe the relative phase and amplitude of perturbed quantities.

4.6.4 Results

Fig. 4.7 shows the solutions, $\omega = \omega_r + i\omega_i$, for $|kr| = 10$ and the standard parameter set. The four solutions are labelled ω_1, ω_2, ω_3, ω_4, and shown as the red, orange, blue and black curves, respectively. We plot the real component (ω_r; top panel), and complex component (ω_i; bottom panel) separately. Positive and negative values of ω are represented by solid and dashed curves, respectively. A negative complex component decays with time, whereas a positive complex component grows with time, and constitutes an instability.

The modes are multivalued, exhibiting the multiple equilibrium solution branches. Modes on the lower branch consist of two sound-like waves (i.e., ω_3 and ω_4) and two resistivity-driven waves (i.e., ω_1 and ω_2), and reduce to those found by Lizano et al. (2010). Mode ω_2 is growing across the entire lower branch whereas ω_1 and ω_4 are unstable in part of the domain. Mode frequencies rise sharply along the intermediate branch, where the growth rate of ω_1 and ω_2 reaches up to $\approx \Omega$. On the upper branch, solutions develop into two growing, and two decaying modes. The fastest-growing modes, ω_1 develops into an instability within a dynamical time-scale, whereas ω_2 decreases sharply with increasing column density. Solutions merge into one another and show a pairing between ω_3 and ω_4, and modes ω_1 and ω_2.

Fig. 4.8 shows the effect of varying resistivity and Hall drift. Solutions on the upper branch are essentially unaffected by a ten-fold decrease/increase in resistivity, but the lower branch scales as $\omega_i \propto \eta_O$, suggesting these are resistivity-driven modes. Hall drift alters the range of column densities with multiple solutions, but it does not change the nature (i.e., growing or decaying), and has little effect on the growth rate.

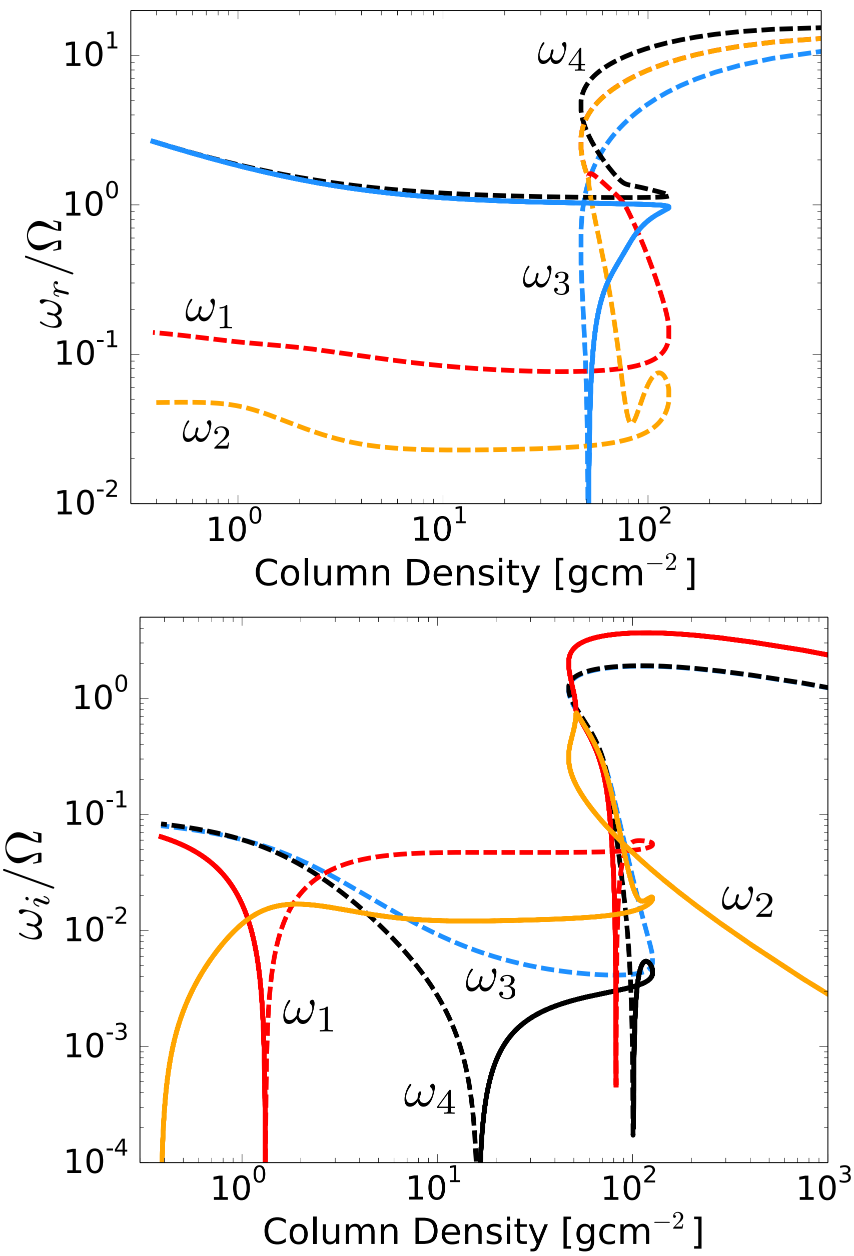

Figure 4.7: Wave solutions as a function of column density for $|kr| = 10$ and the standard parameter set. The solution is separated into real (top panel) and complex (bottom panel) and normalised by Keplerian orbital angular frequency. Solid and dashed portions of the curves indicate where the solution is positive and negative, respectively. The modes labelled ω_1, ω_2, ω_3, and ω_4 are shown by the red, orange, blue and black curves, respectively.

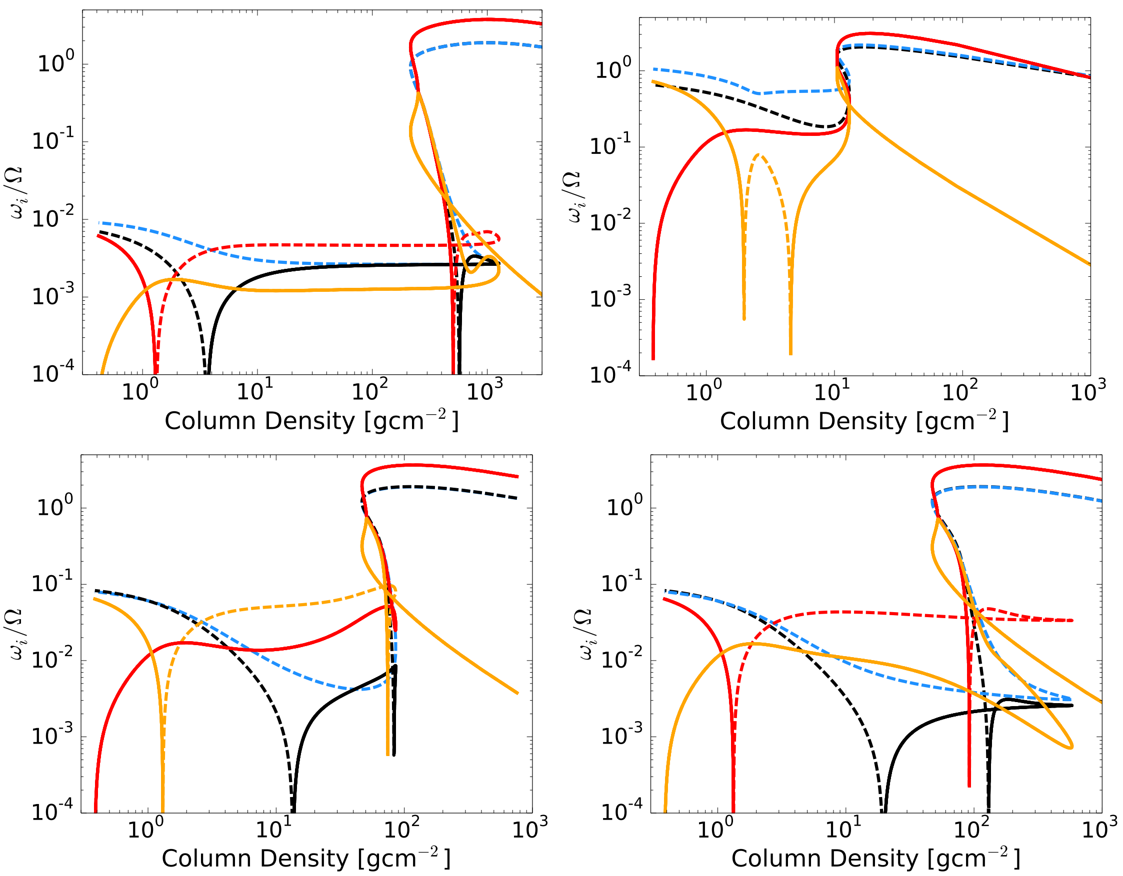

Figure 4.8: Imaginary component of wave solutions as a function of column density, for $|kr| = 10$. Pure resistive (i.e., $\eta_H = 0$) solutions are shown in the top panels with $\eta_O/(Hc_s) = 0.01$, 1 in left and right panels, respectively; Hall drift $\eta_H/(Hc_s) = -0.3$, 0.3 is added to solutions with $\eta_O = 0.1Hc_s$ in the bottom-left and -right panels, respectively.

We need to verify that the solutions are significant in light of approximations we have made in this analysis. Secular evolution associated with the growth of the central object occurs on a much longer time-scale than our solutions (i.e., $t_{\rm grow} = M/\dot{M} \gg \omega^{-1}$) , and so our treatment of the stellar mass as constant was valid. Our assumption that the vertical disc structure readjusts sufficiently rapidly to be taken as constant underpins our neglect of vertically propagating wave modes.Vertical averaging limits our solutions to those acting on a longer timescale than the vertical mixing timescale (i.e., $\omega^{-1} > t_{\rm mix} = H/c_s$). Our disc is sufficiently thin that vertical mixing is effectively instantaneous as compared with mode time-scales, justifying our approach.

The local approximation $kr \gg 1$, poses a greater challenge. By discarding radial gradients in the equilibrium model and perturbations, we have assumed that the disc is uniform on the perturbation length-scale k^{-1}. We have dropped terms like α/r compared with ik, where α is a real value of order unity. For example, in deriving the linearised continuity equation, equation (4.54), we approximated

$$\begin{aligned} ikv_r\left(1-\frac{i}{kr}-\frac{1}{kr}\frac{d\log v_r}{d\log r}\right) &= ikv_r\left(1-\frac{i}{2kr}\right), \\ &\approx ikv_r. \end{aligned} \tag{4.87}$$

Retaining radial gradient terms is roughly equivalent to introducing a small complex component to the wavenumber, $k \rightarrow k + i\alpha/r$. A significant solution would have a growing/decaying component of ω which is large enough compared to the real part, that changes in k of order $1/r$ do not affect whether it is growing or decaying. Therefore, we require that $\mathrm{Im}(\omega)\geqslant kr\mathrm{Re}(\omega)$ for significant growth in the local approximation. We tested this by determining whether the modes remained growing or decaying when they were computed for wavenumbers $k - i/r$, k and $k + i/r$. Solutions are considered reliably stable/unstable if the sign of ω_i did not change with this perturbation to k.

We find that on the upper branch ω_1 is unstable, ω_3 and ω_4 are stable, but the growth of ω_2 is too weak to say. All solutions are reliable on the intermediate branch, so that ω_1, ω_2 are unstable and ω_3 and ω_4 are stable. On the lower branch all modes are sensitive to radial gradients. This is further supported by the scaling $\omega_i \propto 1/(kr)$. Lower branch solutions can be considered stable on time-scales less than the mode growth rate, $t = \omega^{-1} \approx kr\Omega^{-1}$, but our local analysis is not sufficient to determine the stability of these solutions on longer time-scales.

The fastest-growing mode, ω_1, is shown as the red curve in Fig. 4.7. It experiences significant growth on the upper and intermediate branches. We can gain an understanding of the physical nature of this instability by considering the interplay between the perturbed quantities. An instability is produced by a positive feed-back loop in the linearised equation set, equations (4.54)–(4.59) and (4.75).

The dominant terms in the linearised equations for this mode, on the upper branch, are

$$\frac{\partial\delta\Sigma}{\partial t}+v_r\frac{\partial\delta\Sigma}{\partial r}+\Sigma\frac{\partial\delta v_r}{\partial r}=0, \tag{4.88}$$

$$\frac{\partial\delta v_r}{\partial t}+v_r\frac{\partial\delta v_r}{\partial r}-\frac{B_r\delta B_z}{2\pi\Sigma}=0, \tag{4.89}$$

$$\frac{\partial\delta v_\phi}{\partial t}+v_r\frac{\partial\delta v_\phi}{\partial r}-\frac{B_\phi\delta B_z}{2\pi\Sigma}=0, \tag{4.90}$$

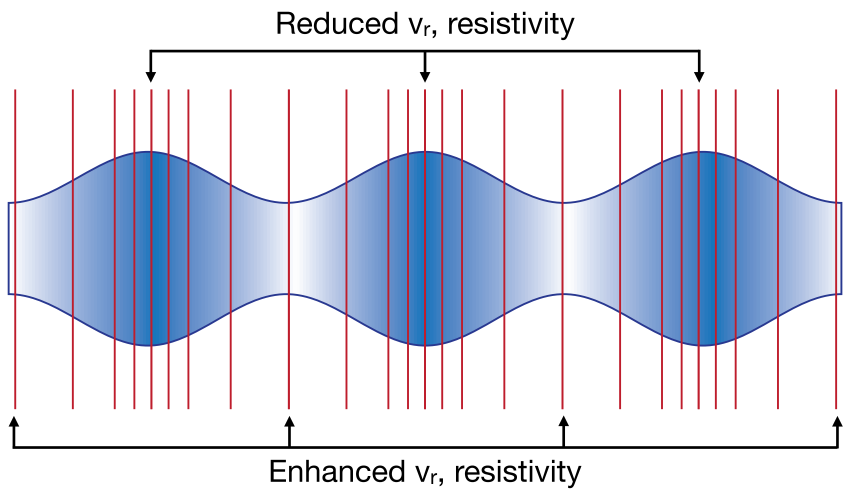

Figure 4.9: Schematic of the instability of the fastest-growing mode, ω_1, as described in the text. A radial perturbation wave is introduced to disc quantities. The scale height is shown as the lower and upper horizontal disc boundaries, column density is represented by the intensity of the blue fill colour, and the vertical field strength is shown by the density of the red, vertical field-lines.

$$\frac{\partial B_z}{\partial t} + v_r \frac{\partial \delta B_z}{\partial r} + \frac{\eta_O B_r}{H^2} \frac{\partial \delta H}{\partial r} = 0, \tag{4.91}$$

$$c_s^2 \delta\Sigma + \frac{2 g_r \Sigma H \delta H}{r} = 0, \tag{4.92}$$

and

$$\delta B_r + \frac{i|k|}{k} \delta B_z = 0. \tag{4.93}$$

The angular momentum equation and the force-free relation, equations (4.90) and (4.93), are auxiliary equations as these are the only equations δv_ϕ and δB_r appear in. The remaining equations describe runaway growth of perturbations from a feedback loop connecting B_z, v_r, Σ and H.

For example, consider the impact of small radial perturbations in the column density, as illustrated in Fig. 4.9. This produces a wave in the scale-height due to the spatially-varying thermal pressure support [equation (4.92)]. Magnetic field gradients are on a length-scale H so the perturbation increases the field-line drift in regions of enhanced vertical compression, and vice versa. The field drifts out of the under-dense regions, and consequently reduces magnetic tension there. This allows for an increased inflow velocity in under-dense regions, draining the material into the denser regions. The result is an enhancement of the initial perturbations, leading to runaway growth.

There is another, weaker unstable mode on the upper and intermediate branch (i.e., ω_2). The interplay between the perturbations is more complicated in this case, so our analysis into the origin of this instability is ongoing.

In summary, we have found that the intermediate and upper branches of our equilibrium solution are unstable to local, axisymmetric, radial perturbations. The growth rate rises sharply along the intermediate branch, reaching $\omega_i/\Omega \approx 4$ on the upper branch. Our local approximation was not adequate to determine whether solutions on the lower branch are reliably growing or decaying.

4.7 Discussion

In this study we modelled an accretion disc braked by magnetic torques from a large-scale field. We considered a disc which is connected to a surrounding massive cloud of gas by a magnetic field. The field is wound up by the rotation of the disc, and winding is transported along field lines to the cloud. The massive cloud is essentially unaffected by the magnetic torque applied by the field. It pulls back on the field, which in turn brakes the disc.

We used the axisymmetric, vertically-averaged equation set in Braiding & Wardle (2012) to develop a 1D model of the radial structure. An approximate force-free model for the external field was developed, which was exact in the limit of a vanishing azimuthal field. We did not treat the physics of the braking, but assume it produced just the right amount of B_ϕ that the resulting inflow velocity is consistent with that permitted by field-line drift. Non-ideal effects were incorporated, as parameters, to provide the necessary field line drift preserving the field against accretion with gas inflow.

We sought a power-law equilibrium solution characterised by a uniform mass inflow rate. We applied this to model accreting surface layers, which are ionised by external radiation. Solutions are only possible for $\Sigma > 0.4\,\mathrm{g\,cm^{-2}}$ for $B_z = 1\,\mathrm{G}$, below which the azimuthal solution drops sharply due to overwhelming magnetic tension. We found that some accreting column densities have multiple solutions (e.g., $\Sigma = 50$–$120\mathrm{g\,cm^{-2}}$). Hall drift cooperates with, or counteracts resistivity to effect range of column densities with multiple solutions.

There are up to three solutions, characterised by low-, intermediate-, and high-accretion rates. The lower branch is a weakly magnetised, Keplerian solution and is consistent with quiescent protoplanetary disc accretion ($\dot{M} = 10^{-8}$–$10^{-6}\,M_\odot/\mathrm{yr}$). The solution enters the intermediate branch once magnetic pressure from the toroidal field becomes strong.

On the upper solution branch, the disc is in essentially free-fall with a high accretion rate more representative of accretion outbursts ($\dot{M} = 10^{-5}$–$10^{-3}\, M_{\odot}$/yr). This is a highly-magnetised solution for which the field is tightly-wrapped and lies predominantly in the plane of the disc (i.e., $B_z \ll B_r,\, B_\phi$). Strong magnetic pressure compresses the disc vertically, yielding an aspect ratio $H/r \approx 10^{-5}$. Although we have not included outflows in our analysis, this solution branch is likely to be susceptible to a magnetocentrifugal wind and this should be accounted for. It is also possible that magnetic reconnection may cap the strength of B_ϕ and B_r (Krasnopolsky & Königl, 2002). Magnetic squeezing strongly compresses the disc height on the upper branch, and so B_r, B_ϕ may be constrained, in part, by striking a balance between compression and reconnection.

The curve of equilibrium $\dot{M}$ as a function of column density doubles back on itself, and the three solution branches form an 'S-shape'. This feature is similar to that found in models of thermal-viscous instability and gravo-magneto limit cycles (Pringle, 1981; Bell & Lin, 1994; Martin & Lubow, 2011a), although it has a different physical origin in each case. It is typically associated with accretion outbursts as a limit cycle can develop between the upper and lower branches (Faulkner, Lin & Papaloizou, 1983; Latter & Papaloizou, 2012). This is caused by a feedback process in which the disc is pushed out of equilibrium by a gas pile-up in conditions near the upper end of the lower branch, rapidly increasing the accretion rate until the solution reaches the upper branch, and similarly at the lower end of the upper branch. Time-dependent calculations are needed to trace the evolution of our model to determine whether or not a limit-cycle develops.

Our model has been developed with the idea that magnetic braking is produced by a distant, massive cloud. Other studies have considered alternate braking mechanisms such as torsional Alfvén waves (Krasnopolsky & Königl, 2002), or a disc wind (Blandford & Payne, 1982; Wardle & Königl, 1993). Each of these mechanisms yields a distinct equilibrium disc state which would be interesting to cross-compare.

We have assumed that the braking produced by the cloud matches the inflow produced by field-line drift. This constraint gave us a solution for B_ϕ; however, B_ϕ is ultimately governed by details of the braking mechanism (Krasnopolsky, Li & Blandford, 1999; Ogilvie & Livio, 2001). Furthermore, although our approximate model for the force-free atmosphere is valid in the limit of vanishing B_ϕ/B_z, we find strong toroidal field solutions on the upper branch.

Vertical averaging greatly simplified our analysis; the resulting 1D (or 2D if azimuthal structure is included) MHD equation set is very versatile and can be applied to other similar processes. For example, Lizano et al. (2010) applied a similar equation set to incorporate magnetic fields into an equivalent Toomre's Q.

An important application would be to model magnetic-flux transport (e.g., see Lubow, Papaloizou & Pringle, 1994). Flux transport studies are key in determining the magnetic field distribution and evolution in protoplanetary discs (Guilet & Ogilvie, 2012, 2013, 2014; Okuzumi, Takeuchi & Muto, 2014; Takeuchi & Okuzumi, 2014), particularly as very few constraints can be drawn from observations at present. Time-dependent flux transport has the potential to bunch together the magnetic field lines, enhancing the field strength and gradients. In particular, it would be interesting to determine the sensitivity to the inclusion of a toroidal field, which is typically neglected (e.g., Okuzumi, Takeuchi & Muto 2014; Takeuchi & Okuzumi 2014).

We performed a perturbation analysis to study the linear growth of axisymmetric, radial modes in the equilibrium. We considered local perturbations, for which the perturbation length-scale is much less than the radial gradient length-scales in the equilibrium (i.e., the radius). The straightforward extension of our analysis to consider non-axisymmetric modes would be very interesting.

We allowed for radial and vertical wave vectors in the force-free atmosphere, where the radial and vertical gradients are similar. We found three perturbation modes in the atmosphere; these correspond to perturbations which are decaying, growing, or oscillatory with height. Of these, only the first (pure-poloidal) mode was kept as physically relevant. The growing mode is clearly unphysical, as it would correspond to large perturbations in the cloud's rotation.

It is not clear whether the oscillatory mode is realistic as it relies on the simultaneous excitation of detailed velocity structures in the cloud and disc. We have neglected time-derivatives in the atmosphere as the signal speed is so fast that we assume the atmosphere adjusts instantaneously. This has the effect of removing any sense of causality in the atmosphere, and so it is not clear if this mode is, in fact, disc-driven. More analysis is needed to determine the viability of this mode.

We found four mode solutions, each of which was multi-valued like the equilibrium model. At least two modes are unstable on the upper and intermediate branches. The most unstable mode grows extremely rapidly in these conditions, with a growth time less than the dynamical time-scale. It is produced by a feed-back loop for which magnetic tension slows inflow, an increases the column density and scale-height through enhanced pressure support. This reduces the effectiveness of non-ideal effects in washing out the developing field gradient, allowing for runaway field growth.

Modes on the lower branch have a resistivity-driven complex component; however, it is typically too small to be considered reliable. The growing/decaying component is so weak relative to the real component that it is sensitive to radial gradients, which we neglected with the local approximation. We mimicked the inclusion of these terms by introducing a complex component to the wavenumber. Solutions with a very weak imaginary component change sign when a complex wavenumber is included, indicating that we cannot rely on the nature of the solution (i.e., growing or decaying). Nevertheless, they can be considered as approximately stable within $t \lesssim kr\Omega^{-1}$; however, a non-local treatment would be needed to confirm their behaviour on longer time-scales.

The unstable upper solution branch is in marked contrast with the standard 'S-curve' produced by the thermal-viscous instability. Our solution may also be susceptible to addition non-axisymmetric instabilities, all of which would lead to different evolution from the standard case. For example, the disc presented here could not evolve along the upper solution-branch in equilibrium, as seen in simulations of the thermal-viscous instability (e.g., Latter & Papaloizou, 2012). However, this need not rule out limit-cycle behaviour all together, as solutions do not need to evolve along the upper branch to form a limit-cycle (e.g., see simulated tracks by Bell & Lin, 1994).

Our force-free model sets important boundary conditions for our disc, yet it poses a challenge to our locally-valid solution. We have developed an equilibrium solution which is valid locally, in the sense that different disc annuli evolve independent of one another. Accretion connects different radii by transporting material over radial distances, but this occurs on such a long time-scale, $t = M/\dot{M}$ that we may neglect this effect. On the other hand, in the atmosphere, signals propagate so rapidly, (i.e., at the Alfvén speed), that field adjustments at one radius are transmitted to the remainder of the disc, effectively instantaneously. This compromises our local approach, and means that our model is sensitive to radial gradients in B_r, which we approximated in our force-free model. Thus, our analysis would benefit from an improved treatment of the force-free field.

In summary, we present a model for the steady-state, radial structure of a magnetically-braked accretion disc. We find that up to three accretion states are possible for a range of column densities relevant to protoplanetary discs. We find that intermediate- and high-inflow solutions are unstable to local, radial wave modes in the linear regime. Furthermore, the existence of multiple solutions may make the disc susceptible to accretion limit-cycles.

5
Conclusions

This thesis addressed the role of magnetic fields in giant planet formation, and protoplanetary disc dynamics. Magnetic fields are thought to be the primary driver of accretion flow in protoplanetary discs, which may result from hydromagnetic turbulence, outflows, or magnetic braking. Each of these mechanisms has a wide-ranging influence on disc dynamics.

For example, random fluctuations induced by hydromagnetic turbulence affects grain settling (Fromang & Nelson, 2009), collisional grain growth (Youdin & Goodman, 2005), the onset of runaway gas accretion (Okuzumi & Ormel, 2013; Ormel & Okuzumi, 2013), and disc chemistry through turbulent mixing (Ilgner & Nelson, 2006, 2008). Associated viscous diffusion also governs gap opening, with implications for Type II migration (Lin & Papaloizou, 1986; Nelson & Papaloizou, 2004). Winds and jets launched by large-scale fields can radically alter dynamics in protoplanetary discs (Wardle & Königl, 1993; Shu et al., 1994; Bai & Stone, 2013), and potentially circumplanetary discs (Quillen & Trilling, 1998; Fendt, 2003; Machida, Inutsuka & Matsumoto, 2006; Gressel et al., 2013). Magnetic tension may also stabilise discs against gravitational instability (Lizano et al., 2010).

Three key physical processes relating to giant planet gas capture and magnetically-driven accretion were analysed in this study: circumplanetary disc accretion, gas crossing gaps in protoplanetary discs, and magnetic-braking in accretion discs.

The first study addressed accretion in circumplanetary discs surrounding giant planets. Circumplanetary discs are thought to channel accretion flow onto a protoplanet during the final gas-capture phase. Current astrophysical accretion disc models rely on MRI turbulence or gravitoturbulence as the source of effective viscosity within the disc. However, magnetically-coupled accreting regions in these models are so limited that the disc may not support inflow at all radii, or at the required rate.

We examined the conditions needed for self-consistent accretion, in which the disc is susceptible to accretion driven by magnetic fields or gravitational instability. We modelled the radial structure of a circumplanetary disc with a Shakura-Sunyaev α-disc. A plane-parallel atmosphere model was used with the Zhu, Hartmann & Gammie (2009) opacity law to calculate the disc temperature resulting from local accretion heating. The midplane ionisation fraction was calculated for ionisation by irradiation by cosmic rays and X-rays, radioactive decay and thermal ionisation. From this we were able to calculate the strength of non-ideal effects, along with Toomre's Q to assess gravitational instability.

We found that a standard, constant-α disc is only coupled to the field by thermal ionisation in the inner $30\,R_J$, with strong magnetic diffusivity prohibiting accretion through the bulk of the midplane. In light of the failure of the constant-α disc to produce accretion consistent with its viscosity we dropped the assumption of constant-α. Instead, we considered an alternate model in which α varies radially according to the level of magnetic turbulence or gravitoturbulence. We found that in this disc a vertical field may drive accretion across the entire disc, whereas MRI can drive accretion out to $\sim 200\,R_J$, beyond which Toomre's $Q = 1$. The gravitationally unstable region cools too slowly for fragmentation and so gravitoturbulence ensues. Thermal ionisation is the only source of ionisation strong enough for magnetic coupling, and so a self-consistent disc is necessarily hot ($T \gtrsim 800\,\mathrm{K}$), and consequently unrealistically massive ($M_{\mathrm{disc}} \sim 0.5\,M_J$).

Circumplanetary discs are unlikely to satisfy the extreme conditions required for steady-state, midplane accretion. Instead, it is likely that inflow is confined, primarily to ionised surface layers (Turner, Lee & Sano, 2014). Our analysis suggests that the accreting column in active surface layers is insufficient for steady-state accretion, and so the disc would experience time-dependent accretion, such as the MRI-gravitational instability limit-cycles (Martin & Lubow, 2011a; Lubow & Martin, 2012).

Accretion has critical implications for giant planet satellite growth. Regular moons around solar-system giant planets are believed to have formed within circumplanetary discs. It is possible that several generations of satellites grew in the disc before the present-day satellites were formed (Canup & Ward, 2006), as accretion flow carries satellites inward and onto the planet (Canup & Ward, 2002; Sasaki, Stewart & Ida, 2010). The surviving generation of satellites in our solar system are icy, indicating that they formed in a late, cooler phase of the disc (Coradini et al., 1989). This limits the disc inflow rate to ensure that accretion heating is not so strong as to compromise the temperature profile inferred from satellite composition studies (Mosqueira & Estrada, 2003; Barr & Canup, 2008). However, until extrasolar satellites are discovered, just how representative solar-system satellite systems are will be unclear (Kipping et al., 2013).

Recent simulations of gas capture may have made some headway towards resolving the uncertainty in the accretion flow. Three-dimensional hydrodynamical and MHD simulations have challenged the traditional view of in-plane inflow, finding that flow within the Hill sphere is dominated by high-latitude flows (Tanigawa, Ohtsuki & Machida, 2012; Gressel et al., 2013). This reduces the accretion flow that the disc needs to support, and allows satellites to form in a relatively low-mass circumplanetary disc without significant accretion. As such, the distribution of mass flux incident on the disc as a function of radius is a critical boundary condition for circumplanetary disc models. Further studies are needed to develop a robust physical description of the flow geometry and determine how much of the accreting material is processed across the disc.

The second study examined the influence of magnetic fields on the gas dynamics in gaps surrounding giant planets. Gas captured by a protoplanet flows across a gap encircling the planet, and a magnetic field carried along with the flow potentially influences the accretion flow. Gap crossing has been simulated with varying degrees of attention to field evolution (pure hydrodynamical, ideal, and resistive MHD], but as yet there has been no detailed assessment of the role of the field accounting for all three non-ideal MHD effects: Ohmic resistivity, ambipolar diffusion, and Hall drift.

We presented a detailed investigation of gap magnetic field structure as determined by non-ideal effects. Since full non-ideal simulations are computationally expensive, we took an a posteriori approach; assuming that the field is passively drawn along with the gas, we used the hydrodynamical simulation by Tanigawa, Ohtsuki & Machida (2012), to post-calculate MHD quantities and analyse the gap field structure.

We calculated the ionisation fraction produced by cosmic rays, stellar X-rays and radioactive decay, accounting for charge capture by grains. From this we determined the strength of non-ideal effects to determine whether MRI field gradients could be sustained, and if a toroidal field could couple to the gas flow. The magnetic field strength in the protoplanetary disc was estimated from inferred accretion rates, and accounted for flux-freezing in the gap.

We confirmed that our use of a hydrodynamical base model was valid as magnetic coupling is strong enough that the field is dragged into the gap. Furthermore, magnetic forces are too weak to influence the disc structure, except in the disc atmosphere above $z > 2$–$3H_p$ where the gas density, and consequently pressure, is low. Flux-freezing enhances the field in the gap over the surrounding protoplanetary disc, as it is pinned to the upper layers of the dense circumplanetary disc. We mapped out the approximate field geometry across the gap, identifying regions according to whether non-ideal effects permitted a predominantly poloidal, toroidal or turbulent field. We found that a toroidal field couples throughout most of the gap, and an MRI field is maintained between $0.5H_p < z < 2H_p$.

Hall drift modifies the turbulent and toroidal field components. Hall-MRI extends the turbulent field to the midplane if the vertical component of the magnetic field is the favourable orientation, aligned with the rotation axis. We found that a similar effect influences the strength and direction of the toroidal field. Hall drift enhances azimuthal field winding if the vertical component of the field is anti-parallel to the rotation axis, and wraps the field in the opposite direction if the field and rotation axes are aligned.

Our simple, a posteriori approach is successful for modelling regions of strong Ohmic resistivity and ambipolar diffusion, as the field has little effect on the flow, other than inducing turbulence. However, it is difficult to anticipate the effect of Hall drift as it is dissipationless and can introduce small-scale field structure (Sano & Stone, 2002; Kunz & Lesur, 2013; Lesur, Kunz & Fromang, 2014; O'Keeffe & Downes, 2014; Bai, 2015). We modelled the effect of Hall drift on turbulence and on the azimuthal component, but the interplay between the field and disc can produce complex behaviour in Hall-dominated flows (e.g., zonal flows; Lesur, Kunz & Fromang, 2014). Further analysis is needed to probe the effect of Hall drift, both in the gap and in the unperturbed protoplanetary disc.

The third study addressed the more general case of accretion powered by large-scale magnetic fields. Large-scale fields can transport angular momentum through the launching of a magnetocentrifugal wind, or brake a disc through magnetic torques. Strong evidence for protoplanetary disc MRI-inactive zones has renewed interest in transport by large-scale fields, which may be at work across more of the disc owing to the less stringent magnetic coupling requirement.

We presented a model of a magnetically-braked accretion disc. We developed a 1D model of the radial structure by vertically-averaging the axisymmetric, MHD equation set (Krasnopolsky & Königl, 2002; see also Braiding, 2011). The disc is threaded by a magnetic field which emerges into an atmosphere above and below the disc. We determined an approximate force-free model for the orientation of field lines at the outer surface of the disc to account for the tendency of concentrations of magnetic flux to splay out.

Non-ideal effects were included (as parameters) to provide necessary field-line drift maintaining the field against accretion with gas inflow. We considered the case for which the disc is magnetically-braked by the transfer of angular momentum to a massive cloud by the magnetic field.

We sought a local, power-law equilibrium solution characterised by a uniform inflow rate, $\dot{M}$, and valid up to $\mathcal{O}(H/r)$. We found power-law indices of $-\frac{1}{2}$ for velocities and surface density, $-\frac{5}{4}$ for magnetic field components (akin to the Blandford & Payne, 1982 disc-wind solution), and a constant aspect-ratio. Magnetic tension limits solutions to a range of column densities as it reduces v_ϕ through strong radial support at low and high column densities.

We found that a range of column densities admit multiple equilibrium solutions. We find up to three solutions are possible: (i) a slowly-accreting lower branch consistent with quiescent accretion in protoplanetary discs ($\dot{M} = 10^{-8}$–$10^{-5}\,M_\odot$/year for $B_z = 1\,\mathrm{G}$), (ii) a highly magnetised upper branch with a rapid accretion rate similar to outburst events in young circumstellar discs ($\dot{M} = 10^{-5}$–$10^{-3}\,M_\odot$/year), and (iii) an unstable intermediate branch connecting the other two solutions. The transition between lower and intermediate branch occurs as B_ϕ exceeds B_z and magnetic pressure from the azimuthal field becomes strong. The solution turns onto the upper branch as magnetic braking exceeds centrifugal support and the disc changes from a rotationally-supported, Keplerian disc to a state of free-fall. Given the importance of the magnetic field in the intermediate and upper branches, our model would benefit from an improved treatment of the force-free field outside the disc.

The solutions form an 'S-shaped' curve when $\dot{M}$ is plotted as a function of accreting column. This feature is associated with models of accretion outbursting; a limit cycle can develop if the local inflow rate does not match the mass flux into a region. When this occurs, gas pile-up near the end of the lower branch, (and similarly with gas drain at the end of the upper branch), pushes the solution out of equilibrium and along a hysteresis loop along the upper and lower solution branches (Faulkner, Lin & Papaloizou, 1983; Latter & Papaloizou, 2012). Time dependent-calculations are needed to determine whether such a limit-cycle could also develop in this system.

We performed a perturbation analysis to determine the stability of our equilibrium solution to local, radial modes. In this first pass we considered axisymmetric perturbations but this analysis should be extended to include non-axisymmetric modes.

We identified three perturbation modes in the atmosphere; we kept the pure-poloidal mode which damps with height, but discarded another mode which grows exponentially with height as being unphysical. The third mode is fundamentally different as it is oscillatory in height, and it perturbs B_ϕ. We also discarded this mode in our analysis as it requires perturbations in the cloud, which we have not treated in our analysis. However, further analysis is needed to determine whether this mode is physically relevant.

We found four perturbation mode solutions which we analysed to determine if there was any significant growth indicative of an instability. We found two growing solutions on the intermediate and upper branches. The most unstable mode grows rapidly, on a time-scale shorter than the dynamical time-scale. This growth is produced by a feed-back loop caused by the interplay between resistivity, magnetic tension, and magnetic-compression of the scale-height.

The other unstable mode grows too weakly to be significant, given our local analysis. We found that the complex component of the wave frequency is so small compared to the real component, that the nature of the solutions (i.e., growing or decaying) is sensitive to the radial gradients that we neglected in our local approximation. The other two solutions are decaying modes, and are reliably decaying under the local approximation. Lower branch solutions are all sensitive to terms of $\mathcal{O}[(kr)^{-1}]$, so a non-local treatment is needed to determine whether they grow or decay. These are resistive modes, and so their growth/decay rate is sensitive to the strength of magnetic coupling.

Large-scale fields have long been recognised as a key candidate for driving accretion in accretion discs. Provided that there is sufficient ionisation to couple the field to the disc, disc winds and magnetic-braking are very efficient at transporting angular momentum. Despite this, recent advances in MRI simulations have somewhat diverted efforts from modelling this mechanism in protoplanetary discs. Our first-pass investigation into the structure of magnetically-braked discs warrants further analysis to assess the potential for accretion driven by large-scale torques, and to determine the time-dependent behaviour of these systems. In particular, a proper treatment of non-ideal effects would ascertain whether (and where) this solution is appropriate in protoplanetary discs, and other magnetically-braked accretion discs.

Our findings suggest that an assessment of the importance of magnetic fields in giant planet formation must be done for each physical process individually. The main reason for this is the strong contrast in density and field gradient length-scales between the protoplanetary- and circumplanetary discs, as well as within the discs themselves. As such, non-ideal effects can vary considerably about the coupling threshold. This highlights the importance of non-ideal effects in studying magnetic fields in giant planet formation and protoplanetary discs. We have considered their capacity to quench turbulence and limit the extent of accreting zones, govern magnetic field structure, and provide the field-line drift necessary for preventing the field from being accreted with gas inflow.

Models of giant planet gas-capture will greatly benefit from the continued development of global non-ideal simulations of protoplanetary disc accretion and gap-crossing (e.g., Gressel et al., 2013, 2015), as well as the more specialised Hall-MHD studies (e.g., Kunz & Lesur, 2013; Lesur, Kunz & Fromang, 2014; Bai, 2014, 2015). There is scope for further analytic and semi-analytic calculations, particularly in circumplanetary disc studies where artificial viscosity is a concern for simulations.

A
Appendix

A.1 Weak-field condition for Hall-MRI

In this appendix we develop the weak-field condition for Hall-MRI used in §3.2.3. Developing and sustaining MRI turbulence requires two conditions: (i) firstly, that field perturbations must grow fast enough, and (ii) secondly, the wavelength of the fastest-growing turbulent mode λ, must be contained within a disc scale-height (i.e., $\lambda \leqslant H$). The wavelength of the fastest-growing Hall-MRI mode is [see equation (B14) of Wardle & Salmeron, 2012]

$$\lambda = \frac{\pi}{\nu}\left[3s\eta_H\Omega - 4\eta_P\nu - 4v_{a,z}^2 + \frac{10v_{a,z}^2\Omega^2}{\nu^2+\Omega^2}\right]^{\frac{1}{2}}, \tag{A.1}$$

where ν is the growth rate of the fastest-growing mode. In the Hall MHD limit, $\eta_P = 0$, the maximum growth rate attains the ideal rate $\nu = \frac{3}{4}\Omega^{-1}$ (Wardle & Salmeron, 2012). Using this result in strong-Hall limit, $\eta_H\Omega v_{a,z}^{-2} \gg 1$, the wavelength of the fastest-growing mode is approximately

$$\lambda \approx 2\pi\sqrt{\frac{\eta_H}{\Omega}}, \tag{A.2}$$

up to a constant factor of order unity.

Ensuring that the two MRI conditions [equations (A.1), (A.2) above] are met allows us to bracket the Hall-drift:

$$\frac{v_{a,z}^2}{\Omega} \leqslant \eta_H \leqslant \Omega \left(\frac{H}{2\pi}\right)^{,} \tag{A.3}$$

which, with the thin-disc approximation $H = c_s/\Omega$, leads to the weak-field limit

$$\beta_z = \frac{2c_s^2}{v_{a,z}^2} \geqslant 8\pi^2. \tag{A.4}$$

This is identical to that in the ideal and resistive MRI regimes [equation (3.13); Okuzumi & Hirose, 2011].

A.2 Non-ideal effects acting on a toroidal field

Here we determine the coupling threshold for a toroidal field using the azimuthal component of the induction equation, as used in §3.2.3. We consider a Keplerian disc with velocity, $\mathbf{v} = \Omega r\hat{\boldsymbol{\phi}}$, independent of height, and uniform transport coefficients η_O, η_H, η_A for simplicity.

Shear generates a toroidal component from a poloidal field in the inductive term: $[\nabla \times (\mathbf{v} \times \mathbf{B})]_\phi = -\frac{3}{2}\Omega B_r$. The resistive term, $[-\nabla \times (\eta_O \nabla \times B)]_\phi = \eta_O(\nabla^2 B_\phi - B_\phi/r^2) \sim \eta_O B_\phi/H^2$, is dominated by vertical gradients (see Section 3.2.4; Wardle & Königl, 1993), as are the Hall and ambipolar terms, which scale similarly. Comparing the two terms yields the coupling criterion[1]

$$\eta < \Omega H^2, \tag{A.5}$$

where $\eta = \eta_P, \eta_H$.

How will the field evolve once it decouples from the gas motion? Recasting the induction equation to show the field line drift, $\mathbf{V_B}$, makes this clear (Wardle & Salmeron, 2012):

$$\frac{\partial \mathbf{B}}{\partial t} = \nabla \times \left\{ (\mathbf{v} + \mathbf{V_B}) \times \mathbf{B} - \eta_O \left[(\nabla \times \mathbf{B}) \cdot \hat{\mathbf{B}} \right] \hat{\mathbf{B}} \right\}, \tag{A.6}$$

where

$$\mathbf{V_B} = \frac{\eta_P}{B} (\nabla \times \mathbf{B})_\perp \times \hat{\mathbf{B}} - \frac{\eta_H}{B} (\nabla \times \mathbf{B})_\perp \tag{A.7}$$

The azimuthal component of the drift velocity, $V_{B,\phi}$, controls the wrapping of the field lines with the shear. Neglecting terms of $\mathcal{O}(H/r)$, the azimuthal drift velocity is (Braiding & Wardle, 2012):

$$V_{B,\phi} = \frac{\eta_P}{H}\frac{B_z B_{\phi,s}}{B^2} - \frac{\eta_H}{H}\frac{B_{r,s}}{B} \tag{A.8}$$

$$\equiv V_P + V_H, \tag{A.9}$$

where we have separated the Pedersen and Hall drift components. Pedersen drift always resists winding, tending to reduce $|B_{\phi,s}|$ and straighten field lines. On the other hand, the Hall component will enhance or resist winding according the sign of $B_{r,s}$.

In the natural configuration for $s = 1$ (i.e., $B_{r,s} > 0$, and $B_{\phi,s} < 0$ for $z > 0$),

[1]This threshold is a factor of $10\,(H/r)^{-2} \sim 5 \times 10^3$ lower than Turner & Sano (2008), as we allow for vertical gradients in the non-ideal terms.

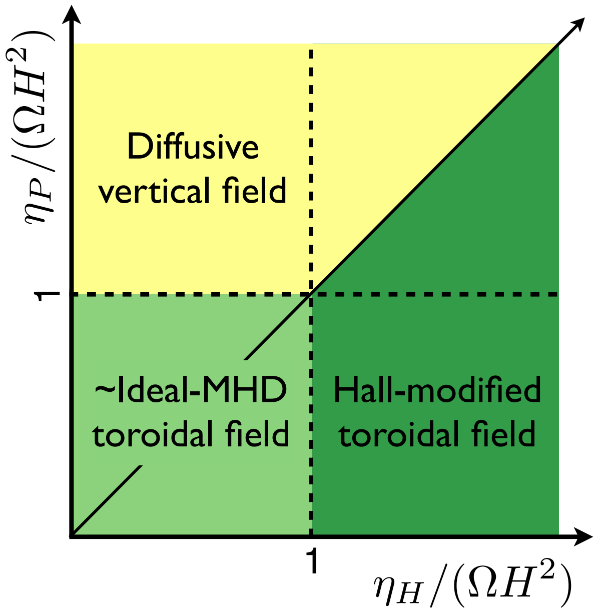

Figure A.1: Regions of η_H–η_P parameter space, shaded according to the toroidal field drift. Ideal MHD (light green) and Hall dominated MHD (dark green) will sustain a toroidal field, although the orientation of the field varies with the vertical field orientation in the Hall-MHD region. Pedersen diffusion only permits a vertical field in the yellow region.

$V_H < 0$ and $V_P < 0$ so that the components cooperate in unwrapping the field. For dominant Hall, the unwrapping will overshoot, winding the field in the opposite direction so that $B_{\phi,s} > 0$. For the anti-aligned field, $s = -1$, the natural configuration is $B_{r,s} < 0$, and $B_{\phi,s} > 0$ above the midplane. Once again, Pedersen resists wrapping of the field lines and if it dominates the field will tend towards vertical. On the other hand, now Hall drift tends to enhance field motion along $\hat{v}_\phi$ so that even if the field is somehow wound against the flow (i.e., $B_{\phi,s} > 0$) both components cooperate to restore $B_{\phi,s} \geqslant 0$ in equilibrium.

This behaviour is summarised in Fig. A.1, which shows how the resulting field geometry varies in the η_H–η_P parameter space. Non-ideal effects are weak in the lower-left quadrant (light green), with the toroidal field wound up by the disc so that $B_z B_\phi < 0$. Pedersen diffusion dominates above the diagonal (yellow region), so that the field tends toward vertical. The Hall effect counteracts diffusion below the diagonal (dark green), so that the toroidal component is enhanced for $s = -1$ or counter-wrapped when $s = 1$.

References

Adams F. C., 2011, ApJ, 730, 27

Alexander D. R., Ferguson J. W., 1994, ApJ, 437, 879

Alibert Y., Mordasini C., Benz W., Winisdoerffer C., 2005, A&A, 434, 343

Alibert Y., Mousis O., Benz W., 2005, A&A, 439, 1205

Anderson E. et al., 1999, LAPACK Users' Guide, 3rd edn. Society for Industrial and Applied Mathematics, Philadelphia, PA

Andrews S. M., Williams J. P., 2005, ApJ, 631, 1134

Armitage P. J., 2011, ARA&A, 49, 195

Armitage P. J., Livio M., Pringle J. E., 2001, MNRAS, 324, 705

Armstrong R., Kulesza B. L. J., 1981, Institute of Mathematics and its Applications, 17, 56

Artymowicz P., 1993, ApJ, 419, 166

Artymowicz P., Lubow S. H., 1996, ApJ, 467, L77

Asplund M., Grevesse N., Sauval A. J., Scott P., 2009, ARA&A, 47, 481

Ayliffe B. A., Bate M. R., 2009a, MNRAS, 397, 657

Ayliffe B. A., Bate M. R., 2009b, MNRAS, 393, 49

Ayliffe B. A., Bate M. R., 2012, MNRAS, 427, 2597

Bae J., Hartmann L., Zhu Z., Nelson R. P., 2014, ApJ, 795, 61

Bai X.-N., 2014, ApJ, 791, 137

Bai X.-N., 2015, ApJ, 798, 84

Bai X.-N., Stone J. M., 2013, ApJ, 769, 76

Balbus S. A., 2003, ARA&A, 41, 555

Balbus S. A., Hawley J. F., 1991, ApJ, 376, 214

Balbus S. A., Hawley J. F., 1992, ApJ, 400, 610

Balbus S. A., Hawley J. F., 2000, Space Sci. Rev., 92, 39

Balbus S. A., Terquem C., 2001, ApJ, 552, 235

Bally J., Reipurth B., Davis C. J., 2007, Protostars and Planets V, 215

Barr A. C., Canup R. M., 2008, Icarus, 198, 163

Baruteau C., Fromang S., Nelson R. P., Masset F., 2011, A&A, 533, A84

Bate M. R., Lubow S. H., Ogilvie G. I., Miller K. A., 2003, MNRAS, 341, 213

Bell K. R., Cassen P. M., Klahr H. H., Henning T., 1997, ApJ, 486, 372

Bell K. R., Lin D. N. C., 1994, ApJ, 427, 987

Blandford R. D., Payne D. G., 1982, MNRAS, 199, 883

Blum J., Wurm G., 2008, ARA&A, 46, 21

Bodenheimer P., Pollack J. B., 1986, Icarus, 67, 391

Boley A. C., 2009, ApJ, 695, L53

Bonnell I., Bastien P., 1992, ApJ, 401, L31

Borucki W. J. et al., 2010, Science, 327, 977

Boss A. P., 1997, Science, 276, 1836

Boss A. P., 2007, ApJ, 661, L73

Braiding C. R., 2011, PhD thesis, Macquarie University (arXiv:1110.2168v1)

Braiding C. R., Wardle M., 2012, MNRAS, 427, 3188

Brogan C. L. et al., 2015, ApJ, 808, L3

Bryden G., Chen X., Lin D. N. C., Nelson R. P., Papaloizou J. C. B., 1999, ApJ, 514, 344

Cameron A. G. W., 1978, Moon and Planets, 18, 5

Canup R. M., Ward W. R., 2002, AJ, 124, 3404

Canup R. M., Ward W. R., 2006, Nature, 441, 834

Casassus S. et al., 2013, Nature, 493, 191

Cassen P., Moosman A., 1981, Icarus, 48, 353

Chandrasekhar S., 1960, Proceedings of the National Academy of Science, 46, 253

Chiang E. I., Goldreich P., 1997, ApJ, 490, 368

Cisowski S. M., Hood L. L., 1991, Sun in Time, Sonett C. P., Giampapa M., Matthews M. S., eds., Vol. 761. Tucson: Univ. Arizona Press

Clarke C., Lodato G., Melnikov S. Y., Ibrahimov M. A., 2005, MNRAS, 361, 942

Cleeves L. I., Bergin E. A., Harries T. J., 2015, ApJ, 807, 2

Coradini A., Cerroni P., Magni G., Federico C., 1989, Formation of the satellites of the outer solar system - Sources of their atmospheres, Atreya S. K., Pollack J. B., Matthews M. S., eds., pp. 723–762

Crida A., Morbidelli A., Masset F., 2006, Icarus, 181, 587

D'Angelo G., Henning T., Kley W., 2002, A&A, 385, 647

D'Angelo G., Henning T., Kley W., 2003, ApJ, 599, 548

D'Angelo G., Kley W., Henning T., 2003, ApJ, 586, 540

Dawson R. I., Murray-Clay R. A., 2013, ApJ, 767, L24

Debes J. H., Jang-Condell H., Weinberger A. J., Roberge A., Schneider G., 2013, ApJ, 771, 45

Desch S. J., 2007, ApJ, 671, 878

Dong R., Zhu Z., Rafikov R. R., Stone J. M., 2015, ApJ, 809, L5

Draine B. T., 1980, ApJ, 241, 1021

Draine B. T., Roberge W. G., Dalgarno A., 1983, ApJ, 264, 485

Draine B. T., Sutin B., 1987, ApJ, 320, 803

Dullemond C. P., Hollenbach D., Kamp I., D'Alessio P., 2007, Protostars and Planets V, 555

Dunham M. M., Vorobyov E. I., 2012, ApJ, 747, 52

Dunhill A. C., 2015, MNRAS, 448, L67

Elmegreen B. G., 1979, ApJ, 232, 729

Esteban C., Peimbert M., Torres-Peimbert S., Escalante V., 1998, MNRAS, 295, 401

Faulkner J., Lin D. N. C., Papaloizou J., 1983, MNRAS, 205, 359

Fendt C., 2003, A&A, 411, 623

Flaig M., Ruoff P., Kley W., Kissmann R., 2012, MNRAS, 420, 2419

Flock M., Dzyurkevich N., Klahr H., Turner N., Henning T., 2012, ApJ, 744, 144

Flock M., Ruge J. P., Dzyurkevich N., Henning T., Klahr H., Wolf S., 2015, A&A, 574, A68

Forgan D., Rice K., 2010, MNRAS, 402, 1349

Forgan D., Rice K., 2013, MNRAS, 432, 3168

Forgan D., Rice K., Cossins P., Lodato G., 2011, MNRAS, 410, 994

Fricke K., 1968, ZAp, 68, 317

Fromang S., Nelson R. P., 2009, A&A, 496, 597

Fu R. et al., 2014, Science

Fujii Y. I., Okuzumi S., Inutsuka S.-i., 2011, ApJ, 743, 53

Fujii Y. I., Okuzumi S., Tanigawa T., Inutsuka S.-i., 2014, ApJ, 785, 101

Galassi M., Davies J., Theiler J., Gough B., Jungman G., Alken P., Booth M., Rossi F., 2009, GNU Scientific Library Reference Manual, 3rd edn., Gough B., ed. Network Theory Ltd.

Galvagni M., Mayer L., 2014, MNRAS, 437, 2909

Gammie C. F., 1996, ApJ, 457, 355

Gammie C. F., 2001, ApJ, 553, 174

Garufi A., Quanz S. P., Schmid H. M., Avenhaus H., Buenzli E., Wolf S., 2014, A&A, 568, A40

Goldreich P., Schubert G., 1967, ApJ, 150, 571

Goldreich P., Tremaine S., 1979, ApJ, 233, 857

Goldreich P., Tremaine S., 1980, ApJ, 241, 425

Goldreich P., Ward W. R., 1973, ApJ, 183, 1051

Gomes R., Levison H. F., Tsiganis K., Morbidelli A., 2005, Nature, 435, 466

Goodman J., Rafikov R. R., 2001, ApJ, 552, 793

Gradshteyn I. S., Ryzhik I. M., 2007, Table of integrals, series, and products, seventh edn. Elsevier/Academic Press, Amsterdam, pp. xlviii+1171

Gressel O., Nelson R. P., Turner N. J., Ziegler U., 2013, ApJ, 779, 59

Gressel O., Turner N. J., Nelson R. P., McNally C. P., 2015, ApJ, 801, 84

Guilet J., Ogilvie G. I., 2012, MNRAS, 424, 2097

Guilet J., Ogilvie G. I., 2013, MNRAS, 430, 822

Guilet J., Ogilvie G. I., 2014, MNRAS, 441, 852

Guilloteau S., Dutrey A., 1998, A&A, 339, 467

Guilloteau S., Dutrey A., Wakelam V., Hersant F., Semenov D., Chapillon E., Henning T., Piétu V., 2012, A&A, 548, A70

Hartigan P., Edwards S., Ghandour L., 1995, ApJ, 452, 736

Hartmann L., Calvet N., Gullbring E., D'Alessio P., 1998, ApJ, 495, 385

Hartmann L., Kenyon S. J., 1985, ApJ, 299, 462

Hartmann L., Kenyon S. J., 1996, ARA&A, 34, 207

Hawley J. F., Gammie C. F., Balbus S. A., 1995, ApJ, 440, 742

Hayashi C., 1981, Progress of Theoretical Physics Supplement, 70, 35

Heinisch R. L., Bronold F. X., Fehske H., 2010, Phys. Rev. B, 82, 125408

Herbig G. H., 1977, ApJ, 217, 693

Herbig G. H., 1989, in European Southern Observatory Conference and Workshop Proceedings, Vol. 33, European Southern Observatory Conference and Workshop Proceedings, Reipurth B., ed., pp. 233–246

Herbig G. H., 2007, AJ, 133, 2679

Hirose S., Turner N. J., 2011, ApJ, 732, L30

Hubbard W. B., Burrows A., Lunine J. I., 2002, ARA&A, 40, 103

Hubeny I., 1990, ApJ, 351, 632

Hughes A. M., Wilner D. J., Andrews S. M., Qi C., Hogerheijde M. R., 2011, ApJ, 727, 85

Hull C. L. H., Plambeck R. L., Bolatto A., et al., 2013, ApJ, 768, 159

Ida S., Makino J., 1993, Icarus, 106, 210

Igea J., Glassgold A. E., 1999, ApJ, 518, 848

Ilgner M., Nelson R. P., 2006, A&A, 445, 223

Ilgner M., Nelson R. P., 2008, A&A, 483, 815

Inutsuka S.-i., Sano T., 2005, ApJ, 628, L155

Ioannidis G., Froebrich D., 2012, MNRAS, 425, 1380

Isella A., Chandler C. J., Carpenter J. M., Pérez L. M., Ricci L., 2014, ApJ, 788, 129

Jin L., 1996, ApJ, 457, 798

Johansen A., Oishi J. S., Mac Low M.-M., Klahr H., Henning T., Youdin A., 2007, Nature, 448, 1022

Johnson B. M., Gammie C. F., 2006, ApJ, 636, 63

Jones E., Oliphant T., Peterson P., et al., 2001, SciPy: Open source scientific tools for Python -http://www.scipy.org/

Keith S. L., Wardle M., 2014, MNRAS, 440, 89

Keith S. L., Wardle M., 2015, MNRAS, 451, 1104

King A. R., Pringle J. E., Livio M., 2007, MNRAS, 376, 1740

Kipping D. M., Forgan D., Hartman J., Nesvorný D., Bakos G. Á., Schmitt A., Buchhave L., 2013, ApJ, 777, 134

Kitamura Y., Momose M., Yokogawa S., Kawabe R., Tamura M., Ida S., 2002, ApJ, 581, 357

Klahr H. H., Bodenheimer P., 2003, ApJ, 582, 869

Kokubo E., Ida S., 1998, Icarus, 131, 171

Königl A., Salmeron R., Wardle M., 2010, MNRAS, 401, 479

Krasnopolsky R., Königl A., 2002, ApJ, 580, 987

Krasnopolsky R., Li Z.-Y., Blandford R., 1999, ApJ, 526, 631

Krasnopolsky R., Li Z.-Y., Shang H., 2011, ApJ, 733, 54

Krumholz M. R., Crutcher R. M., Hull C. L. H., 2013, ApJ, 767, L11

Kuiper G. P., 1951, Proceedings of the National Academy of Science, 37, 1

Kunz M. W., Lesur G., 2013, MNRAS, 434, 2295

Latham D. W. et al., 2011, ApJ, 732, L24

Latter H. N., Papaloizou J. C. B., 2012, MNRAS, 426, 1107

Laughlin G., Bodenheimer P., 1994, ApJ, 436, 335

Lesur G., Kunz M. W., Fromang S., 2014, A&A, 566, A56

Lesur G., Longaretti P.-Y., 2009, A&A, 504, 309

Li Z.-Y., Banerjee R., Pudritz R. E., Jørgensen J. K., Shang H., Krasnopolsky R., Maury A., 2014, Protostars and Planets VI, 173

Li Z.-Y., Krasnopolsky R., Shang H., 2011, ApJ, 738, 180

Lide D. R., 2004, CRC Handbook of Chemistry and Physics, 85th Edition, 85th edn., Lide D. R., ed. CRC Press

Lin D. N. C., Papaloizou J., 1985, in Protostars and Planets II, Black D. C., Matthews M. S., eds., pp. 981–1072

Lin D. N. C., Papaloizou J., 1986, ApJ, 309, 846

Lissauer J. J., Hubickyj O., D'Angelo G., Bodenheimer P., 2009, Icarus, 199, 338

Lizano S., Galli D., Cai M. J., Adams F. C., 2010, ApJ, 724, 1561

Lodato G., Clarke C. J., 2004, MNRAS, 353, 841

Lorén-Aguilar P., Bate M. R., 2015, MNRAS, 453, L78

Lovelace R. V. E., Covey K. R., Lloyd J. P., 2011, AJ, 141, 51

Lovelace R. V. E., Romanova M. M., Newman W. I., 1994, ApJ, 437, 136

Lubow S. H., D'Angelo G., 2006, ApJ, 641, 526

Lubow S. H., Martin R. G., 2012, ApJ, 749, L37

Lubow S. H., Papaloizou J. C. B., Pringle J. E., 1994, MNRAS, 267, 235

Lubow S. H., Seibert M., Artymowicz P., 1999, ApJ, 526, 1001

Lunine J. I., Stevenson D. J., 1982, Icarus, 52, 14

Lynden-Bell D., Pringle J. E., 1974, MNRAS, 168, 603

Lyra W., Klahr H., 2011, A&A, 527, A138

Machida M. N., 2009, MNRAS, 392, 514

Machida M. N., Inutsuka S.-I., Matsumoto T., 2006, ApJ, 649, L129

Machida M. N., Kokubo E., Inutsuka S.-I., Matsumoto T., 2008, ApJ, 685, 1220

Malhotra R., 1993, Nature, 365, 819

Martin R. G., Lubow S. H., 2011a, ApJ, 740, L6

Martin R. G., Lubow S. H., 2011b, MNRAS, 413, 1447

Matsumoto T., Tomisaka K., 2004, ApJ, 616, 266

Mayor M., Queloz D., 1995, Nature, 378, 355

McElroy D., Walsh C., Markwick A. J., Cordiner M. A., Smith K., Millar T. J., 2013, A&A, 550, A36

McKee C. F., Ostriker E. C., 2007, ARA&A, 45, 565

Meru F., Bate M. R., 2012, MNRAS, 427, 2022

Meyer F., Meyer-Hofmeister E., 1981, A&A, 104, L10

Miller K. A., Stone J. M., 2000, ApJ, 534, 398

Mizuno H., 1980, Progress of Theoretical Physics, 64, 544

Mohanty S., Ercolano B., Turner N. J., 2013, ApJ, 764, 65

Mosqueira I., Estrada P., Turrini D., 2010, Space Sci. Rev., 153, 431

Mosqueira I., Estrada P. R., 2003, Icarus, 163, 198

Muranushi T., Okuzumi S., Inutsuka S.-I., 2012, ApJ, 760, 56

Nelson A. F., Benz W., 2003, ApJ, 589, 578

Nelson A. F., Benz W., Ruzmaikina T. V., 2000, ApJ, 529, 357

Nelson R. P., Papaloizou J. C. B., 2003, MNRAS, 339, 993

Nelson R. P., Papaloizou J. C. B., 2004, MNRAS, 350, 849

Ober F., Wolf S., Uribe A. L., Klahr H. H., 2015, A&A, 579, A105

Ogilvie G. I., Livio M., 2001, ApJ, 553, 158

O'Keeffe W., Downes T. P., 2014, MNRAS, 441, 571

Okuzumi S., Hirose S., 2011, ApJ, 742, 65

Okuzumi S., Inutsuka S.-i., 2015, ApJ, 800, 47

Okuzumi S., Ormel C. W., 2013, ApJ, 771, 43

Okuzumi S., Takeuchi T., Muto T., 2014, ApJ, 785, 127

Ormel C. W., Okuzumi S., 2013, ApJ, 771, 44

Paardekooper S.-J., 2012, MNRAS, 421, 3286

Paczynski B., 1978, Acta Astron., 28, 91

Pandey B. P., Wardle M., 2008, MNRAS, 385, 2269

Papaloizou J. C. B., Lin D. N. C., 1995, ARA&A, 33, 505

Papaloizou J. C. B., Nelson R. P., Snellgrove M. D., 2004, MNRAS, 350, 829

Parkin E. R., Bicknell G. V., 2013, ApJ, 763, 99

Perez S., Dunhill A., Casassus S., Roman P., Szulágyi J., Flores C., Marino S., Montesinos M., 2015, ApJ, 811, L5

Perez-Becker D., Chiang E., 2011, ApJ, 735, 8

Petkaki P., Freeman M. P., Kirk T., Watt C. E. J., Horne R. B., 2006, Journal of Geophysical Research (Space Physics), 111, 1205

Pfalzner S., 2008, A&A, 492, 735

Piétu V., Dutrey A., Guilloteau S., 2007, A&A, 467, 163

Pineda J. E., Quanz S. P., Meru F., Mulders G. D., Meyer M. R., Panić O., Avenhaus H., 2014, ApJ, 788, L34

Pinilla P., de Juan Ovelar M., Ataiee S., Benisty M., Birnstiel T., van Dishoeck E. F., Min M., 2015, A&A, 573, A9

Pinto C., Galli D., 2008, A&A, 484, 17

Pollack J. B., Hollenbach D., Beckwith S., Simonelli D. P., Roush T., Fong W., 1994, ApJ, 421, 615

Pollack J. B., Hubickyj O., Bodenheimer P., Lissauer J. J., Podolak M., Greenzweig Y., 1996, Icarus, 124, 62

Powell M. J. D., 1970, in Numerical Methods for Nonlinear Algebraic Equations, Rabinowitz P., ed., Gordon and Breach

Pringle J. E., 1977, MNRAS, 178, 195

Pringle J. E., 1981, ARA&A, 19, 137

Quanz S. P., Avenhaus H., Buenzli E., Garufi A., Schmid H. M., Wolf S., 2013, ApJ, 766, L2

Quillen A. C., Trilling D. E., 1998, ApJ, 508, 707

Rafikov R. R., 2007, ApJ, 662, 642

Rao R., Girart J. M., Lai S.-P., Marrone D. P., 2014, ApJ, 780, L6

Rasio F. A., Ford E. B., 1996, Science, 274, 954

Rayleigh L., 1917, Royal Society of London Proceedings Series A, 93

Reggiani M. et al., 2014, ApJ, 792, L23

Reipurth B., Aspin C., Herbig G. H., 2012, ApJ, 748, L5

Reipurth B., Bally J., 2001, ARA&A, 39, 403

Ricci L., Testi L., Natta A., Scholz A., de Gregorio-Monsalvo I., Isella A., 2014, ApJ, 791, 20

Rice W. K. M., Lodato G., Pringle J. E., Armitage P. J., Bonnell I. A., 2004, MNRAS, 355, 543

Rice W. K. M., Paardekooper S.-J., Forgan D. H., Armitage P. J., 2014, MNRAS, 438, 1593

Rivier G., Crida A., Morbidelli A., Brouet Y., 2012, A&A, 548, A116

Safronov V., 1969, Evolution of the Protoplanetary Cloud and Formation of the Earth and the Planets. Nauka, Moscow

Safronov V. S., 1967, Soviet Ast., 10, 650

Salmeron R., Königl A., Wardle M., 2011, MNRAS, 412, 1162

Sano T., Inutsuka S.-I., Turner N. J., Stone J. M., 2004, ApJ, 605, 321

Sano T., Miyama S. M., 1999, ApJ, 515, 776

Sano T., Miyama S. M., Umebayashi T., Nakano T., 2000, ApJ, 543, 486

Sano T., Stone J. M., 2002, ApJ, 577, 534

Sasaki T., Stewart G. R., Ida S., 2010, ApJ, 714, 1052

Savonije G. J., Papaloizou J. C. B., Lin D. N. C., 1994, MNRAS, 268, 13

Schneider J., Dedieu C., Le Sidaner P., Savalle R., Zolotukhin I., 2011, A&A, 532, A79

Semenov D., Henning T., Helling C., Ilgner M., Sedlmayr E., 2003, A&A, 410, 611

Shabram M., Boley A. C., 2013, ApJ, 767, 63

Shakura N. I., Sunyaev R. A., 1973, A&A, 24, 337

Shi J., Krolik J. H., Hirose S., 2010, ApJ, 708, 1716

Shu F., Najita J., Ostriker E., Wilkin F., Ruden S., Lizano S., 1994, ApJ, 429, 781

Shu F. H., Adams F. C., Lizano S., 1987, ARA&A, 25, 23

Shu F. H., Galli D., Lizano S., Glassgold A. E., Diamond P. H., 2007, ApJ, 665, 535

Simon J. B., Hawley J. F., Beckwith K., 2011, ApJ, 730, 94

Simon J. B., Hughes A. M., Flaherty K. M., Bai X.-N., Armitage P. J., 2015, ApJ, 808, 180

Spitzer L., 1962, Physics of Fully Ionized Gases

Spitzer, Jr. L., 1941, ApJ, 93, 369

Stephens I. W. et al., 2014, Nature, 514, 597

Stevenson D. J., 2003, Earth and Planetary Science Letters, 208, 1

Szulágyi J., Morbidelli A., Crida A., Masset F., 2014, ApJ, 782, 65

Takata T., Stevenson D. J., 1996, Icarus, 123, 404

Takeuchi T., Okuzumi S., 2014, ApJ, 797, 132

Tanaka H., Takeuchi T., Ward W. R., 2002, ApJ, 565, 1257

Tanigawa T., Ohtsuki K., Machida M. N., 2012, ApJ, 747, 47

Terquem C. E. J. M. L. J., 2003, MNRAS, 341, 1157

Toomre A., 1964, ApJ, 139, 1217

Tsiganis K., Gomes R., Morbidelli A., Levison H. F., 2005, Nature, 435, 459

Tsukamoto Y., Iwasaki K., Okuzumi S., Machida M. N., Inutsuka S., 2015, ApJ, 810, L26

Turner N. J., Fromang S., Gammie C. F., Klahr H. H., Lesur G., Wardle M., Bai X.-N., 2014, in Protostars and Planets VI

Turner N. J., Lee M. H., Sano T., 2014, ApJ, 783, 14

Turner N. J., Sano T., 2008, ApJ, 679, L131

Turner N. J., Sano T., Dziourkevitch N., 2007, ApJ, 659, 729

Umebayashi T., Nakano T., 1980, PASJ, 32, 405

Umebayashi T., Nakano T., 1981, PASJ, 33, 617

Umebayashi T., Nakano T., 2009, ApJ, 690, 69

Uribe A. L., Klahr H., Henning T., 2013, ApJ, 769, 97

Velikhov E., 1959, J. Exp. Theor. Phys. (USSR), 36, 1398

Vorobyov E. I., Basu S., 2005, ApJ, 633, L137

Vorobyov E. I., Basu S., 2015, ApJ, 805, 115

Walsh K. J., Morbidelli A., Raymond S. N., O'Brien D. P., Mandell A. M., 2011, Nature, 475, 206

Ward W. R., 1986, Icarus, 67, 164

Ward W. R., 1997, Icarus, 126, 261

Ward W. R., Canup R. M., 2010, AJ, 140, 1168

Wardle M., 1998, MNRAS, 298, 507

Wardle M., 1999, MNRAS, 307, 849

Wardle M., 2007, Ap&SS, 311, 35

Wardle M., Königl A., 1993, ApJ, 410, 218

Wardle M., Salmeron R., 2012, MNRAS, 422, 2737

Weidenschilling S. J., 1977, Ap&SS, 51, 153

Weidenschilling S. J., Cuzzi J. N., 1993, in Protostars and Planets III, Levy E. H., Lunine J. I., eds., pp. 1031–1060

Weiss B. P., Gattacceca J., Stanley S., Rochette P., Christensen U. R., 2010, Space Sci. Rev., 152, 341

Whipple F. L., 1972, in From Plasma to Planet, Elvius A., ed., p. 211

Williams J. P., Cieza L. A., 2011, ARA&A, 49, 67

Winn J. N., Fabrycky D. C., 2015, ARA&A, 53, 409

Wolszczan A., Frail D. A., 1992, Nature, 355, 145

Youdin A. N., 2010, in EAS Publications Series, Vol. 41, EAS Publications Series, Montmerle T., Ehrenreich D., Lagrange A.-M., eds., pp. 187–207

Youdin A. N., Goodman J., 2005, ApJ, 620, 459

Zhang K., Blake G. A., Bergin E. A., 2015, ApJ, 806, L7

Zhou Y., Herczeg G. J., Kraus A. L., Metchev S., Cruz K. L., 2014, ApJ, 783, L17

Zhu Z., 2015, ApJ, 799, 16

Zhu Z., Dong R., Stone J. M., Rafikov R. R., 2015, ApJ, 813, 88

Zhu Z., Hartmann L., Calvet N., Hernandez J., Muzerolle J., Tannirkulam A.-K., 2007, ApJ, 669, 483

Zhu Z., Hartmann L., Calvet N., Hernandez J., Tannirkulam A.-K., D'Alessio P., 2008, ApJ, 684, 1281

Zhu Z., Hartmann L., Gammie C., 2009, ApJ, 694, 1045

Zhu Z., Hartmann L., Gammie C., McKinney J. C., 2009, ApJ, 701, 620

Zsom A., Ormel C. W., Güttler C., Blum J., Dullemond C. P., 2010, A&A, 513, A57